



University of Kentucky
UKnowledge

Theses and Dissertations--Biomedical
Engineering

Biomedical Engineering


2019

NONINVASIVE MULTIMODAL DIFFUSE OPTICAL IMAGING OF VULNERABLE TISSUE HEMODYNAMICS

Mingjun Zhao

University of Kentucky, mjzh235@gmail.com

Author ORCID Identifier:

 <https://orcid.org/0000-0002-8657-4413>

Digital Object Identifier: <https://doi.org/10.13023/etd.2019.300>

Right click to open a feedback form in a new tab to let us know how this document benefits you.

Recommended Citation

Zhao, Mingjun, "NONINVASIVE MULTIMODAL DIFFUSE OPTICAL IMAGING OF VULNERABLE TISSUE HEMODYNAMICS" (2019). *Theses and Dissertations--Biomedical Engineering*. 58.

https://uknowledge.uky.edu/cbme_etds/58

This Doctoral Dissertation is brought to you for free and open access by the Biomedical Engineering at UKnowledge. It has been accepted for inclusion in Theses and Dissertations--Biomedical Engineering by an authorized administrator of UKnowledge. For more information, please contact UKnowledge@lsv.uky.edu.

STUDENT AGREEMENT:

I represent that my thesis or dissertation and abstract are my original work. Proper attribution has been given to all outside sources. I understand that I am solely responsible for obtaining any needed copyright permissions. I have obtained needed written permission statement(s) from the owner(s) of each third-party copyrighted matter to be included in my work, allowing electronic distribution (if such use is not permitted by the fair use doctrine) which will be submitted to UKnowledge as Additional File.

I hereby grant to The University of Kentucky and its agents the irrevocable, non-exclusive, and royalty-free license to archive and make accessible my work in whole or in part in all forms of media, now or hereafter known. I agree that the document mentioned above may be made available immediately for worldwide access unless an embargo applies.

I retain all other ownership rights to the copyright of my work. I also retain the right to use in future works (such as articles or books) all or part of my work. I understand that I am free to register the copyright to my work.

REVIEW, APPROVAL AND ACCEPTANCE

The document mentioned above has been reviewed and accepted by the student's advisor, on behalf of the advisory committee, and by the Director of Graduate Studies (DGS), on behalf of the program; we verify that this is the final, approved version of the student's thesis including all changes required by the advisory committee. The undersigned agree to abide by the statements above.

Mingjun Zhao, Student

Dr. Guoqiang Yu, Major Professor

Dr. Sridhar Sunderam, Director of Graduate Studies

NONINVASIVE MULTIMODAL DIFFUSE OPTICAL IMAGING
OF VULNERABLE TISSUE HEMODYNAMICS

DISSERTATION

A dissertation submitted in partial fulfillment of the
requirements for the degree of Doctor of Philosophy in the
College of Engineering
at the University of Kentucky

By
Mingjun Zhao
Lexington, Kentucky
Director: Dr. Guoqiang Yu, Professor of Biomedical Engineering
Lexington, Kentucky
2019

Copyright © Mingjun Zhao 2019
<https://orcid.org/0000-0002-8657-4413>

ABSTRACT OF DISSERTATION

NONINVASIVE MULTIMODAL DIFFUSE OPTICAL IMAGING OF VULNERABLE TISSUE HEMODYNAMICS

Measurement of tissue hemodynamics provides vital information for the assessment of tissue viability. This thesis reports three noninvasive near-infrared diffuse optical systems for spectroscopic measurements and tomographic imaging of tissue hemodynamics in vulnerable tissues with the goal of disease diagnosis and treatment monitoring. A hybrid near-infrared spectroscopy/diffuse correlation spectroscopy (NIRS/DCS) instrument with a contact fiber-optic probe was developed and utilized for simultaneous and continuous monitoring of blood flow (BF), blood oxygenation, and oxidative metabolism in exercising gastrocnemius. Results measured by the hybrid NIRS/DCS instrument in 37 subjects (mean age: 67 ± 6) indicated that vitamin D supplement plus aerobic training improved muscle metabolic function in older population. To reduce the interference and potential infection risk on vulnerable tissues caused by the contact measurement, a noncontact diffuse correlation spectroscopy/tomography (ncDCS/ncDCT) system was then developed. The ncDCS/ncDCT system employed optical lenses to project limited numbers of sources and detectors on the tissue surface. A motor-driven noncontact probe scanned over a region of interest to collect boundary data for three dimensional (3D) tomographic imaging of blood flow distribution. The ncDCS was tested for BF measurements in mastectomy skin flaps. Nineteen (19) patients underwent mastectomy and implant-based breast reconstruction were measured before and immediately after mastectomy. The BF index after mastectomy in each patient was normalized to its baseline value before surgery to get relative BF (rBF). Since rBF values in the patients with necrosis ($n = 4$) were significantly lower than those without necrosis ($n = 15$), rBF levels can be used to predict mastectomy skin flap necrosis. The ncDCT was tested for 3D imaging of BF distributions in chronic wounds of 5 patients. Spatial variations in BF contrasts over the wounded tissues were observed, indicating the capability of ncDCT in detecting tissue hemodynamic heterogeneities. To improve temporal/spatial resolution and avoid motion artifacts due to a long mechanical scanning of ncDCT, an electron-multiplying charge-coupled device based noncontact speckle contrast diffuse correlation tomography (scDCT) was developed. Validation of scDCT was done by imaging both high and low BF contrasts in tissue-like phantoms and human forearms. In a wound imaging study

using scDCT, significant lower BF values were observed in the burned areas/volumes compared to surrounding normal tissues in two patients with burn. One limitation in this study was the potential influence of other unknown tissue optical properties such as tissue absorption coefficient (μ_a) on BF measurements. A new algorithm was then developed to extract both μ_a and BF using light intensities and speckle contrasts measured by scDCT at multiple source-detector distances. The new algorithm was validated using tissue-like liquid phantoms with varied values of μ_a and BF index. In-vivo validation and application of the innovative scDCT technique with the new algorithm is the subject of future work.

KEYWORDS: Hybrid Near Infrared Spectroscopy/ Diffuse Correlation Spectroscopy (hybrid NIRS/DCS), Speckle Contrast Diffuse Correlation Tomography (scDCT), Noncontact Diffuse Correlation Tomography (ncDCT), Muscle, Flap, Wound

Mingjun Zhao

07/05/2019

NONINVASIVE MULTIMODAL DIFFUSE OPTICAL IMAGING
OF VULNERABLE TISSUE HEMODYNAMICS

By
Mingjun Zhao

Dr. Guoqiang Yu
Director of Dissertation

Dr. Sridhar Sunderam
Director of Graduate Studies

07/05/2019

DEDICATION

This work is dedicated to my family.

ACKNOWLEDGMENTS

First, I would like to thank my advisor, Dr. Guoqiang Yu, for his invaluable mentorship. Without him, this work would never have been possible. His brilliant ideas, keen insights and broad vision directed me through my graduate study. Dr. Yu also provided tremendous help on the training of critical thinking and professional writing which benefits me not only in this work but also in my future work.

I would also like to sincerely thank Dr. Yu Shang for clarifying many fundamental technical details in the early stage of my study. Dr. Chong Huang deserves many thanks for his great help on optical system configurations and experimental design. I would also like to acknowledge my other lab mates, Brad Henry, Ahmed Bahrani, Siavash Mazdeyasna, Drs. Yu Lin, Daniel Irwin and Lian He, who offered me help and encouragement during my study.

I appreciate the help from my collaborators including Drs. D. Travis Thomas, Maja Redzic, Dave Schnell, Lesley Wong, Destinee Eakle, Amanda Meeks and Dorothy Ross. The clinical studies in this work would never have been done without their help.

I would like to extend my thanks to the remaining members of my PhD committee, Drs. Abhijit Patwardhan and Sridhar Sunderam, for offering me valuable feedbacks throughout my study.

I acknowledge funding from the National Institutes of Health (NIH) Nos. R01-CA149274, R21-AR062356, R21-AG034279, R21-AG046762, and R21-HD091118; American Heart Association (AHA) Grant-In-Aid 16GRNT30820006; National Endowment for Plastic Surgery (NEPS), Plastic Surgery Foundation No. 3048112770;

National Science Foundation (NSF) EPSCoR #1539068. The content herein is solely the responsibility of the author(s) and does not necessarily represent the official views of the NIH, AHA, NEPS or NSF.

Finally I would like to thank my family for their constant love and support.

TABLE OF CONTENTS

ACKNOWLEDGMENTS	iii
LIST OF TABLES.....	vii
LIST OF FIGURES	viii
CHAPTER 1. Study Background and Importance.....	1
1.1 Hemodynamic assessment of vulnerable tissues	1
1.2 Technologies for the assessment of tissue hemodynamics.....	3
1.3 Diffuse optical technologies for hemodynamic assessment of vulnerable tissues	4
1.4 Development and application of innovative diffuse optical technologies for hemodynamic assessment of vulnerable tissues.....	7
CHAPTER 2. Hybrid Near-Infrared Spectroscopy/Diffuse Correlation Spectroscopy (NIRS/DCS) for Assessment of Exercising Muscle Hemodynamics in Older Adults with Vitamin D (vitD) Insufficiency ...	11
2.1 Introduction.....	11
2.2 Methods.....	14
2.2.1 NIRS for tissue oxygenation.....	14
2.2.2 DCS for tissue blood flow (BF)	19
2.2.3 Hybrid NIRS/DCS.....	23
2.2.4 Occlusive calibrations for absolute oxygen consumption rate (VO ₂) and BF	25
2.2.5 Gating algorithm.....	27
2.2.6 Fatigue gastrocnemius plantar flexion protocol.....	29
2.2.7 Monitoring of muscle hemodynamics during fatigue gastrocnemius plantar flexion in older adults with vitD insufficiency	31
2.3 Results.....	31
2.4 Discussion and conclusions	34
2.5 APPENDIX: Other engineering work.....	36
2.5.1 Torque and position data acquisition	36
2.5.2 Automatic recognition of torque peak	38
CHAPTER 3. Noncontact Diffuse Correlation Spectroscopy/Tomography (ncDCS/ncDCT) for Imaging of Mastectomy Skin Flaps and Chronic Wounds	40
3.1 Introduction.....	40
3.2 Methods.....	42
3.2.1 ncDCS/ncDCT instrumentation.....	42
3.2.2 DCT reconstruction.....	44
3.2.3 ncDCS for measurements of blood flow in mastectomy skin flaps	48
3.2.4 ncDCT for 3D imaging of chronic wounds	50

3.3	<i>Results</i>	52
3.3.1	Prediction of mastectomy skin flap necrosis.....	52
3.3.2	3D imaging of chronic wounds.....	54
3.4	<i>Discussion and conclusions</i>	56
CHAPTER 4. Speckle Contrast DCT (scDCT) for Imaging of Wounds		60
4.1	<i>Introduction</i>	60
4.2	<i>Methods</i>	62
4.2.1	scDCT instrumentation.....	62
4.2.2	3D reconstruction of blood flow distributions.....	64
4.2.3	2D mapping of blood flow distributions.....	66
4.2.4	Phantom tests.....	68
4.2.5	Imaging of forearm blood flow.....	70
4.2.6	Imaging of wounds.....	70
4.2.7	Simultaneous extraction of absorption coefficient (μ_a) and blood flow index (αD_B).....	72
4.2.8	Phantom tests for simultaneous extraction of μ_a and αD_B	75
4.3	<i>Results</i>	80
4.3.1	Phantom test results.....	80
4.3.2	Human forearm test results.....	82
4.3.3	3D and 2D imaging of wounds.....	83
4.3.4	Phantom test results for simultaneous extraction of μ_a and αD_B	85
4.4	<i>Discussion and conclusions</i>	88
CHAPTER 5. Study Summary, Limitations, and Future Perspectives		92
5.1	<i>Study Summary and my contributions</i>	92
5.2	<i>Study limitations and future perspectives</i>	95
APPENDIX: Glossary		97
REFERENCES		99
VITA		107

LIST OF TABLES

Table 3.1 rBF values in mastectomy skin flaps of 19 patients	52
Table 4.1 Specifications of Cascade 1K and Orca Flash 4.0LT	62
Table 4.2 Summary of phantom test results.....	86

LIST OF FIGURES

Figure 1.1 Absorption spectra of hemoglobin and water.....	6
Figure 2.1 Photon transportation in biological tissues.....	17
Figure 2.2 FD-NIRS device and probe.	19
Figure 2.3 DCS device and probe.	22
Figure 2.4 hybrid NIRS/DCS device.	24
Figure 2.5 Fiber-optic probe for hybrid NIRS/DCS device.....	25
Figure 2.6 Hybrid NIRS/DCS measurements of exercising gastrocnemius with occlusive calibrations and gating algorithms.....	26
Figure 2.7 Occlusive calibrations for absolute BF and VO_2	27
Figure 2.8 Illustration of gating algorithm.....	28
Figure 2.9 Typical muscle hemodynamic responses to exercise.	32
Figure 2.10 Hemodynamic responses to 13 weeks of intervention.	33
Figure 2.11 Muscle blood oxygen saturation responses to 13 weeks of intervention in post-exercise recovery.	34
Figure 2.12 Torque and position data acquisition system.....	37
Figure 2.13 Graphical user interface (GUI) for automatic recognition of torque peak. ...	39
Figure 3.1 ncDCS/ncDCT probe and experimental setup for wound imaging.	43
Figure 3.2 Mesh generation.	45
Figure 3.3 Mastectomy skin flap measurement setup.....	49
Figure 3.4 Prediction of mastectomy skin flap necrosis.	53
Figure 3.5 DCT results from the pressure ulcer case.....	55
Figure 3.6 DCT results from the diabetic ulcer case.	55
Figure 3.7 DCT measurement results from the non-healing traumatic injury case.	56
Figure 4.1 scDCT system configuration.	63
Figure 4.2 Variations in speckle contrasts over a range of S-D separations and exposure times.	65

Figure 4.3 Flowchart of 2D mapping algorithm.	67
Figure 4.4 Phantom tests with scDCT.	69
Figure 4.5 Imaging of BF distributions in burn wounds with scDCT system.	71
Figure 4.6 Two-step approach for extraction of μ_a and μ_s'	74
Figure 4.7 Effect of pinhole optimization.	76
Figure 4.8 Definition of pixel windows.	77
Figure 4.9 The reconstructed 3D images of tube flow contrasts.	80
Figure 4.10 Reconstructed images of spherical phantoms flow contrasts.	81
Figure 4.11 Reconstructed 3D images of forearm blood flow during cuff occlusion.	82
Figure 4.12 BF Distribution in Patient #1.	84
Figure 4.13 BF Distribution in Patient #2.	85
Figure 4.14 Ink titration results.	86
Figure 4.15 Temperature variation results.	87
Figure 4.16 Linear regressions of fitted unknowns against pre-set values.	87

1.1 Hemodynamic assessment of vulnerable tissues

Blood flow (BF) facilitates the delivery of nutrients and oxygen to tissues and the removal of metabolic byproducts from tissues. BF and its response to physiological changes indicate underlying tissue microenvironment conditions. It is equally important to understand tissue oxygenation since assessment of tissue oxygenation provides important information about the regulation of tissue oxygen delivery. In situations where oxygen delivery is insufficient to meet the demand, hypoxia will result. Many diseases in biological tissues may be detected by functional imaging of tissue hemodynamics (i.e., blood flow and oxygenation) prior to observable or palpable structural changes. Thus, monitoring of tissue BF and oxygenation provides critical information to medical professionals for the diagnosis and treatment monitoring of various diseases. Hemodynamic assessment also serves in animal studies to study pathology of diseases and to validate new medications.

One of the most prevalent objects in hemodynamic study is to characterize the hemodynamics in vulnerable tissues for diagnosis and treatment monitoring. Specifically, hemodynamic assessment is important for monitoring of vulnerable tissues such as wounds or injuries. Monitoring of hemodynamics in wounds (e.g., burn wounds, traumatic injuries) provides essential information for determining the necessity and area of wound excision and skin grafting to ensure successful surgical outcomes [1]. Notably, chronic wounds may never heal or take years to heal, thus resulting in poor quality of life

[2]. Individuals with peripheral arterial disease (PAD), diabetes, and paralysis have the highest risk of developing chronic wounds [3]. Pressure ulcer has high incident rate in patients with spinal cord injury and may lead to pain, infection and sepsis [4]. Prolonged pressure that applied to the tissue reducing blood flow and oxygenation supply, together with other risk factors including presents of moisture, limited mobility, poor nutrition and so on, leads to ulcer and prevents the ulcer from healing [4, 5].

Flap surgery is a common approach for tissue reconstruction. The flap is vulnerable and prone to tissue necrosis, which is one the most common complications after the surgery [6, 7]. Flap necrosis ensues when the blood supply to the flap is insufficient to meet metabolic needs. Knowledge of flap blood perfusion and variation during surgery may enable the surgeon to predict necrosis and failure of flaps. For example, in this dissertation work, BF in mastectomy skin flap was measured intraoperatively for patients undergo mastectomy and implant-based breast reconstruction immediately after mastectomy. The results suggested that the decrease in BF from pre- to post- operation was highly correlated with the incidence of flap necrosis, which demonstrated the potential of intraoperative BF assessment for necrosis prediction.

In many applications, for example in the assessment of intact muscles, contact measurement with a probe placed on tissue surface is doable without unforeseen risks. Contact measurement ensures better data quality for measurements in exercising muscles, which are prevalently used in studying muscle hemodynamics. However, for many other types of vulnerable tissues, such as open wounds and surgery incisions, noncontact measurements are preferred over contact measurements, where infection risk

and pain induced potentially by applying contact measurements are of great concerns. Moreover, the contact pressure applied to tissue surface may result in tissue deformation and alter the tissue hemodynamics, and consequently leading to inaccurate measurement results. Another benefit of noncontact measurement is that it complies better with sterile protocols in operating room for those intraoperative measurements.

In contrast to spectroscopic measurements, tomographic imaging of vulnerable tissue hemodynamics is also desired, as it provides valuable information for determining the locations and areas of ischemic/hypoxic tissues. For example, imaging of skin flaps may predict the risky area of tissue necrosis. Hemodynamic imaging of wound and surrounding tissues facilitates the evaluation of wound healing progress and determines the treatment strategy such as the necessity and scope of debridement.

1.2 Technologies for the assessment of tissue hemodynamics

A wide range of technologies have been developed to measure tissue BF. Doppler ultrasound is one of the most commonly used noninvasive techniques [8]. It performs well in assessing large vessel blood flow; but deep tissue wounds are more related to impairments in microcirculation. Techniques for microvascular perfusion measurement include optical coherence tomography [9], photoacoustic tomography [10], optical micro angiography [11] and skin perfusion pressure measurement [12]. Most of these techniques provide tissue perfusion information at skin level. Fluorescence angiography for tissue surface perfusion measurement is invasive and involves intravenous dye injection [13-15]. The measurement is transient and does not allow for continuous

monitoring. It has been applied in flap necrosis prediction and has been reported to over or under predict the risk of necrosis [15].

Various types of techniques have been developed for tissue oxygenation assessment. Hyperspectral image detects tissue oxygenation at the skin level [16]. Oxygen microelectrode can measure cellular oxygen level in a single cell although this method is invasive [17]. Transcutaneous oxygen measurement also measures tissue oxygenation, but it involves in complicated interaction between different tissue layers [18].

Larger imaging modalities such as positron emission tomography (PET) and magnetic resonance imaging (MRI) have the capacity of assessing both tissue BF/oxygenation and metabolism [19, 20]. These imaging technologies are expensive with large instruments. They require confinement to measurement tubes and thus limit the flexibility for muscle function characterization during exercising. In addition, PET involves radioactive elements, which is harmful to subjects.

1.3 Diffuse optical technologies for hemodynamic assessment of vulnerable tissues

Diffuse optical technologies using near-infrared light (NIR, 650-950 nm) have become popular over decades because of their noninvasiveness, safety, sensitivity to relatively deep tissues (up to several centimeters), and relatively lower cost in contrast to other large imaging instruments. These techniques are particularly useful for bedside and longitudinal monitoring of deep tissue hemodynamics. A variety of diffuse optical technologies have been developed for tissue hemodynamic assessment, including NIR

spectroscopy (NIRS) and diffuse optical tomography (DOT) for tissue oxygenation measurements [21-23] and diffuse correlation spectroscopy and tomography (DCS/DCT) for tissue BF measurements [24-28].

NIRS/DOT for tissue oxygenation measurements. NIRS provides a noninvasive, low-cost, rapid way for quantification of tissue optical properties, which are characterized by absorption coefficient μ_a (cm^{-1}) and reduced scattering coefficient μ_s' (cm^{-1}) [29-31]. The transportation of NIR light in biological tissues is dominated by scattering rather than absorption ($\mu_s' \gg \mu_a$) and therefore can be treated as a diffusive process. The absorption spectra of NIR light in biological tissue are shown in **Figure 1.1**. Major tissue chromophores to absorb NIR light include water (H_2O), oxy-hemoglobin (HbO_2), and deoxy-hemoglobin (Hb). Because of the relatively low absorption in biological tissues to NIR light (650 to 950 nm), NIRS can probe deep tissues (up to several centimeters). Since NIRS is sensitive to hemoglobin concentration variations in microvasculature, it enables tissue blood oxygenation detection, including oxy-hemoglobin concentration ($[\text{HbO}_2]$), deoxy-hemoglobin concentration ($[\text{Hb}]$), total hemoglobin concentration (THC), and blood oxygenation saturation (StO_2).

For tomographic imaging with NIRS (i.e., DOT), boundary data measured from large numbers of source and detector pairs are used to cover a target tissue volume. Three-dimensional images of tissue optical properties and oxygenation can be reconstructed from these measured boundary data with DOT principles. DOT has been used over decades for tissue oxygenation imaging [21, 22].

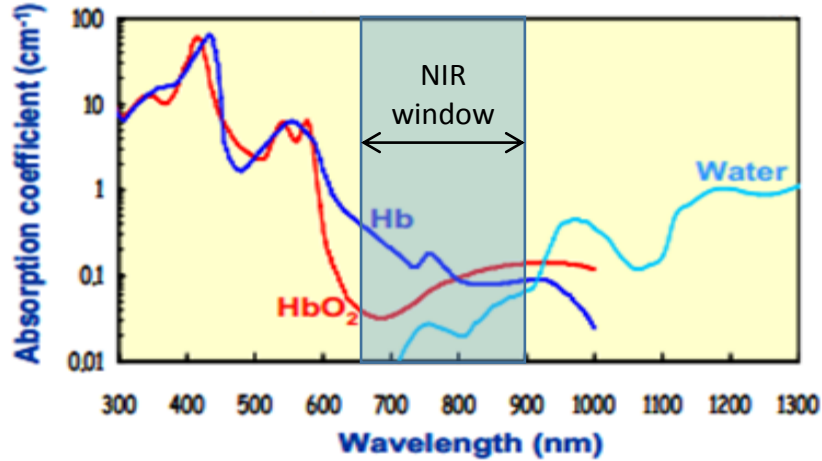


Figure 1.1 Absorption spectra of hemoglobin and water.

Tissue absorption coefficients (μ_a) of the three major absorbers in biological tissues (HbO_2 , Hb and water) are shown as function of wavelengths. Within the NIR window (650 to 900 nm), all three absorbers have relatively low absorptions thus enabling NIR light to penetrate deep into tissues. HbO_2 : oxy-hemoglobin, Hb: deoxy-hemoglobin.

DCS/DCT for tissue blood flow measurements. A dynamic NIR technique, namely diffuse correlation spectroscopy (DCS), has been developed for blood flow measurement in deep tissue [24-28]. Similar to NIRS, DCS uses NIR light to probe deep tissues. However, while NIRS only requires laser source with no specific requirement on coherence length, DCS uses a long coherence (coherence length > 5 meter) continuous-wave (CW) laser as the light source and high sensitivity single-photon-counting avalanche photodetector (APD) as the detector. DCS detects temporal light intensity fluctuations resulting from the interactions between photons and red blood cells in microvasculature at a single speckle area on the tissue surface using a single-mode fiber that transmits light only directly down the fiber connected to the APD. Through quantifying the time scale of light intensity fluctuation, DCS extracts blood flow index (BFI) that is related to the motion of red blood cells. Relative changes in blood flow

(rBF) are subsequently determined by normalizing flow data to its baseline level prior to the physiological change. DCS has been extensively validated against other techniques in various tissues, including Doppler ultrasound in tumors [32], Xenon-CT in traumatic brains, and arterial-spin labeled MRI (ASL-MRI) in human brains and muscles [24, 33, 34].

Similar to the extension from NIRS to DOT, DCS has been extended to DCT for three dimensional (3D) imaging of BF distributions using boundary data measured from multiple source-detector (S-D) pairs on the tissue surface. DCT has been applied for preclinical applications in small animal models [22, 35, 36].

1.4 Development and application of innovative diffuse optical technologies for hemodynamic assessment of vulnerable tissues

Conventional NIRS/DOT and DCS/DCT have technical limitations for assessing vulnerable tissues in different applications, which are described below. To overcome these limitations, I have optimized three innovative NIR diffuse optical systems for spectroscopic measurements and tomographic imaging of tissue hemodynamics in vulnerable tissues with the goal of disease diagnosis and treatment monitoring. These systems include a hybrid NIRS/DCS, a noncontact DCS/DCT (ncDCS/ncDCT), and a speckle contrast DCT (scDCT).

Hybrid NIRS/DCS for hemodynamic characterization of exercising muscles in older adults with Vitamin D (vitD) insufficiency (Chapter 2). The conventional NIRS or DCS alone is not capable of continuous monitoring of tissue oxidative (i.e.,

oxygen consumption rate (VO_2) which provides important information for the evaluation of muscle metabolic function. One reason for this is that DCS is sensitive to the motion of muscle fibers and could get motion artifacts in BF measurements during exercise [37]; the other is that DCS can accurately measure the change in BF relative to a baseline value, but it is not capable of absolute BF value quantification.

In this study, we combined a commercial NIRS device with a custom-made 4 channel DCS (hybrid NIRS/DCS) for simultaneous measurements of BF, blood oxygenation, and oxidative metabolism of exercising calf muscles in older adults with VitD insufficiency. A contact fiber-optic probe was designed for NIRS/DCS data acquisition from the same region of measured tissues. An innovative gating algorithm was developed to minimize motion artifacts during exercise [26-28]. Occlusive calibration protocols were developed for quantification of absolute VO_2 and BF values [26-28]. Using the optimized NIRS/DCS technique, I studied the relationships among vitD repletion, aerobic exercise, and muscle metabolic function in an older population with vitD insufficiency [38].

ncDCS/ncDCT for hemodynamic imaging of mastectomy skin flaps and chronic wounds (Chapter 3). Conventional NIRS and DCS have been used for noninvasive monitoring of oxygenation and blood flow in deep tissues with fiber-optic probes that gently contact the skin surface. However, measurements of tissue hemodynamics using contact probes are not appropriate for vulnerable tissues, such as surgery site and wound tissues. Contact measurement would increase the risk of infection and alter the tissue hemodynamic properties by applying the contact probe and thus lead to inaccurate measurement results.

To reduce the interference and potential infection risk on vulnerable tissues caused by the contact measurement, we developed an ncDCS/ncDCT system with optical lenses to project sources and detectors on the tissue surface [39-42]. The S-D pairs were arranged in a linear array. The motor-driven noncontact probe scanned linearly over a selected region of interest (ROI) to collect boundary data for 3D tomographic imaging. A finite element method (FEM) based reconstruction algorithm was developed for 3D reconstruction of BF distributions from these boundary measurements [39-41].

I have used the ncDCS/ncDCT system to measure BF distribution in mastectomy skin flaps for prediction of skin flap necrosis [43]. An intraoperative protocol for flap BF measurement was designed and implemented in 19 patients who underwent mastectomy and implant-based breast reconstruction. These patients were measured before and immediately after mastectomy, and after breast reconstruction. I have also applied the ncDCS/ncDCT system for 3D imaging of BF distributions in 5 patients with chronic wounds.

scDCT for 3D imaging of burn wounds (Chapter 4). The ncDCS/ncDCT system enabled noncontact spectroscopic and tomographic measurements of deep tissue BF. However, it has poor temporal and spatial resolution due to the time-consuming mechanical scanning. Each scanning may take up to more than ten minutes, which is prone to motion artifacts. With limited sources and detectors, its spatial resolution was poor. The ncDCS/ncDCT system used expensive APDs as detectors, which increase the instrument size and cost.

To overcome these limitations, we developed a camera-based scDCT system [44-46]. A galvo mirror was used to project point source laser light onto the measured tissue

surface. The diffused light speckle pattern was detected by a camera through optical lens system. The BF information was extracted from the speckle contrast measured by the camera. The scDCT enabled rapid data acquisition with high spatial resolution and without mechanical scanning. The optical lens system enabled flexible selection of different sizes of ROI for different applications. I used the innovative scDCT system to image patients with burned tissues [47].

One limitation of the scDCT system is the potential influence of unknown tissue optical properties such as μ_a on BFI quantification. Therefore, I developed a new algorithm to extract both μ_a and BFI using light intensities and speckle contrasts measured by scDCT at multiple S-D distances. I also designed and conducted tissue-like phantom tests to validate this innovative algorithm.

CHAPTER 2. HYBRID NEAR-INFRARED SPECTROSCOPY/DIFFUSE CORRELATION SPECTROSCOPY (NIRS/DCS) FOR ASSESSMENT OF EXERCISING MUSCLE HEMODYNAMICS IN OLDER ADULTS WITH VITAMIN D (VITD) INSUFFICIENCY

2.1 Introduction

Characterization of metabolic function in skeletal muscle has important applications in exercise and sports medicine and provides key information for understanding many diseases affecting skeletal muscle, such as peripheral vascular disease, fibromyalgia and heart failure [48-54]. Understanding of muscle metabolic function in older adults is fundamental for understanding the pathology of most age-related co-morbidities and has the potential to combat muscle function loss and to improve life quality.

Since differences in muscle function between healthy population and population with muscle dysfunction are not always apparent at rest, it is important to study muscle hemodynamic and metabolic changes in response to stimuli such as rhythmic exercise [49, 52, 54-56]. The ability to noninvasively quantify local muscle hemodynamics during exercise should provide critical information for muscle metabolic function evaluation, and has great potential for improving disease diagnosis and treatment assessment. Vitamin D (VitD) and exercise have positive effects on muscle health. Emerging data suggest that combining these treatments can alter muscle lipid distribution and mitochondrial capacity [57, 58]. This combination may preserve skeletal muscle function in aging [58, 59]. Therefore, assessment of muscle hemodynamics during exercise can be employed to evaluate muscle performance for older population who receive vitD

repletion and/or aerobic training in order to study the relationship between vitD repletion, aerobic training and skeletal muscle metabolic function.

Various techniques have been used in assessment of skeletal muscle blood flow (BF) during exercise in previous studies. Doppler ultrasound has been used for this purpose but it is limited to large vessel BF assessment. Microvascular BF evaluation techniques include laser Doppler flowmetry (LDF) [60, 61], skin perfusion pressure [12], and optical coherence tomography [62]; however, these techniques are limited to surface BF assessment at skin level. Positron emission tomography (PET) [63] and arterial-spin-labeled magnetic resonance imaging (ASL-MRI) [64] have made deep tissues microvascular BF monitoring possible, but these imaging modalities require large and expensive instrumentation that limits their use in exercise monitoring.

Oxygen consumption (VO_2) in skeletal muscle has also been quantified by several technologies. Muscle VO_2 can be measured invasively using the Fick principle that calculates VO_2 as the arteriovenous oxygen concentration difference times the cardiac output with blood sampling via catheter; however it does not accurately reflect the VO_2 level in local microvasculature because the blood samples are taken from major vessels connected to several muscle groups [65]. Spirometry measures whole body VO_2 noninvasively but it does not specify local tissue contribution [66]. Local muscle VO_2 has been quantified noninvasively by phosphorus magnetic resonance spectroscopy (P-MRS) but requires large and expensive equipment with limited sensitivity, thus limiting its application in exercise monitoring [67].

Near infrared (NIR) diffuse optical methods for tissue hemodynamics quantification have gained popularity in recent years. In previous studies, Near infrared

spectroscopy (NIRS) has been applied in investigation of tissue oxygenation changes in skeletal muscles during different types of exercise. Another NIR optical technology, diffuse correlation spectroscopy (DCS), has been developed for non-invasive measurement of the relative change of BF (rBF) in deep tissues [26-28, 32, 34, 68-71], including skeletal muscles [26-28, 34, 70]. DCS measurements of tissue BF have been validated by other standards, including Doppler ultrasound [56], Xenon-CT [24], and ASL-MRI [33].

Our laboratory has developed a hybrid optical device combining frequency domain (FD) NIRS and DCS technologies for simultaneous measurements of oxy and de-oxy hemoglobin concentrations ($[HbO_2]$, $[Hb]$), total hemoglobin concentration (THC), tissue blood oxygen saturation (StO_2), and rBF [72]. Simultaneous measurements of rBF and StO_2 enable the calculation of relative change in oxygen consumption (rVO_2) [56]. Only recently, an occlusive calibration has been applied by our lab to allow hybrid NIRS/DCS to simultaneously and continuously measure absolute values of BF and VO_2 in skeletal muscle [26, 28]. DCS is highly sensitive to muscle fiber motion and causes overestimation of BF during exercise, which prevented it from use in exercise monitoring. Recently, an innovative gating algorithm has been developed and applied in hybrid NIRS/DCS for exercising muscle monitoring to collect BF data only at time points when muscle fiber motion is minimal [26, 28, 37]. The application of the gating algorithm significantly improves the accuracy of BF measurements using DCS, and thus improved the accuracy in VO_2 quantification during exercise using hybrid NIRS/DCS. The hybrid NIRS/DCS system has been used in arm muscle measurements during exercise in previous studies [26, 27]. However, our particular interests are in the leg

muscles because lower limb is more likely influenced by diseases, such as peripheral arterial disease (PAD) and muscle metabolic dysfunction [73, 74]. Therefore, we applied the hybrid NIRS/DCS system for the hemodynamics monitoring during calf muscle exercise [28]. I have validated the hybrid NIRS/DCS system for calf muscle monitoring first in young healthy subjects and established the methods for the characterization of hemodynamic changes during exercise and in post-exercise recovery [28].

In this chapter, I report the methods and applications of our innovative hybrid NIRS/DCS instrument for quantification of calf muscle hemodynamics during exercise in older adults that are given vitD repletion and/or aerobic training to determine the effects of vitD repletion and aerobic training on hemodynamic and metabolic functions of skeletal muscles.

2.2 Methods

2.2.1 NIRS for tissue oxygenation

NIRS theory. The NIR window (650 to 900 nm) has made the application of diffuse optical measurements possible for biological tissues. The major chromophores in biological tissue are water and hemoglobin (oxyhemoglobin and deoxyhemoglobin). Within the NIR window, the absorption coefficient (μ_a) of water and hemoglobin are relatively low, allowing photons to penetrate deeply into tissue to up to several centimeters. The photon transportation in biological tissue can be treated as a diffusive process because scattering is the dominant event [75, 76]. The scattering coefficient (μ'_s)

is typically much larger (10 folds) than μ_a , therefore a photon may have been scattered multiple times before it is absorbed and a random walk pattern would be observed.

The diffusive process of photon propagation in biological tissue can be described by the photon diffusion equation [76, 77]. Specifically, the measured photon fluence rate, $\Phi(\mathbf{r},t)$ [$Watt \cdot cm^{-2}$], obeys the photon diffusion equation written in frequency domain as follows [76, 78]:

$$\nabla \cdot (D(\mathbf{r}) \nabla \Phi(\mathbf{r},t)) - v \mu_a(\mathbf{r}) \Phi(\mathbf{r},t) + v S(\mathbf{r},t) = \frac{\partial \Phi(\mathbf{r},t)}{\partial t} \quad (2.1)$$

Where, \mathbf{r} is the position vector, t [s] is time and v [$cm \cdot s^{-1}$] is the speed of light in the medium. $\mu_a(\mathbf{r})$ [cm^{-1}] is the absorption coefficient, $\mu_s'(\mathbf{r})$ [cm^{-1}] is the reduced scattering coefficient, and $D(\mathbf{r}) \equiv v/3(\mu_a(\mathbf{r}) + \mu_s'(\mathbf{r})) \approx v/3\mu_s'(\mathbf{r})$ [$cm^2 \cdot s^{-1}$] is the photon diffusion coefficient. $S(\mathbf{r},t)$ [$Watt \cdot cm^{-2}$] is the isotropic source term which quantifies the number of photons emitted at position \mathbf{r} and time t per unit volume per unit time.

The right hand side ($\frac{\partial \Phi(\mathbf{r},t)}{\partial t}$) describes the rate of the change of photon fluence within the sampled volume. It equals the number of photons scattered into the volume per unit time from its surroundings ($\nabla \cdot (D(\mathbf{r}) \nabla \Phi(\mathbf{r},t))$), minus the number of photons absorbed per unit time within the volume ($v \mu_a(\mathbf{r}) \Phi(\mathbf{r},t)$), plus the number of photons emitted per unit time from any sources in the volume ($v S(\mathbf{r},t)$). This diffusion approximation is valid when the following two premises are met: $\mu_a \ll \mu_s'$; the distance between source and detector is much greater than the random walk step length (~ 1 mm in biological tissue) [78].

When using point source, which can be mathematically described as $S(\mathbf{r},t) = S_0 \delta(\mathbf{r} - \mathbf{r}_s) \exp(-i\omega t)$, where S_0 is a constant, ω is the modulation frequency of sinusoidal

oscillation of the source. and r_s is the source location, Equation 2.1 can be simplified to [79]:

$$\nabla \cdot \left(\frac{D(r)}{v} \nabla \Phi(\mathbf{r}) \right) - (\mu_a(\mathbf{r}) + \frac{i\omega}{v}) \Phi(\mathbf{r}) = S_0 \delta(\mathbf{r} - \mathbf{r}_s) \quad (2.2)$$

Where $\Phi(\mathbf{r}, t) = \Phi(\mathbf{r}) \exp(-i\omega t)$.

The analytical solution of Equation 2.2 in semi-infinite geometry is [80]:

$$\Phi(\rho) = \frac{vS_0}{4\pi D} \left(\frac{\exp(-Kr_1)}{r_1} - \frac{\exp(-Kr_2)}{r_2} \right) \quad (2.3)$$

Where $K^2 = 3\mu_s' (-i\omega/v + \mu_a)$, $r_1 = \sqrt{\rho^2 + z_0^2}$ and $r_2 = \sqrt{\rho^2 + (z_0 + 2z_b)^2}$,

ρ is the source-detector (S-D) distance, z_b is the distance above the tissue surface where the fluence rate extrapolates to zero and z_0 is the effective depth of the source, $z_0 = 1/\mu_s'$ and $z_b = \frac{2}{3\mu_s'} \frac{1+R_{eff}}{1-R_{eff}}$, $R_{eff} = -1.44n^{-2} + 0.71n^{-1} + 0.668 + 0.064n$, $n \approx 1.33$ (for biological tissues). The R_{eff} term accounts for the mismatch between the medium and the air indices of refraction with n being the ratio between them.

To apply NIRS measurements for tissue absorption and scattering, photodetectors are typically used to detect the diffused light at known distances (few millimeters to centimeters) from point sources. **Figure 2.1** shows a simple measurement setup with one pair of source and detector in reflection geometry. Light injected into the tissue from source can be detected by the detector placed at a distance ρ from the source location. The sensitive region of diffuse light is usually described as a “banana pattern” with the penetration depth of $\sim \rho/2$ [78, 81].

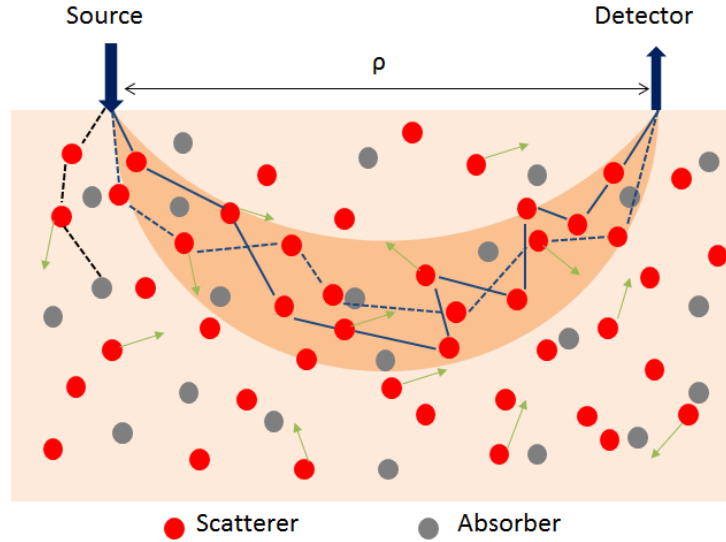


Figure 2.1 Photon transportation in biological tissues.

The source and detector fibers are placed on the tissue surface separated by a distance ρ . Grey and red dots represent tissue absorbers and scatterers respectively. Multiple scattering happen along a single photon path. The green arrows represent the moving directions of scatterers. The solid and dashed blue lines indicate potential paths of the detected photons. The dashed black lines indicate the potential paths of the photons absorbed before reaching to detector. The banana shape area indicates the average path of the detected photons emitted from the source location.

Multi-distance measurements of the phase and the amplitude of the photon fluence rate $\Phi(\mathbf{r}, t)$ with FD-NIRS system enable the extraction of optical properties (μ_s' and μ_a) of the measured tissue by fitting the analytical solution (**Equation 2.3**) with the measured fluence rate [82-84]. In the NIR band, deoxyhemoglobin (Hb) and oxyhemoglobin (HbO_2) have different absorption spectra (**Figure 1.1**) [85], therefore the concentrations of [Hb] and [HbO_2] can be calculated from known μ_a at two (or more) wavelengths [28, 82, 86]. The measured $\mu_a(\lambda)$ at each wavelength can be decomposed into the absorption contributions from the major tissue chromophores including Hb, HbO_2 and water (H_2O) [23]:

$$\mu_a(\lambda) = \epsilon_{\text{Hb}}(\lambda) \cdot [\text{Hb}] + \epsilon_{\text{HbO}_2}(\lambda) \cdot [\text{HbO}_2] + P_{\text{H}_2\text{O}} \cdot \mu_{a(\text{H}_2\text{O})}(\lambda) \quad (2.4)$$

Here, ϵ is wavelength-dependent extinction coefficient of the major tissue chromophores. Water absorption is usually considered constant and is thus fixed according to literature [87, 88]. Therefore, the two unknowns of [Hb] and [HbO₂] can be solved with assessment of μ_a at minimum two wavelengths.

THC and StO₂ can be derived based on [Hb] and [HbO₂] consequently as the following: $\text{THC} = [\text{Hb}] + [\text{HbO}_2]$; $\text{StO}_2 = [\text{HbO}_2]/\text{THC} \times 100\%$.

FD-NIRS instrument. In this study a commercial FD-NIRS (Imagent, Iss Inc., IL, USA) was used (**Figure 2.2**). The machine has two banks of sources (eight laser diodes at same wavelength for each bank) and one photomultipliers (PMT) detector. The 2 source wavelengths this machine has are 690 nm and 830 nm. The fiber-optic probe is optically coupled to laser-diode sources through multimode fibers (400 um fiber core). Sources are distributed at multiple distances ($\rho = 2.0, 2.5, 3.0, \text{ and } 3.5 \text{ cm}$) from the detector location. A large fiber bundle (2.5 mm in diameter) connected from the detector location on the probe to the PMT is used to detect the scattered light from the tissue. Source light at 690 and 830 nm are modulated at 110 MHz and multiplexed so that only one laser diode in each bank is on at a time. Fluence rate (AC, DC and phase) are measured and used to calculate μ_s' and μ_a for each wavelength and secondary outcomes ([Hb], [HbO₂], etc.).

Typically, the measurement time for each cycle covering all S-D pairs and wavelengths is 150 ms. Data from several cycles may be averaged to improve signal-to-noise ratio (SNR) upon specific measurement needs.

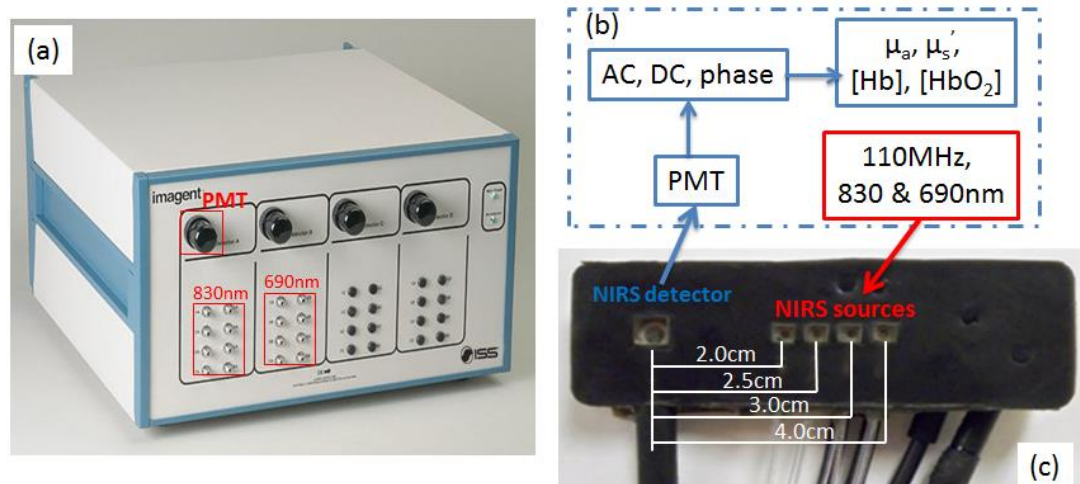


Figure 2.2 FD-NIRS device and probe.

(a) Commercial FD-NIRS (Imagent, Iss Inc., IL, USA); (b) Schematic of FD-NIRS; (c) Probe configuration of Imagent. FD-NIRS: frequency domain near infrared spectroscopy.

2.2.2 DCS for tissue blood flow (BF)

DCS theory. Similar to NIRS, DCS also probes deep tissues with NIR light. Instead of quantifying tissue blood oxygenation from the relatively slow changes in light intensities due to tissue absorption and scattering changes, DCS monitors the motion of moving scatterers (majorly red blood cells) in tissue by quantifying the fast temporal fluctuations in light intensities [36, 78, 89].

The normalized light intensity temporal autocorrelation function is calculated to characterize the light intensity fluctuations at multiple delay time τ :

$$g_2(\mathbf{r}, \tau) = \langle I(\mathbf{r}, t) \cdot I(\mathbf{r}, t + \tau) \rangle / \langle I(\mathbf{r}, t) \rangle^2 \quad (2.5)$$

Here, $I(\mathbf{r}, t)$ is the detected light intensity at position vector \mathbf{r} (from a source to a point of detection) and at time t . The $\langle \rangle$ denotes a time average. g_2 is calculated from the detected intensity fluctuations of scattered light. τ represents the delay time of

autocorrelation function. $g_2(\mathbf{r}, \tau)$ is related to the normalized electric field temporal autocorrelation function, $g_1(\tau)$, through the Siegert relationship [90]:

$$g_2(\mathbf{r}, \tau) = 1 + \beta |g_1(\mathbf{r}, \tau)|^2 \quad (2.6)$$

Here, β is a coherence factor depending mainly on the laser coherence and detection optics. β can be determined experimentally from measured $g_2(\mathbf{r}, \tau)$ via $\beta = g_2(\mathbf{r}, 0) - 1$.

The unnormalized electric field temporal autocorrelation $G1$ is defined by

$$G1(\mathbf{r}, \tau) = g_1(\mathbf{r}, \tau) \cdot G1(\mathbf{r}, 0) = g_1(\mathbf{r}, \tau) \cdot I(\mathbf{r}, 0) \quad (2.7)$$

The motions contributed by moving scatterers in biological tissue (red blood cells) result in the exponential decay of $G1$. The propagation of $G1$ in biological tissues can be described by the correlation diffusion equation in homogeneous medium for continuous-wave (CW) light source [36, 78, 89]:

$$\nabla \left(\left(\frac{D(\mathbf{r})}{v} \right) \nabla G1(\mathbf{r}, \tau) \right) - \left(\mu_a + \frac{1}{3} \mu_s' k_0^2 \alpha \langle \Delta r^2(\tau) \rangle \right) G1(\mathbf{r}, \tau) = -S_0 \delta(\mathbf{r}) \quad (2.8)$$

Here $D(\mathbf{r}) \approx v/3 \mu_s'$, v is the light speed in the medium, $S_0 \delta(\mathbf{r})$ is the CW source term, S_0 is a constant. $k_0 = 2\pi n/\lambda$ is the wave number of the source light in biological tissue, $n = 1.33$, λ is the source light wavelength. $\langle \Delta r^2(\tau) \rangle$ is the mean-square displacement of moving scatterers at delay time τ . To adapt the correlation diffusion equation for the use in biological tissues, a unitless factor α (ranging from 0 to 1) is introduced here to represent the ratio of light scattering events resulted from “moving” scatterers (e.g., red blood cells) to the total scatterers, since some of the scatterers in tissue are “static” (e.g., organelles, mitochondria, and nuclei). The factor α is included as a pre-fix to $\langle \Delta r^2(\tau) \rangle$ (i.e., $\alpha \langle \Delta r^2(\tau) \rangle$) to indicate the mean square displacement of

“moving” scatterers in biological tissues. In a semi-infinite homogeneous medium, analytical solution of $G_1(\mathbf{r}, \tau)$ are [78]:

$$G_1(\mathbf{r}, \tau) = \frac{vS_0}{4\pi D} \left(\frac{e^{-K(\tau)r_1}}{r_1} - \frac{e^{-K(\tau)r_2}}{r_2} \right) \quad (2.9)$$

Consequently, combining with **Equation 2.7**, the analytical expression for $g_1(\mathbf{r}, \tau)$ can be derived as:

$$g_1(\mathbf{r}, \tau) = \frac{G_1(\mathbf{r}, \tau)}{G_1(\mathbf{r}, 0)} = \left(\frac{e^{-K(\tau)r_1}}{r_1} - \frac{e^{-K(\tau)r_2}}{r_2} \right) / \left(\frac{e^{-K(0)r_1}}{r_1} - \frac{e^{-K(0)r_2}}{r_2} \right) \quad (2.10)$$

where $K^2(\tau) = 3\mu_s'\mu_a + \mu_s'^2 k_0^2 \alpha \langle \Delta r^2(\tau) \rangle$, is an effective “absorption” for the attenuation of G_1 as it transports through the tissue; while r_1, r_2 and \mathbf{r} are the same as in **Equation 2.3**.

For diffusive motion, $\alpha \langle \Delta r^2(\tau) \rangle = 6\alpha D_B \tau$, where D_B is the effective Brownian diffusion coefficient of tissue scatterers [91]. The combined term, αD_B , is referred as the blood flow index (BFI) in tissues and its relative change is commonly used to calculate the relative change of blood flow (rBF) compared with the baseline/resting BFI.

By introducing the BFI term αD_B , it is easy to tell that the analytical solution of $g_1(\mathbf{r}, \tau)$ is a function of αD_B and tissue optical properties (e.g., μ_s' and μ_a). Tissue optical properties can be measured using NIRS or assumed from literature, then $g_1(\mathbf{r}, \tau)$ is solely determined by αD_B . Meanwhile, the measured $g_1(\mathbf{r}, \tau)$ can be converted from the measured $g_2(\mathbf{r}, \tau)$ using the Siegert Relation (**Equation 2.6**) [90]. Therefore, αD_B can be extracted by varying αD_B in the analytical solution of $g_1(\mathbf{r}, \tau)$ and fitting it to the measured $g_1(\mathbf{r}, \tau)$ [25-28, 82].

DCS instrument. Figure 2.3a shows a 4-channel DCS device used in this study. It is consisted of a CW long coherence laser (coherence length > 5 m) at 830 nm (100 mw, CrystaLaser Inc., NV, USA), 4 single-photon-counting avalanche photodiodes (APDs) (e.g., Perkin Elmer Inc., Canada), and an autocorrelator board (Correlator.com, NJ, USA).

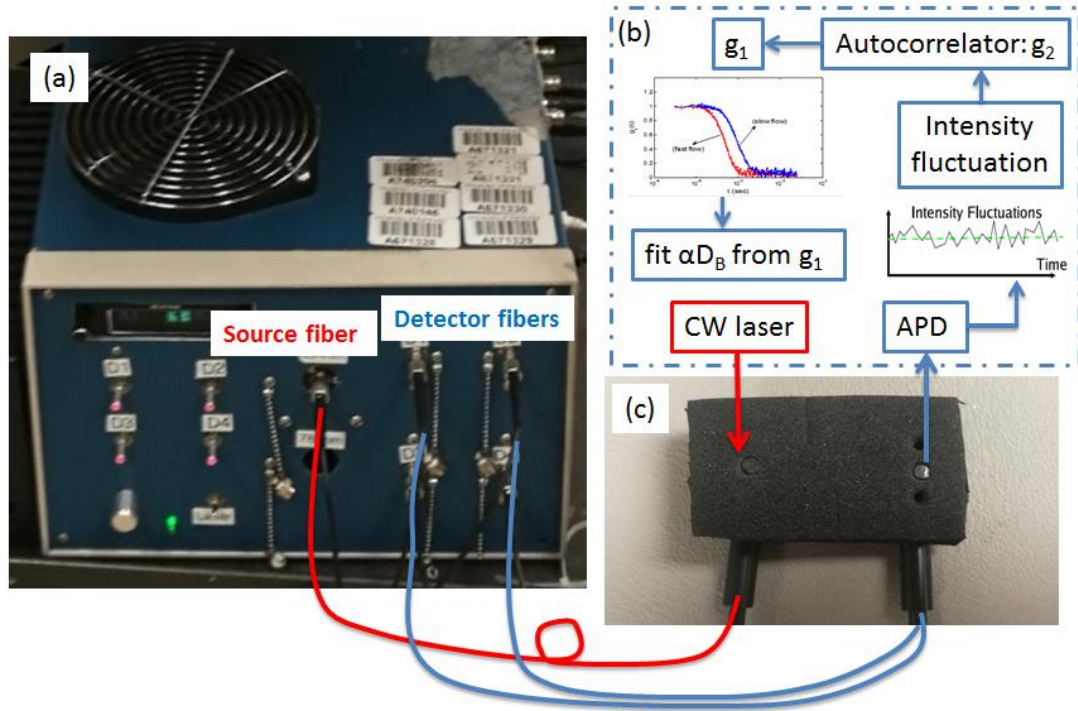


Figure 2.3 DCS device and probe.

(a) A 4-channel DCS device; (b) Schematic of DCS; (c) DCS probe. DCS: diffuse correlation spectroscopy.

The laser and APDs are connected to tissue surface through optical fibers. A fiber-optic probe is usually made with foam pad to confine source and detector fibers (Figure 2.3c). The S-D separation along the tissue surface is selected according to the specific applications. Same as NIRS, the penetration depth is typically half of the distance between source and detector.

During a measurement, the laser diode shines the NIR light through a source fiber (multi-mode fiber, diameter = 200 μm) into the tissue (**Figure 2.3b**). The temporal light intensity variations caused by the moving scatterers in a single speckle area are detected by detector fiber(s) (single-mode fiber, diameter = 5 μm) connected to the APD(s). The output of the APD is sent to the autocorrelator board to calculate the normalized light intensity temporal autocorrelation function (g_2). g_2 at each delay time (τ) is saved to data log and used to extract αD_B in post processing (see data processing diagram in **Figure 2.3b**).

2.2.3 Hybrid NIRS/DCS

In order to measure blood flow and oxygenation simultaneously, our lab built the hybrid NIRS/DCS. **Figure 2.4** shows the picture and diagram of the hybrid NIRS/DCS instrument [26-28, 71]. Computer-controlled TTL signals were used to trigger the Imagent and DCS devices working sequentially. A 50 ms delay between the transition of Imagent and DCS measurements was set to avoid the potential interference between the two devices. The hybrid fiber-optic probe was modified based on the commercial Imagent probe (**Figure 2.5**) by housing the DCS source and detector fibers into the Imagent probe. The optical fibers for the DCS measurement were arranged in the pattern shown in **Figure 2.5** for minimal interference between DCS and NIRS measurements, and for flexible selection of S-D separation for blood flow measurement (1.5 cm to 2.5 cm). Acquisition times for NIRS and DCS measurements can also be varied based on the needs for specific applications.

In addition to simultaneous measurements of BF and tissue oxygenation, the hybrid NIRS/DCS allows for calculation of rVO_2 : $rVO_2 = (100 - StO_2)/(100 - \text{resting } StO_2) \times rBF$, which is a critical parameter for assessment of tissue viability.

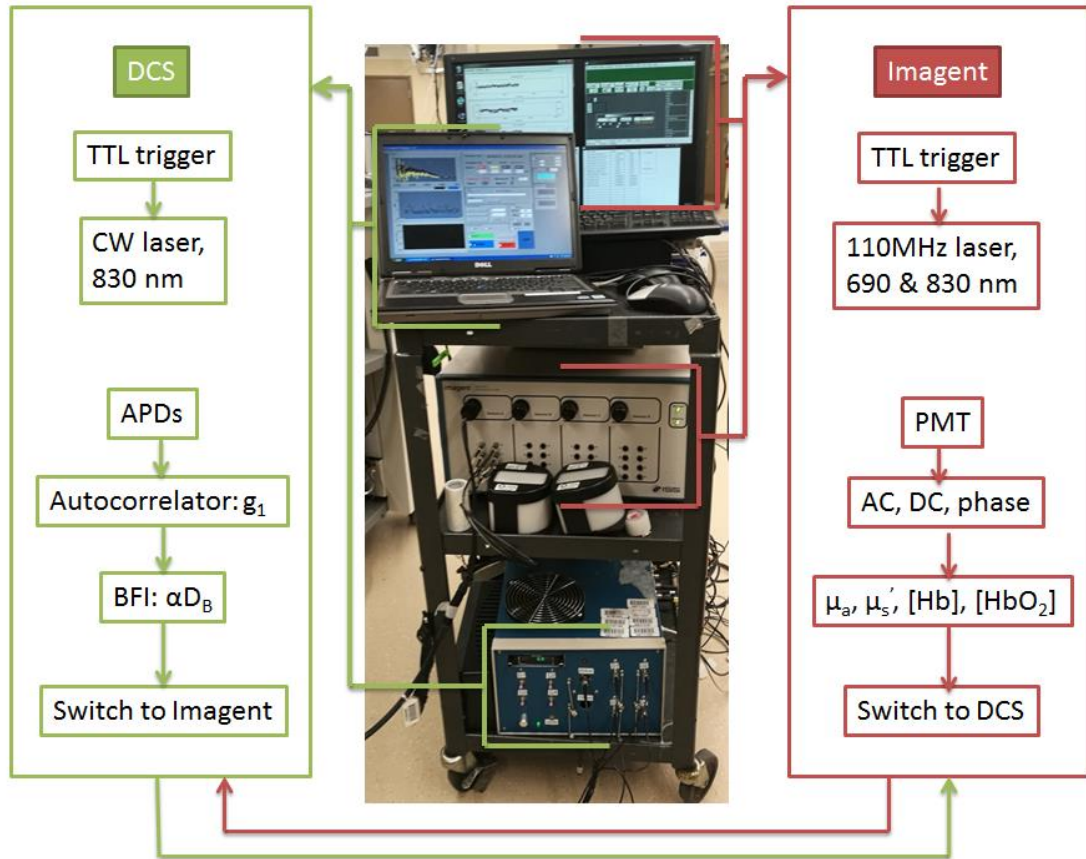


Figure 2.4 hybrid NIRS/DCS device.

The hybrid NIRS/DCS consists of a commercial FD-NIRS (Imagent, right) and a 4-channel DCS flowmeter (left). The Imagent and DCS work alternatively and communicate with each other through TTL signals. NIRS: near infrared spectroscopy, DCS: diffuse correlation spectroscopy, FD: frequency domain.

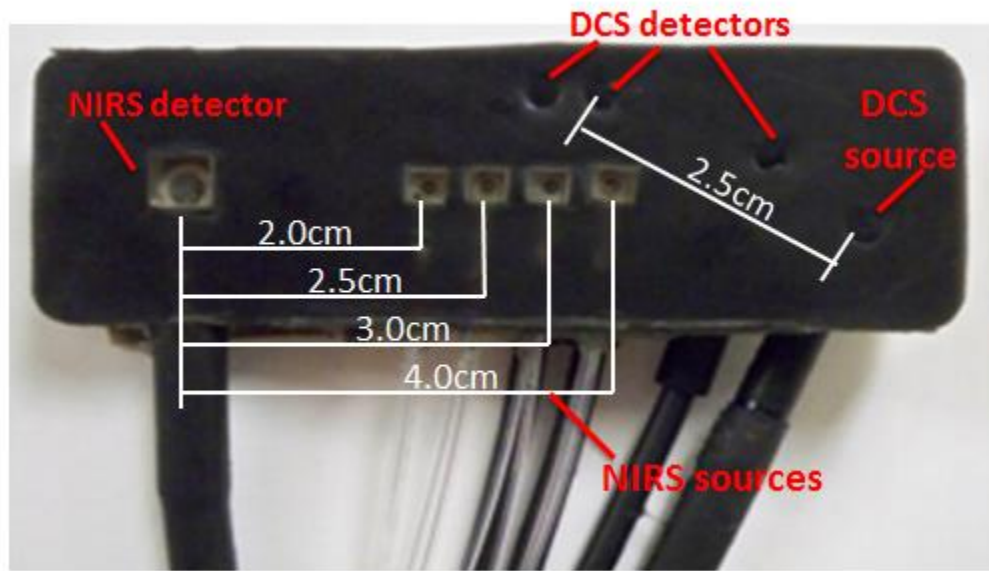


Figure 2.5 Fiber-optic probe for hybrid NIRS/DCS device.

The hybrid probe is made based on the commercial Imagent probe by inserting DCS source and detector fibers into the probe. Several slots have been created for flexible selection of source-detector separation(s) for DCS measurement. NIRS: near infrared spectroscopy, DCS: diffuse correlation spectroscopy.

2.2.4 Occlusive calibrations for absolute oxygen consumption rate (VO_2) and BF

Each subject was placed in sitting position with the right foot secured to a dynamometer (Primus, BTE, Hanover, MD) foot plate (**Figure 2.7**). The fiber-optic probe for NIRS/DCS was attached to the belly of the calf muscle. A pressure/occlusion cuff (Zimmer ATS 1000, Indiana) was affixed to the thigh of the right leg. The optical probe was then secured to the medial gastrocnemius. Then a series of occlusion were completed. The protocol is illustrated in **Figure 2.8 (a)**. A 3-min baseline period was recorded by the hybrid NIRS/DCS to ensure hemodynamic stability. After the baseline measurement, three venous occlusions (VO) (50 mm Hg tourniquet pressure for 10 s) were performed, each with 1 min in between to allow tissue hemodynamics return to

rest. Upon completion of the three VOs, a single arterial occlusion (AO) (~250 mmHg) was performed for 3 min. Subject recovery was monitored following the AO for 5 min.

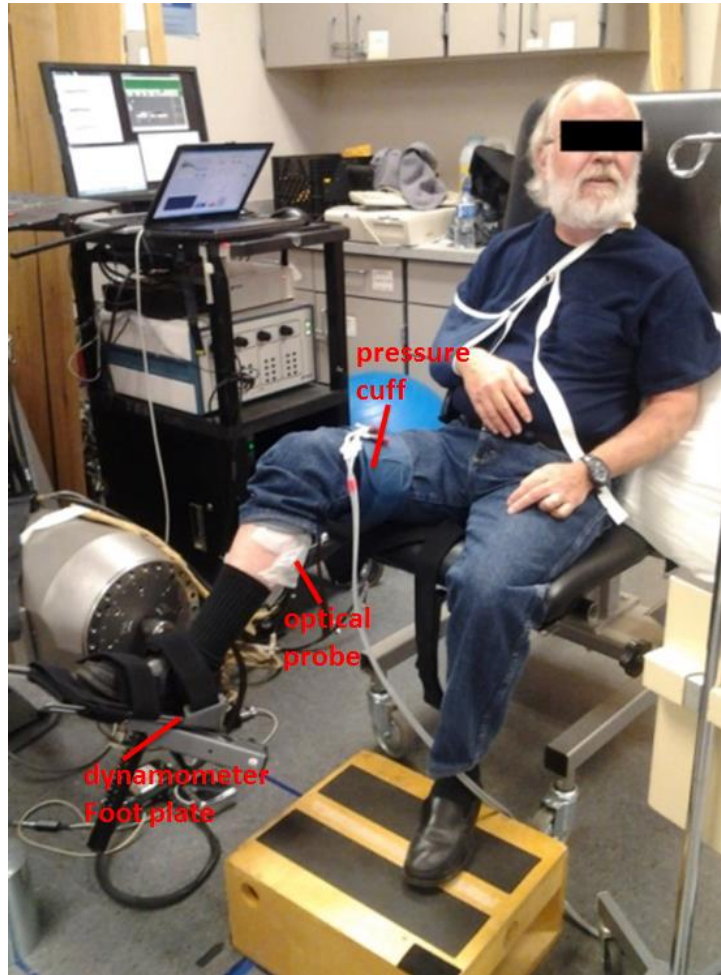


Figure 2.6 Hybrid NIRS/DCS measurements of exercising gastrocnemius with occlusive calibrations and gating algorithms.

Baseline absolute BF was obtained by fitting the slope of the THC increase measured by NIRS during VO (**Figure 2.7 (b)**) [27, 73]. The three slopes were then averaged as the absolute BF. Baseline absolute VO_2 was calculated by fitting the slope of the difference between $[\text{HbO}_2]$ and $[\text{Hb}]$ during the first minute of AO (**Figure 2.7 (c)**) [26, 92].

Finally, the time-course rBF and rVO₂ data were calibrated to absolute BF and VO₂ by multiplying the absolute baseline BF and absolute baseline VO₂ obtained through the VO and AO protocols, respectively.

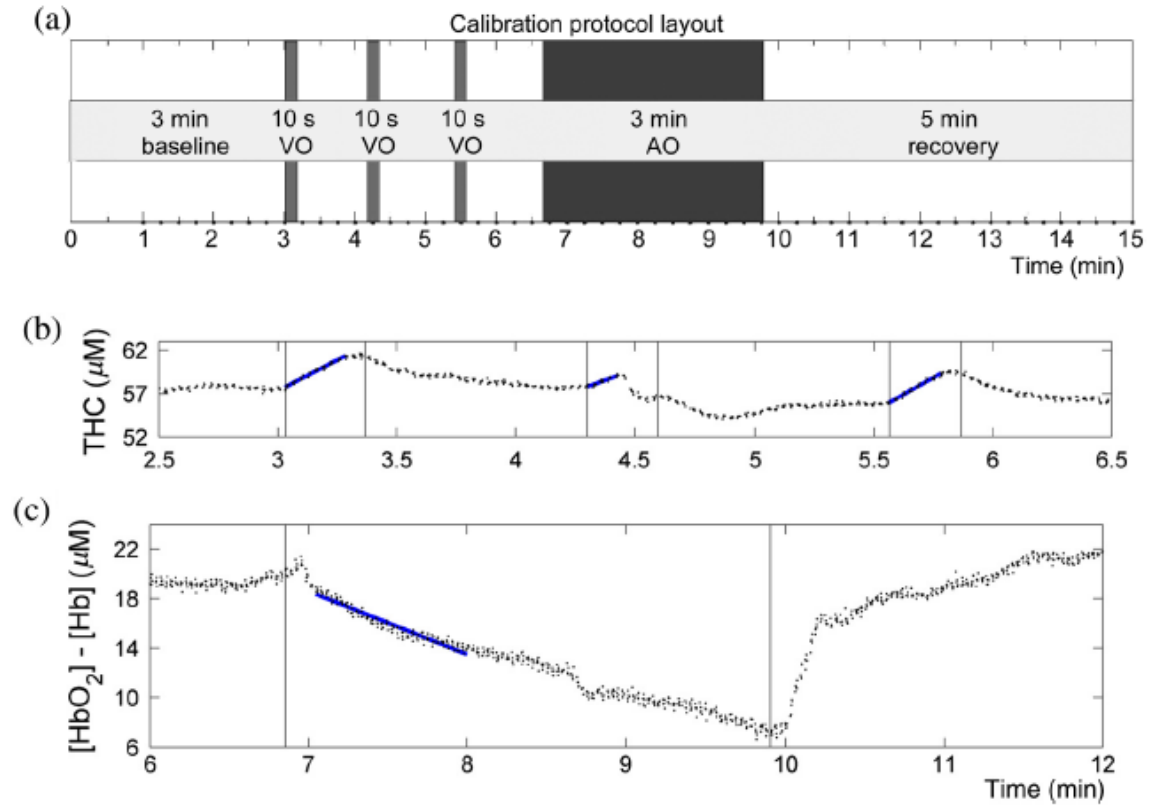


Figure 2.7 Occlusive calibrations for absolute BF and VO₂.

(a) Protocol illustration. (b) THC slope during VO was used to calculate baseline BF. (c) [HbO₂] - [Hb] slope during AO was used to calculate baseline VO₂. THC: total hemoglobin concentration, [HbO₂]: oxy-hemoglobin concentration, [Hb]: deoxy-hemoglobin concentration, VO: venous occlusion, AO: arterial occlusion,

2.2.5 Gating algorithm

The gating algorithm was designed to reduce the influence of muscle fiber motion on DCS measurements [27, 28, 37]. The logic of the gating algorithm is illustrated in

Figure 2.8. The algorithm determines muscle contraction status during plantar flexion based on an analog voltage output of foot pedal position from dynamometer (blue curve in **Figure 2.8**). The analog voltage output decreased with foot/pedal position changes during plantar flexion and increased back when the foot/pedal was bouncing back to resting position.

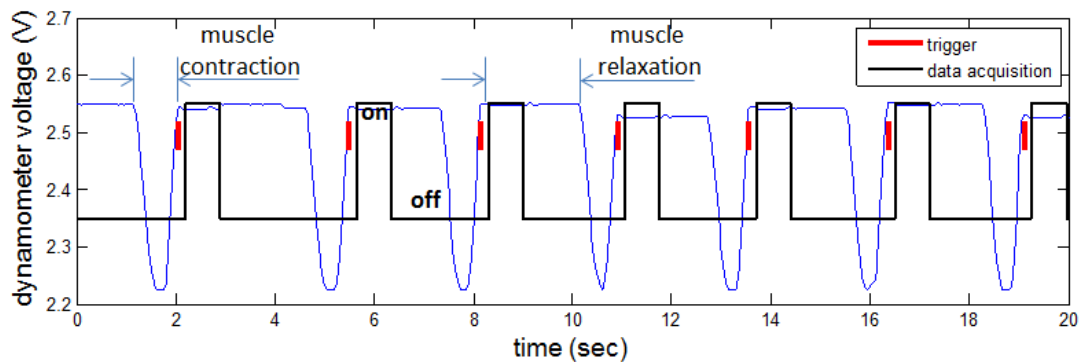


Figure 2.8 Illustration of gating algorithm.

The blue curve represents the signal from dynamometer voltage output, indicating foot pedal position. Red marks in each cycle illustrate triggers determined by a threshold. The hybrid NIRS/DCS collects data during muscle relaxation (inside the black square) between contractions.

Each time the voltage surpasses a threshold when the foot/pedal bounced back indicating muscle status changing from contracted status (low voltage) to relaxed status (higher voltage plateau), a trigger signal will be sent to DCS. After a short delay (50 ms) to allow for residual motion, DCS then begins recording data. After DCS finishes data collection, NIRS will be triggered to collect data. After a complete frame had been collected by the hybrid NIRS/DCS, the algorithm waits for the next rising edge in the position signal to trigger the next data collection sequence. Thus, DCS sampling window

is constrained to the rest period between each cycle of muscle contraction during exercise period. In this study, DCS sampling time was about 600 ms, and NIRS sampling time was about 300 ms, together with some communication time in between, the total sampling time for each frame of the hybrid NIRS/DCS was around 1 second.

2.2.6 Fatigue gastrocnemius plantar flexion protocol

Subjects were seated on a dynamometer (BTE Primus RS, Maryland) with the calf exposed for easy placement of the fiber-optic probe of NIRS/DCS (**Figure 2.6**) [26, 28]. The right foot was placed and secured in the plantar-flexion attachment. Following a warm up to familiarize the subject with the plantar flexion movement, maximal voluntary isometric contractions (MVC) were completed to determine the maximum torque generation. The highest concentric plantar-flexion peak-torque value is recorded as the final MVC. After MVC test, the fiber-optic probe for NIRS/DCS was attached to the belly of the calf muscle. Gastrocnemius hemodynamics, including blood flow (BF), blood oxygen saturation (StO₂), and oxygen consumption rate (VO₂), were then continuously monitored before, during and after the fatigue exercise [26, 28]. Three minutes of resting status data was first taken prior to the start of fatigue exercise. During the fatigue exercise, subjects were asked to complete 75 repetitions of isotonic concentric plantar-flexion contractions at maximal voluntary angular velocity with torque set to 35% of MVC. During the exercise, the previously described gating algorithm (**Chapter 2.2.5**) was used to automatically collect hemodynamic data at an eccentric phase pause (by reading foot pedal angular position) prior to every plantar-flexion contraction to

reduce the motion artifact. Foot pedal position and torque were also continuously recorded during the exercise (**Chapter 2.5.1**). After completion of the exercise, 15 minutes recovery was recorded.

Gastrocnemius BFI was extracted from DCS data. For this study, S-D separation for DCS was set at 2.5 cm (**Figure 2.5**) so that the detected signal would be primarily from skeletal muscle layer rather than subcutaneous adipose tissue. A 4-in-1 detector fiber was used that four fiber cores were integrated together on one end and were plugged at the same location (4 different single speckle areas that were $\sim 5 \mu\text{m}$ apart from each other) in the probe, while the other end of each fiber were connected to one of the four APDs. Therefore, in the post processing, a spatial average was used to average DCS data from the 4 channels at the same time frame to increase the SNR before extracting αD_B .

StO₂ was calculated from NIRS data at multiple separations (2.0–3.5 cm). rBF was calculated by normalizing BFI at all time frames to the averaged BFI (assigning 100%) during the last 2 min prior to the exercise [28]. Resting StO₂ was calculated as an average of StO₂ during the last 2 min prior to exercise. ΔStO_2 was calculated as the increase of StO₂ at all measurement times from resting StO₂ to minimize the influence of individual variation in resting StO₂ and to enhance the StO₂ response induced by the fatigue exercise. The rVO₂ was calculated as $r\text{VO}_2 = (100 - \text{StO}_2)/(100 - \text{resting StO}_2) \times r\text{BF}$. Recovery half-time (T50) of rVO₂ was calculated as the time interval from the end of exercise to the time that they reached a half-maximal value to characterize post-fatigue exercise recovery [27].

2.2.7 Monitoring of muscle hemodynamics during fatigue gastrocnemius plantar flexion in older adults with vitD insufficiency

This was a 13-week double blinded placebo, controlled study. The experimental protocol was approved by the University of Kentucky (UK) Institutional Review Board (IRB). Subjects in normal weight to class I obese (body mass index = 18.5 to 34.9 kg/m²) between 60 to 80 year-old and with vitD insufficiency (25(OH)D \leq 32 ng/mL) were recruited. Subjects who passed the screening were randomized into one of the 4 group assignments: vitD repletion + aerobic training (DAT), aerobic training (AT), vitD repletion alone (D) and control (CTL).

Before (week 0) and after (week 13) the intervention, muscle hemodynamics during fatigue exercise was measured using the hybrid NIRS/DCS for each subject. The occlusive calibration was first done to quantify baseline BF and VO₂ with the method introduced in **Chapter 2.2.4**. Then gastrocnemius hemodynamics during fatigue plantar flexion protocol (**Chapter 2.2.6**) was measured. rBF, rVO₂, StO₂, Δ StO₂ and T50 of rVO₂ were calculated as introduced in **Chapter 2.2.6**.

ANOVA and paired t-tests were used to evaluate the intervention effects. Values were presented as mean \pm standard error of mean (SEM).

2.3 Results

Thirty-seven subjects completed the intervention and participated in both baseline (week 0) and endpoint (week 13) measurements. **Figure 2.9** shows a typical

hemodynamic responses profile in rBF, rVO₂, and StO₂ in subjects during fatiguing exercise.

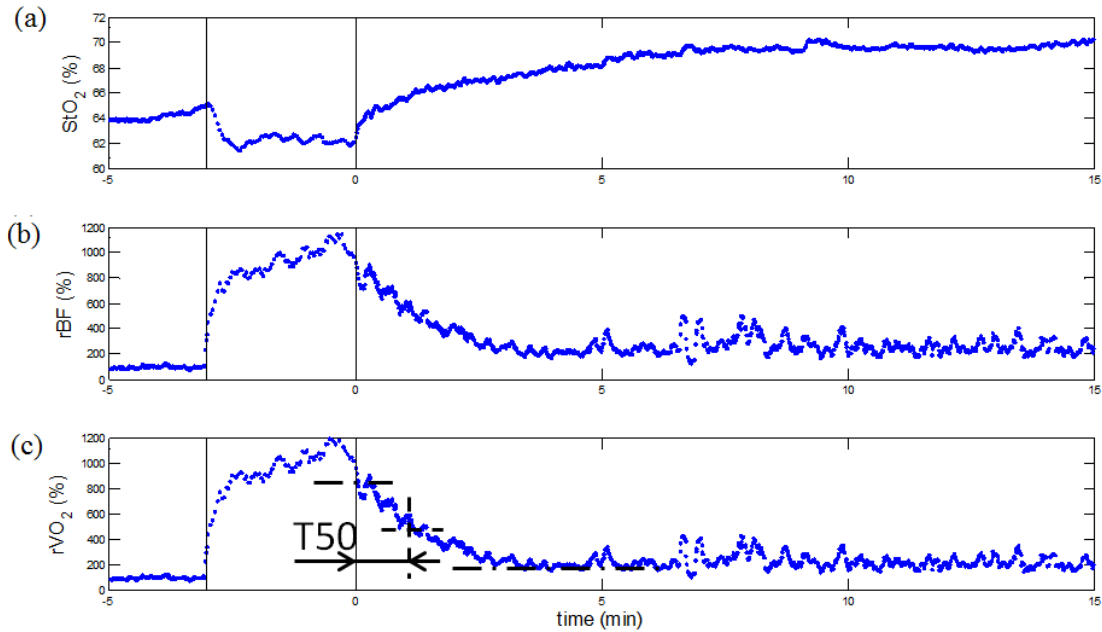


Figure 2.9 Typical muscle hemodynamic responses to exercise.

Representative profile of (a) blood oxygen saturation (StO₂), (b) relative blood flow (rBF), and (c) relative oxygen consumption rate (rVO₂) in a subject throughout the fatiguing exercise. Solid vertical lines indicate the beginning and the end of fatiguing exercise. Half recovery time (T50) definition is demonstrated in (c).

At baseline prior to the intervention, there were no differences in blood flow during the fatiguing exercise protocol between groups; however endpoint comparisons showed significant group differences ($p = 0.04$, ANOVA) (**Figure 2.10(a)**). DAT had significant higher blood flow during exercise than CTL ($p = 0.01$) and AT ($p = 0.01$). Similar trend were found in rVO₂ during exercise. rVO₂ during exercise of DAT was significantly higher at endpoint than CTL ($p = 0.007$), AT ($p = 0.002$), and D ($p = 0.013$, ANOVA) (**Figure 2.10(b)**). No significant differences in StO₂ were found between intervention groups during exercise at baseline or endpoint.

Upon finishing the fatiguing exercise, hemodynamic variables began to return towards their pre-exercise levels: rVO_2 and rBF decreased during recovery, and StO_2 increased during recovery. Throughout the 15 minutes of recovery, there were no significant differences in rBF , rVO_2 , or StO_2 by time or by group ($p>0.05$, RMANOVA). To further explore the intervention effects on StO_2 we examined shifts in ΔStO_2 from baseline to endpoint for each minute of recovery (minutes 1-15). Within group comparisons showed that DAT was the only group had significant reduce in ΔStO_2 towards full recovery from baseline to endpoint (**Figure 2.11(a)**). The observed DAT group trends became stronger from minutes 1 to 6 in recovery phase. Significance was attained ($p<0.05$, paired t-test) at minute seven and continued throughout the rest of recovery. Statistical differences are represented by an average of ΔStO_2 during the final minute of recovery (**Figure 2.11(b)**).

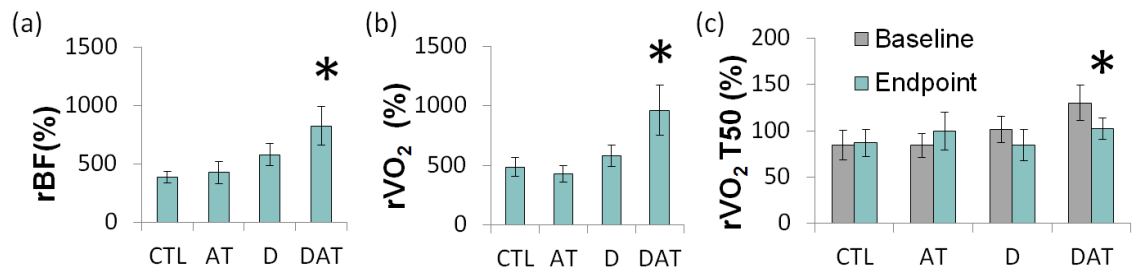


Figure 2.10 Hemodynamic responses to 13 weeks of intervention.

(a) Endpoint (week 13) relative blood flow (rBF) during exercise by group (AT: aerobic training; CTL: control; D: vitamin D; DAT: vitamin D + aerobic training). (b) Endpoint (week 13) relative oxygen consumption rate (rVO_2) during exercise by group. (c) Recovery half-time (T50) of rVO_2 at study baseline (week 0) and endpoint. Bars represent mean \pm SEM.

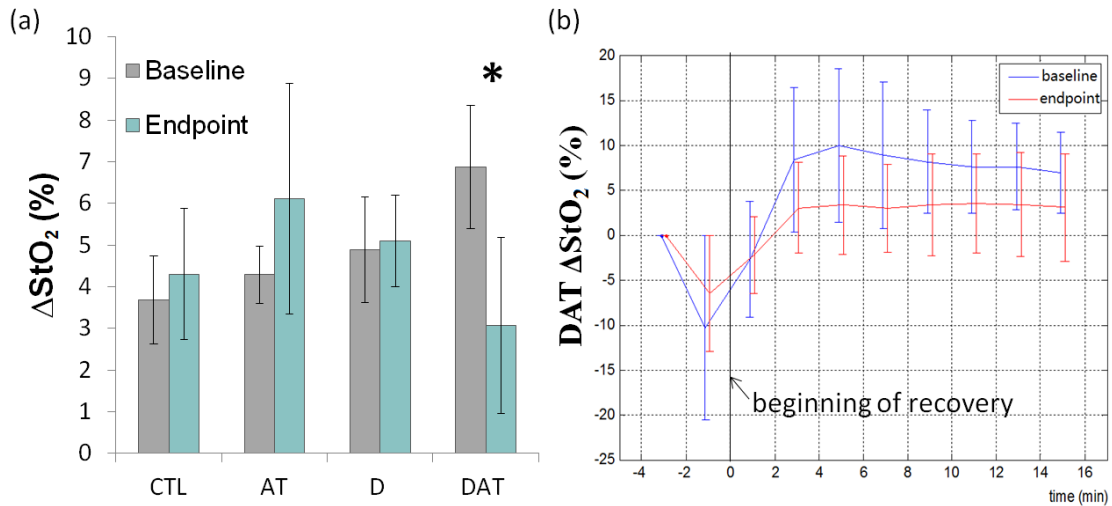


Figure 2.11 Muscle blood oxygen saturation responses to 13 weeks of intervention in post-exercise recovery.

(a) Change in oxygen saturation (ΔStO_2) by group at study baseline (week0) and endpoint (week 13) in post-exercise recovery (AT: aerobic training; CTL: control; D: vitamin D; DAT: vitamin D + aerobic training). (b) DAT: group average of ΔStO_2 at baseline and endpoint during and post exercise. Bars represent mean \pm SEM.

For $r\text{VO}_2$ T50, paired t-tests showed a significant decrease in only DAT (-28.7 ± 31.3 seconds, $p=0.03$) (**Figure 2.10(c)**). However, there were no differences among groups in StO_2 T50 ($p>0.05$). Due to rapid change, the recovery half time of blood flow was not calculated.

Lastly, no significant changes in torque or in absolute BF, absolute VO_2 were observed.

2.4 Discussion and conclusions

We have developed a hybrid NIRS/DCS system for simultaneous and continuous monitoring of tissue oxygenation and BF. Simultaneous measurements of NIRS and

DCS enable quantification of skeletal muscle rVO_2 . The novel occlusive calibration techniques and the gated dynamometer exercise protocol that have been previously applied on forearms have been tailored to the lower limb for the first time in this study [26-28, 93]. Occlusive calibrations make it possible to quantify absolute values of BF and VO_2 . We also developed an exercise protocol for lower limb that is comparable in duration and intensity to other studies and could be done by both healthy subjects and PAD patients [28]. Innovative gating algorithms significantly reduce motion artifacts and improve the accuracy of BF measurements during exercise. The removal of these artifacts means that DCS can produce rapid, continuous examination of microvascular muscle BF during exercise, which is a unique functionality of the system.

We have successfully applied the hybrid NIRS/DCS for the characterization of muscle hemodynamics during and post gastrocnemius fatiguing exercise in an older healthy active population with vitD insufficiency. The DAT intervention had significant effects on rBF , StO_2 , and rVO_2 T50. We examined shifts in ΔStO_2 from study baseline to end study to better represent StO_2 response to exercise. DAT was the only group that had significant decrease in ΔStO_2 during the recovery (min 7-15). A reduction in ΔStO_2 indicates an enriched mitochondrial capacity by increasing oxygen extraction to muscles [27]. DAT was the only group experienced a significant decline in rVO_2 T50 over time (baseline to endpoint), which could be attributed to a beneficial alteration of muscle oxygen utilization, suggesting improved mitochondrial function. Together, these changes in hemodynamics and oxygen consumption may be attributed to multiple mechanisms including improved muscle blood flow and oxygen delivery creating a reduction in

oxygen debt, improved lipid substrate availability to the mitochondria, and direct improvements of mitochondrial function [94].

In summary, NIRS/DCS data show increased rVO₂ and rBF in response to fatiguing exercise and faster recovery after exercise in subjects receiving DAT. This suggests that combining aerobic exercise with vitD repletion may help improve muscle metabolic function. The hybrid NIRS/DCS instrument effectively measures muscle hemodynamic and metabolic changes during and after exercise, and has potential for continued high impact in translational studies combining techniques to comprehensively understand skeletal muscle function.

2.5 APPENDIX: Other engineering work

2.5.1 Torque and position data acquisition

As mentioned in **Chapter 2.2.6**, torque and foot pedal position were recorded during exercise. Torque and position were provided by the dynamometer as analog outputs (voltage, 0 to 3.3 V). An Arduino based data acquisition system was built to monitor and save the data.

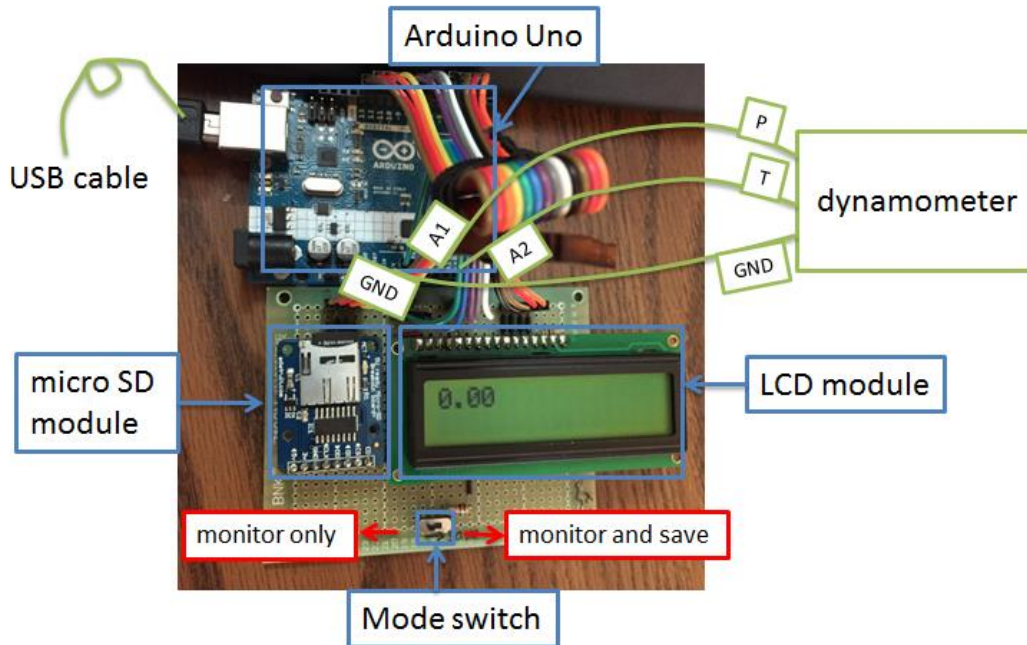


Figure 2.12 Torque and position data acquisition system.

The system is composed of Arduino Uno board, micro secure digital (SD) card module, LCD module and a mode selection switch. Cable connections with dynamometer are marked: Uno analog input channel 1 (A1) and channel 2 (A2) are connected to dynamometer analog output channels of position signal (P) and torque signal (T). The ground (GND) of dynamometer and Uno are also connected.

The system composition and cable connection are shown in **figure 2.12**. Arduino Uno was selected for this project to cover all the needs. Analog input channel 1 and 2 of Uno were employed to record position and torque signal respectively. A liquid crystal display (LCD) screen was connected with Uno for data monitoring in real time. A mode selection design was realized by a switch to select “monitor only” or “monitor and save” mode. A micro secure digital (SD) card module was integrated into the system to save the data.

Uno was programmed to realize the following function. When the system was powered, Uno first checked the status of the micro SD card, an error message would pop

out on LCD if the micro SD card was not in place. After initialization, the LCD displayed the real time torque and position data in number, refreshed at 20 Hz. Data saving started when the switch was pushed to “monitor and save” mode; A new txt file was created at the same time in the micro SD card and Uno wrote torque and position data in 2 separated columns into the file at 20 Hz until the switch was pushed back to “monitor only”.

2.5.2 Automatic recognition of torque peak

Torque peak of each plantar flexion cycle during the exercise were calculated as a secondary outcome of the measurement. An automatic torque peak recognition algorithm with a graphical user interface (GUI) was developed using MATLAB to improve the accuracy and free the labor form manual recognition and data logging.

The algorithm first converted the raw voltage signal of position and torque collected with the above-mentioned system into meaningful values with correct units after importing the raw data file. Then the 75 cycles were segmented using position signal because position had more regular periodic pattern comparing with torque signal. The torque peak value within each cycle was then calculated. The GUI displayed time sequence of torque signal during exercise with torque peaks marked (**Figure 2.13**) and allowed minor manual corrections (optional) by adding or removing torque peak points. A cursor was provided to select the point to add/remove. The selection did not need to be exact: the algorithm would allocate the nearest cycle/target to process. After finalizing all torque peaks, results were saved to a txt file with assigned file name through the GUI.

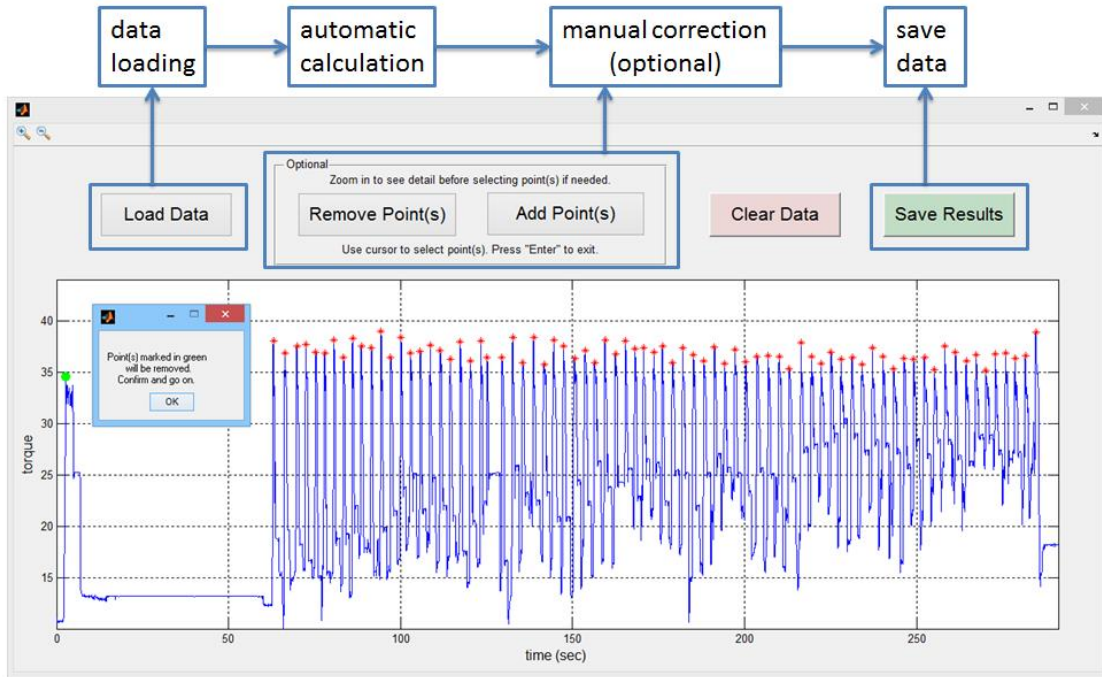


Figure 2.13 Graphical user interface (GUI) for automatic recognition of torque peak.

The GUI for automatic torque peak recognition is shown with workflow marked above. The figure gives an example of manual removal of selected data point.

CHAPTER 3. NONCONTACT DIFFUSE CORRELATION SPECTROSCOPY/TOMOGRAPHY (NCDCS/NCDCCT) FOR IMAGING OF MASTECTOMY SKIN FLAPS AND CHRONIC WOUNDS

3.1 Introduction

Skin flap necrosis is the most common complication after mastectomy and expander-implant based breast reconstruction, with an incident rate of up to 20% [6, 7, 42]. Occurrence of flap necrosis is associated with insufficient blood supply in flap to meet the metabolic needs. Quantification of blood flow (BF) in mastectomy skin flaps is important for the prediction and early salvation of the flap necrosis. Fluorescence angiography has been used to measure tissue surface perfusion in the flap which may not reflect BF in deep tissue of the skin flap. Also, measurements with fluorescence angiography require invasive intravenous injection of dye. Furthermore, fluorescence signal is transient and thus not suitable for continuous monitoring [13-15]. Fluorescence imaging has been reported to over- or under-predict skin flap necrosis [15]. Therefore, a technique for noninvasive and continuous quantification of flap BF is desired.

Chronic wounds affect more than 5 millions of Americans each year, among which the prevalence of limb chronic ulceration approaches 15 percent and this number keeps increasing [95]. The majority of chronic wounds can be classified into the following three categories accordingly: diabetic foot ulcer, pressure ulcer, and venous and arterial ulcers [3, 96]. Diabetic foot ulcers occur in 12 to 25 percent of patients with diabetes [97]. Shunts in the microcirculation, together with the presence of neuropathy, may lead to abnormal distribution of BF, which contributes to the wound development

and disturbs the healing of the wound site [98]. Pressure ulcer occurs after tissue is compressed over time. It originates from bone and develops upward to skin. Prolonged pressure applied to the wound site reduces blood perfusion, which is a key factor to prevent pressure ulcer from healing [4]. Peripheral arterial disease (PAD) is another major cause of chronic wounds because of ischemia due to micro circulation impairments. About 10 percent patients with PAD undergo vascular surgery to improve perfusion in their limbs [99]. Adequate perfusion and hemodynamic success are not only important judgment for revascularization surgery success, but also mandatory for healing of chronic wound [100]. Again, a noninvasive portable device for reliable measurements of BF distributions in wounds is needed for the diagnosis and treatment monitoring.

For vulnerable tissues like skin flaps and wound tissues, contact measurements are not appropriate due to the risk of contact infections. On the basis of diffuse correlation spectroscopy (DCS) technique, we developed an innovative noncontact diffuse correlation spectroscopy and tomography (ncDCS/ncDCT) system for noncontact spectroscopic and tomographic measurements of blood flow distributions in relatively deep tissues [39, 41-43, 101]. The ncDCS/ncDCT system employs optical lens to project DCS sources and detectors on the tissue surface. A noncontact probe is mounted on a motorized-drive linear stage for mechanical scanning over a selected region of interest (ROI) for tomographic measurements. A finite element method (FEM) based diffuse correlation tomography (DCT) image reconstruction algorithm has been developed based on a modified open-source software package NIRFAST, which was originally designed for diffuse optical tomography (DOT) reconstruction [39, 41]. The ncDCS/ncDCT system has been validated in tissue-like phantoms and in *in vivo* tests. It has also been

applied for imaging of breast tumors and head/neck free tissue transfer flaps [39, 41, 82, 101].

In this project, I optimized and applied ncDCS for spectroscopic measurements of BF in mastectomy skin flaps intraoperatively with the hypothesis that ncDCS measurement could provide intraoperative BF data to enable the prediction of mastectomy skin flap necrosis [43]. I also applied ncDCT for tomographic imaging of BF distributions in chronic wounds to measure the BF contrast between wound tissue and normal tissue.

3.2 Methods

3.2.1 ncDCS/ncDCT instrumentation

The ncDCS/ncDCT probe for noncontact blood flow measurement is shown in **Figure 3.1**. The noncontact probe has two identical laser source paths and one shared detector path in the center arranged in a linear array (**Figure 3.1**) [39, 41-43]. In each source path, laser light delivered through a multimode source fiber is projected onto the tissue surface through lens system (Figure 3.1). Fifteen single-mode detector fibers are evenly distributed in 7 mm to cover a 20 mm range on the focus plane (measurement surface) through the lens magnification (**Figure 3.1**). With this setup, the source-detector (S-D) separations range from 10 to 30 mm, which enables maximum penetration depth of ~15 mm (half of the S-D separation) [78, 81].

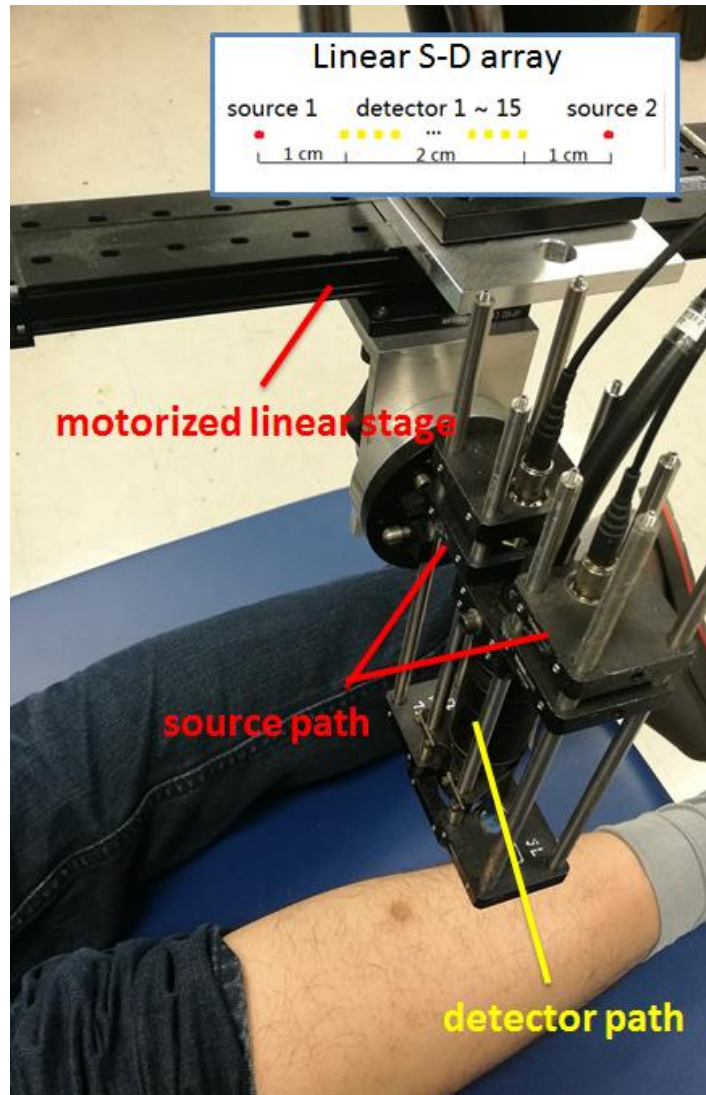


Figure 3.1 ncDCS/ncDCT probe and experimental setup for wound imaging.

There are two separated source paths and one shared detector path integrated in the probe. Sources and detectors are projected/focused to tissue surface through lens apparatus. The noncontact probe is fixed to a motorized linear stage at ~10 cm above tissue surface. S-D: source-detector.

This noncontact probe is connected to a DCS flowmetry device through optical fibers. Photons emitted from lasers are injected through the source path into the tissue sample. Photons travel through the tissue and reflect back to detectors (avalanche photodetector (APD)) through detection path. The correlator takes the APD outputs and

calculates the light intensity autocorrelation functions, which are used to extract tissue blood flow information.

The noncontact optical probe is mounted on a linear motorized stage which is fixed to a multiple axis stand holder for flexible adjustment of probe position. The motorized stage can be fixed at one location for spectroscopic measurements or driven linearly using computer program for linear scanning over the ROI for tomographic measurements.

3.2.2 DCT reconstruction

Surface geometry acquisition and mesh generation. FEM-based DCT reconstruction requires incorporating a finite element mesh to represent the imaged tissue volume and to denote locations of the sources and detectors along the surface [39-41]. For some simple cases, we may use a mesh with simple geometry, such as sphere or slab shape, to approximate the tissue geometry. While for many cases, the tissue surface geometry is complicated and requires more accurate geometry characterization for better reconstruction.

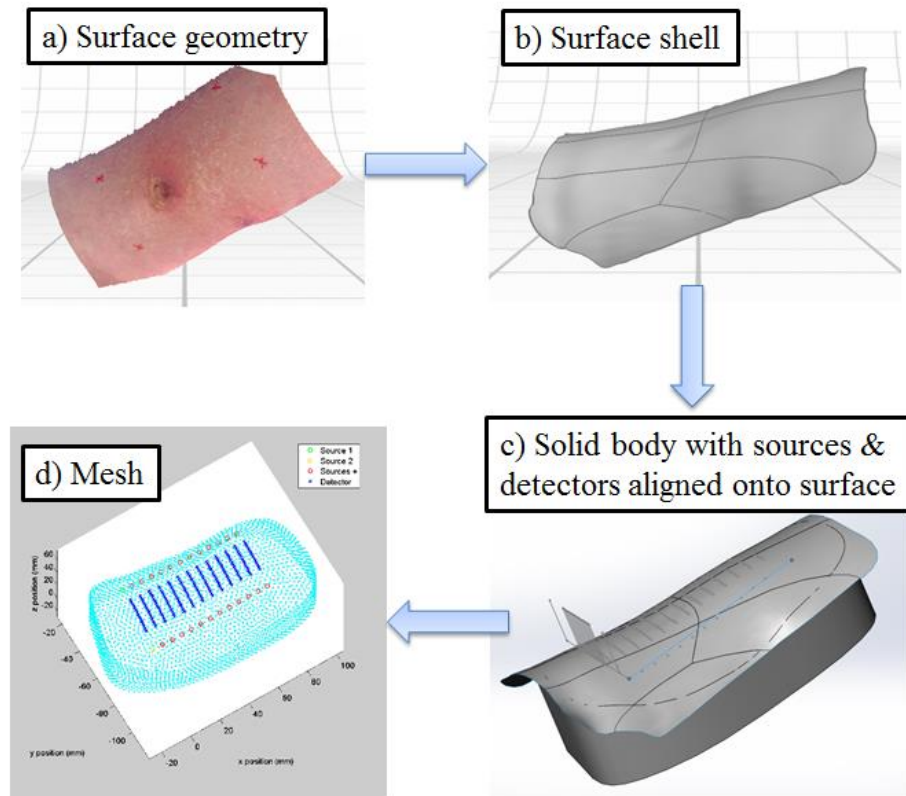


Figure 3.2 Mesh generation.

The surface geometry (a) captured by the 3D camera is used to generate a surface shell (b). A solid body (c) representing the measured tissue volume is generated from the surface shell. Source and detector locations are calculated on the surface of the solid model based on the marks. Finally, the solid model is divided into a solid mesh (d).

In this study, a commercial 3D scanner (NextEngine, CA) was used to scan target sample geometry. The working distance of the 3D scanner was about 17 inches from the sample surface. Prior to geometry acquisition, reference marks were made manually using marker pen on the measurement surface at the projected source locations of the beginning and ending step of the ncDCT scanning (**Figure 3.2 (a)**). These markers were used for assignment of sources and detectors on the mesh surface. During the 3D geometry scanning, a reference plane parallel to the focus plane of ncDCT was included

in the field of view (FOV) of 3D scanner for easy alignment of the geometric information and boundary ncDCT data. The output of the 3D scanner was the tissue surface geometry (**Figure 3.2 (b)**).

A solid model was then created to extend the surface shell into a solid body (SolidWorks, Dassault Systemes, MA) (**Figure 3.2 (c)**). The projected sources and detectors were calculated based on this 3D model and the reference marks made on the tissue surface using a program implemented in SolidWorks interface (**Figure 3.2 (c)**) [40]. Finally, a 3D tetrahedron mesh was generated using ANSYS® (ANSYS, PA) from the solid model created in SolidWorks with an appropriate node distance (typically 2 mm in this study) (**Figure 3.2 (d)**).

Modified NIRFAST for DCT reconstruction. Many DOT methods have been developed for reconstructing 3D tissue heterogeneity from NIRS measurements at multiple S-D pairs [21-23]. For example, NIRFAST is a FEM-based open source software package for DOT image reconstruction [102]. Similar to DOT, DCT reconstructs blood flow image using DCS measurements from multiple S-D pairs. Because of mathematical similarity of the correlation diffusion equation (**Equation 2.7**) and the photon diffusion equation (**Equation 2.2**), the NIRFAST algorithm for DOT was modified and adapted by our group for DCT reconstruction [39, 102]: the term $\frac{1}{3}\mu_s' k_0^2 \alpha(\Delta r^2(\tau))$ in Equation 2.7 was written as $\mu_a^d(\mathbf{r}, \tau) = 2\mu_s' k_0^2 \alpha D_b(\mathbf{r})\tau$, and defined as “dynamic absorption” at correlation delay time τ . DCT was conceptualized as a formulation of continuous-wave (CW) DOT ($\omega = 0$) which computed $G1(\mathbf{r}, \tau)$ instead of photon fluence rate $\Phi(\mathbf{r}, \omega)$, by updating “static absorption” $\mu_a(\mathbf{r})$ to $\mu_a^{total}(\mathbf{r}, \tau) = \mu_a(\mathbf{r})$

+ $\mu_a^d(\mathbf{r}, \tau)$ at a selected τ , and reconstructing $\mu_a^{total}(\mathbf{r}, \tau)$ instead of $\mu_a(\mathbf{r})$ only. The reconstructed μ_a^{total} was used to extract αD_b (blood flow index (BFI)).

Chart 3.1 shows the execution of DCT reconstruction using our modified NIRFAST. First, a mesh representing the imaged tissue volume is loaded. All the sources and detectors according to the actual ncDCT scanning are assigned onto the surface of the mesh. S-D pairs corresponding to the actual tissue boundary are linked to match with the boundary data. Initial guess of BFI and optical properties (μ_a and μ_s') of each mesh voxel, along with the selected $\tau = \tau_0$ are assigned to the mesh. An initial guess of $\mu_a^{total}(\mathbf{r}, \tau_0)$ is then calculated. Boundary BFI data from ncDCT scanning are converted to $g1(\mathbf{r}, \tau_0)$ using **Equation 2.9** and further converted to $G1(\mathbf{r}, \tau_0)$ by multiplying with $G1(\mathbf{r}, 0)$ [39].

We then ran the inverse model with an iterative approach for the reconstruction of spatial distribution of $\mu_a^{total}(\mathbf{r}, \tau_0)$ and BFI [39]. A forward model was first run to calculate the boundary $G1(\mathbf{r}, \tau_0)$ based on the initial guess of the mesh in the first iteration or based on the updated mesh in the following iterations. The discrepancy between the boundary $G1(\mathbf{r}, \tau_0)$ from our measurements and those from the initial/updated data was then calculated and minimized. If the reminding error was larger than the tolerance, an update for $\mu_a^{total}(\mathbf{r}, \tau_0)$ is calculated accordingly. These iterations ran continuously until the remaining error was under the tolerance. Finally, BFI distributions were extracted through the definition of $\mu_a^{total}(\mathbf{r}, \tau)$.

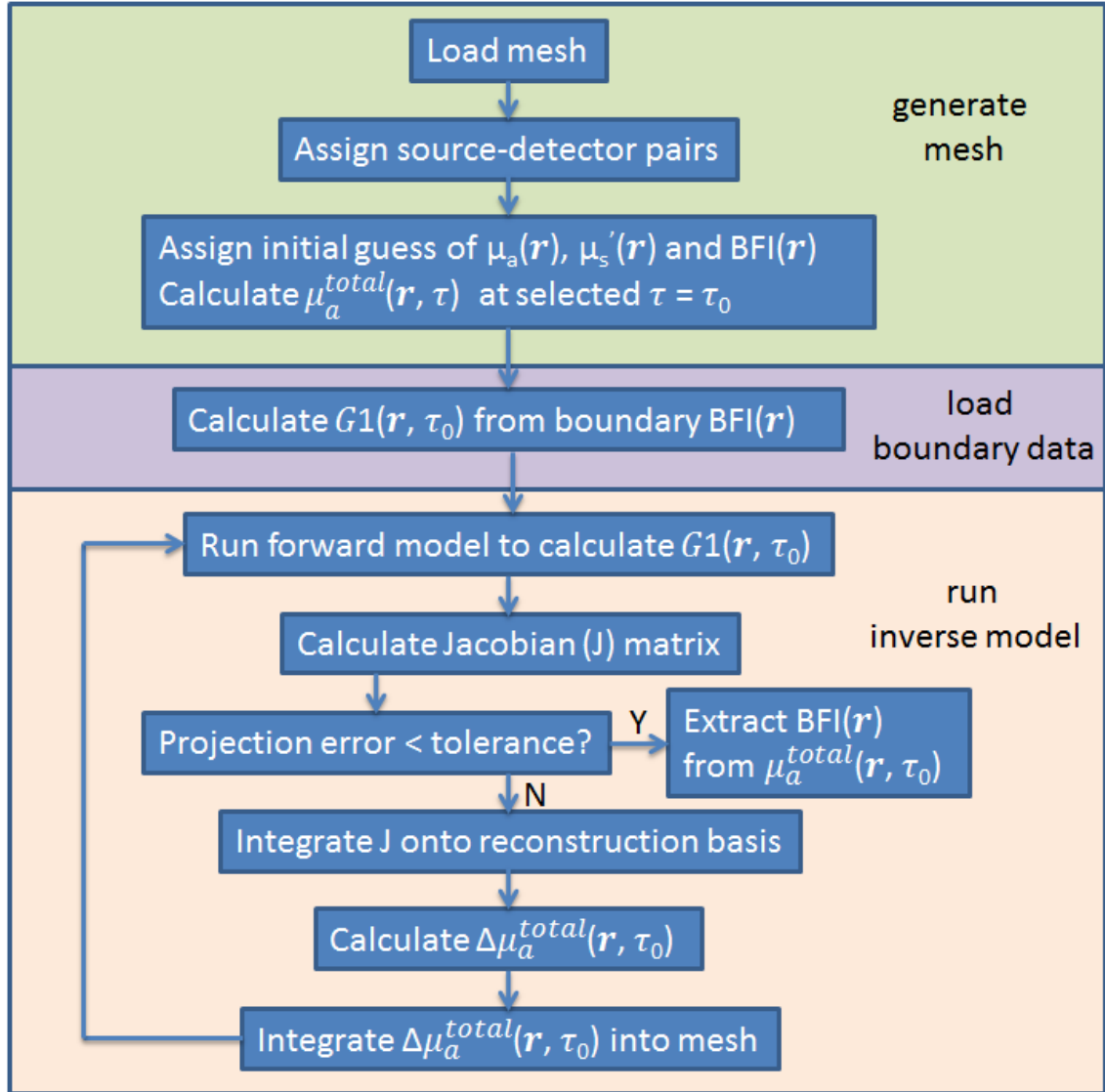


Chart 3.1 Flowchart of the modified NIRFSAT for DCT reconstruction.

3.2.3 ncDCS for measurements of blood flow in mastectomy skin flaps

Patient recruitment. The experimental protocol was approved by University of Kentucky (UK) Institutional Review Board (IRB) (#15-0511-F2L). Female patients over 18 years old undergoing mastectomy and immediate breast reconstruction were recruited from the UK hospital with signed consent form.

Data collection & analysis. For each patient, blood flow was measured at three time points using ncDCS before and immediately after mastectomy, and immediately after breast reconstruction (**Figure 3.3**). For this study, one source path (laser at 785 nm) and 4 detector paths located at 10.0, 14.2, 18.6, and 22.8 mm distances from the source location were used to cover tissue flaps with penetration depths of 5 to 11.4 mm. At each time point, blood flow was measured from two to three equidistant locations along both sides of the edge of the mastectomy incision. Thirty frames of data were taken at each location. Total measurement time at each time point was less than 5 minutes.



Figure 3.3 Mastectomy skin flap measurement setup.

Measurement set up at before (a), immediately after mastectomy (b), and after breast reconstruction (c).

BFI were averaged over all locations and all S-D separations for each time point, and then normalized to the baseline level before mastectomy (assigning “1”) to get rBF. All subjects were followed for at least 5 months for the development of mastectomy skin flap necrosis defined as any area of skin necrosis on the skin flap. Statistical tests for averaged rBF differences at different time points were performed using Welch two sample t-test. The receiver operating characteristic (ROC) curve was constructed and the

area under the ROC curve (AUC) was calculated to evaluate the ability of rBF measurements to discriminate necrosis and non-necrosis groups. All analysis was performed using MATLAB.

3.2.4 ncDCT for 3D imaging of chronic wounds

Patient recruitment. The experimental protocol was approved by UK IRB (#14-0571-F1V). We planned to recruit 20 patients with deep tissue wound (e.g., pressure ulcer, diabetic foot ulcer, arterial ulcer) in total from UK hospital Wound Care Clinic (WCC). Among the 20 subjects, we expected to recruit 10 PAD patients who will undergo revascularization and measure them twice at before and after the surgical intervention to evaluate hemodynamic improvements. The following populations were excluded during subject screening: 1) pregnant females; 2) patients under 18 years old; 3) patients with very limited mobility. Because of the instrumentation limitation (i.e. limited coverage of the ncDCT probe), only patients with wound size under $100 \times 20 \text{ mm}^2$ were considered for this study. Patients who passed our screening and agreed to participant in the study were measured at the UK Center for Clinical and Translational Science (CCTS).

Data collection & analysis. For each measurement, tissue blood flow in the selected wound and the surrounding normal tissue (total coverage of ncDCT scanning on tissue surface: $\sim 40 \times 100 \text{ mm}^2$, centered at the wound) were imaged using the ncDCT system (**Figure 3.1**). For this protocol, both source and detector paths on the ncDCT probe were used for noncontact scanning. Step separation (typically 6 mm) and total number of linear scan steps were determined based on the size of the wound (typically \sim

16 steps in total). Each scanning covered the wound and some surrounding normal tissue (total coverage: $\sim 40 \times 100 \text{ mm}^2$, centered at the wound). At each step, 20 frames of data were obtained.

During the measurement, the patient was asked to lie in the supine position (or bend over if the wound is on the back) to expose the wound site. Subsequently, ncDCT scanning was obtained using the noncontact probe. The scanning time ranged from 4 to 6 minutes depending on the wound size and sampling density. A 3D photo was taken targeting the same location using the commercial 3D scanner to get tissue surface geometry. The actual source positions at the first and last steps were marked during the ncDCT scanning and included in the 3D photo for S-D coordinate. Each measurement took less than 30 minutes, including preparation, ncDCT scanning, 3D photo acquisition and wound bandaging after the optical measurements.

For each measurement, 3D blood flow distribution in the wound and the surrounding normal tissue was reconstructed. The scanning data was processed using Equation 2.5 and 2.9 to get a complete set of boundary αD_b . A mesh with real tissue geometry was generated using the method described in **Chapter 3.2.2**. The DCT reconstruction was done using our modified NIRFAST (**Chapter 3.3.2**). A single delay time $\tau = 3.2 \times 10^{-6} \text{ s}$, and optical properties of $\mu_a = 0.025 \text{ cm}^{-1}$, $\mu_s' = 7.0 \text{ cm}^{-1}$ were used in flow image reconstruction.

3.3 Results

3.3.1 Prediction of mastectomy skin flap necrosis

Nineteen patients were enrolled in the study. Four patients (21%) developed skin necrosis, one of which underwent additional surgery (patient #4). The rBF values immediately after mastectomy and after reconstruction of each patient are shown in **Table 3.1**. The difference in rBF immediately after mastectomy in patients with or without necrosis was statistically significant (**Fig. 3.4 (a)**), with values of 0.27 ± 0.11 and 0.66 ± 0.22 , respectively ($p < 0.001$). rBF values immediately after mastectomy showed a significant high accuracy in prediction of skin flap necrosis, with an AUC of 0.95 (95% confidence interval = 0.81, 1) (**Fig. 3.4(b)**).

Table 3.1 rBF values in mastectomy skin flaps of 19 patients

Patient	Necrosis?	Before mastectomy	After mastectomy	After reconstruction
1	N	1	0.51	1.07
2	N	1	0.51	1.39
3	N	1	0.81	1.36
4	Y	1	0.12	0.35
5	N	1	0.8	0.45
6	N	1	1.05	0.39
7	Y	1	0.37	0.6
8	N	1	0.81	0.58
9	N	1	0.52	0.97
10	N	1	0.24	0.5
11	N	1	0.53	0.72
12	Y	1	0.29	1.16
13	N	1	1.07	0.91
14	N	1	0.76	0.85
15	N	1	0.72	1.04
16	N	1	0.66	1.26
17	N	1	0.52	0.52
18	N	1	0.46	0.29
19	Y	1	0.31	0.27

rBF after reconstruction showed the same trend with 0.58 ± 0.40 in patients who developed necrosis and 0.82 ± 0.36 in patients who did not develop necrosis ((**Fig. 3.4(c)(d)**), while no statistical significance ($p = 0.35$) was observed. rBF values after reconstruction showed poor ability in prediction of skin flap necrosis, with an AUC of 0.68 (95% confidence interval = 0.17, 1) (**Fig. 3.4(d)**).

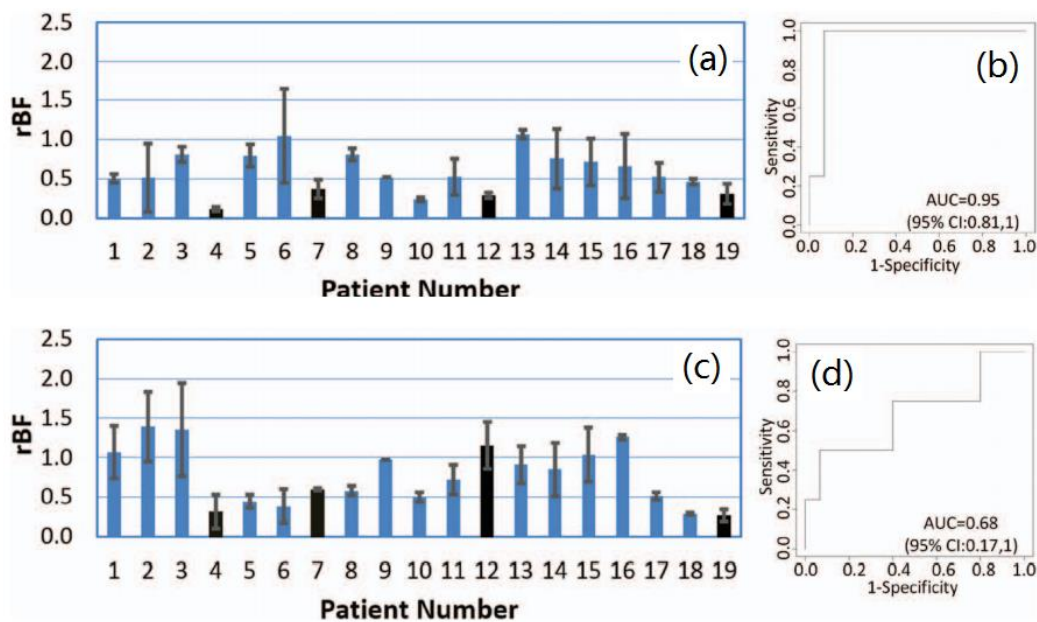


Figure 3.4 Prediction of mastectomy skin flap necrosis.

(a) Relative blood flow changes (rBF) immediately after mastectomy from 19 patients including 4 with mastectomy skin flaps necrosis (patient 4, 7, 12, and 19, marked with black bars). Error bars represent rBF variations (standard deviations) at different depths of the mastectomy skin flap. (b) AUC data immediately after mastectomy for discriminating mastectomy skin flaps with necrosis ($n = 4$) and without necrosis ($n = 15$). (c) rBF after reconstruction from 19 patients. (d) AUC data after reconstruction for discriminating mastectomy skin flaps with necrosis ($n = 4$) and without necrosis ($n = 15$).

3.3.2 3D imaging of chronic wounds

Five subjects with chronic wounds were recruited and measured. There was no PAD patient undergoing revascularization recruited in this study. Two of the five scanning were contaminated with significant motion artifacts since the patients moved significantly during noncontact scanning creating big difficulty for measurement alignment and were not processed for DCT reconstruction. The three successful cases included one with pressure ulcer, one with diabetic ulcer, and one with a non-healing traumatic injury.

The pressure ulcer (**Figure 3.5**) and diabetic ulcer (**Figure 3.6**) had a circular wound with similar size (~1 cm in diameter). The non-healing traumatic injury case (**Figure 3.7**) had a long and narrow wound (~8 cm long and ~1 cm width). The reconstructed BF distributions showed similar pattern in the three cases: higher BF contrast (higher and lower rBF levels comparing to background) was found close to the wound. BF variations are seen both on the surface and in deep tissue while larger BF contrasts mainly appeared on the tissue surface close to the wound margin. In addition, blood flow variations were relatively smaller in the surrounding tissues away from the wound. rBF contrasts (rBF relative to the normal surrounding tissues) over the reconstructed tissue volume were ranging from 0 to 4.0 in the pressure ulcer, from -0.2 to 3.0 in the diabetic ulcer, and from 0.0 to 3.8 in the non-healing traumatic injury, respectively.

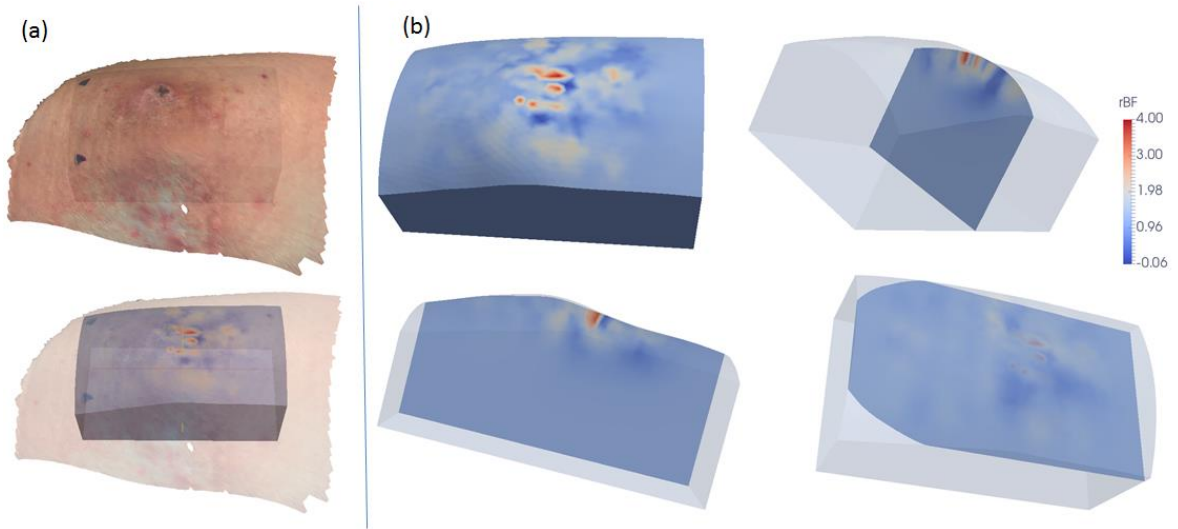


Figure 3.5 DCT results from the pressure ulcer case.

(a) Surface color image overlays with the surface BF distributions. (b) Surface and cross section views of relative blood flow changes (rBF) distributions.

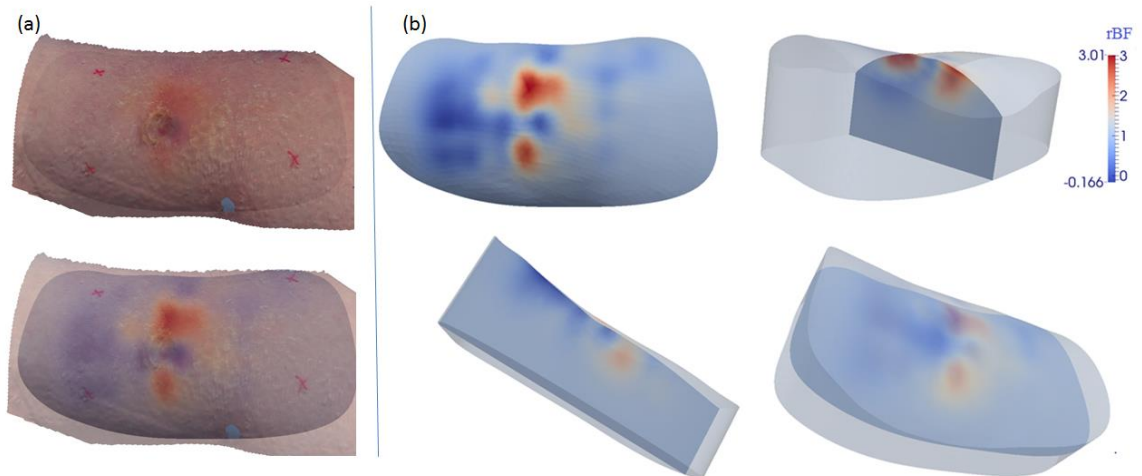


Figure 3.6 DCT results from the diabetic ulcer case.

(a) Surface color image overlays with the surface BF distributions. (b) Surface and cross section views of relative blood flow changes (rBF) distributions.

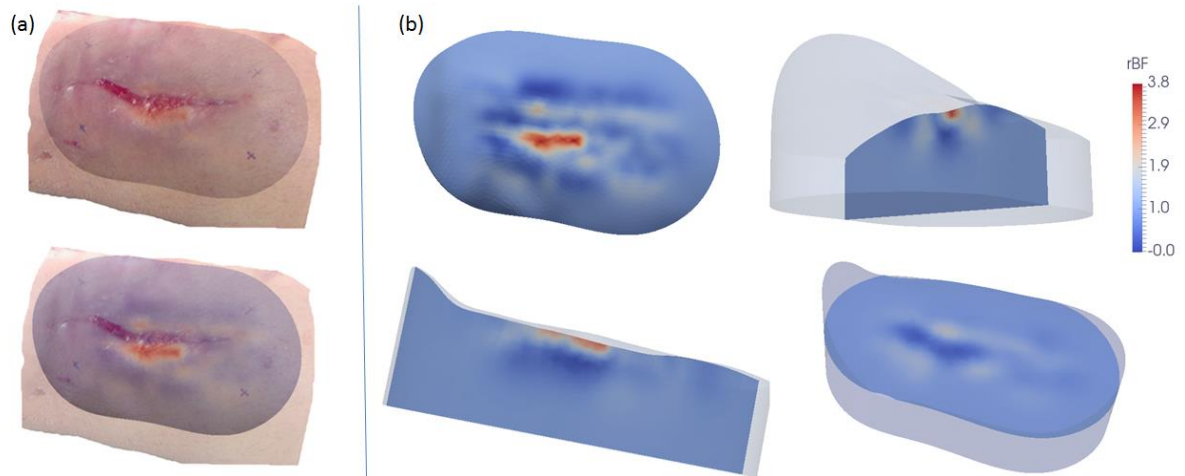


Figure 3.7 DCT measurement results from the non-healing traumatic injury case.

(a) Surface color image overlays with the surface BF distributions. (b) Surface and cross section views of relative blood flow changes (rBF) distributions.

3.4 Discussion and conclusions

Prediction of mastectomy skin flap necrosis. We have demonstrated the feasibility of ncDCS for intraoperative measurements of tissue blood flow in the operating room without interfering with the sterility of surgical setup. The ncDCS has negligible risk comparing to other imaging modalities for intraoperative measurement because of the lack of dye injection or direct contact with patient.

Patients who developed mastectomy skin flap necrosis had significantly lower rBF values at immediately after mastectomy (**Figure 3.4(a)**) comparing with patients who did not develop mastectomy skin flap necrosis, demonstrating the potential of ncDCS for the intraoperative prediction of necrosis risk [43]. Interestingly, the only patient (patient # 4) who required additional surgery had the lowest rBF immediately after mastectomy (**Figure 3.4(a)**), indicating a possible correlation between the

severity/extent of the mastectomy skin flap necrosis and the rBF value immediately after mastectomy. More subjects are needed to establish a model between risk level of necrosis and rBF values.

rBF values after reconstruction showed the same trend that lower values were obtained from patients who developed mastectomy skin flap necrosis (**Figure 3.4(c)**) without reaching statistical significance. Furthermore, rBF after reconstruction demonstrated poor discriminating ability of mastectomy skin flap necrosis (**Figure 3.4(d)**). rBF after reconstruction also showed larger variations comparing with those immediately after mastectomy (**Figure 3.4**), which may be partly attributed to the presence of the tissue expander or implant after reconstruction.

3D imaging of BF distributions in skin flaps can significantly increase spatial resolution and enable precise prediction of necrosis volume and location for excision. However, limited by the long mechanical scanning time and poor spatial resolution, ncDCT imaging could affect surgical workflow in the operating room.

Imaging of chronic wounds. We have successfully applied ncDCT technique for 3D imaging of chronic wounds. Our preliminary results showed that tissue heterogeneity can be captured by the 3D imaging in relatively deep tissues. Given the burden of long-term care for chronic wounds, this translational technology has the potential to facilitate better understanding of deep tissue wound development and healing process, and may lead to improvements in wound management and substantial cost savings in the future. For example, pressure ulcer originates from bone and develops upward to tissue surface. Hemodynamic changes in deep tissue occur before the ulcer is evident on tissue surface [4, 103]. Therefore, imaging of deep tissue hemodynamics in population with risk of

pressure ulcer may help on the prevention and early diagnosis of pressure ulcer. Previous study in PAD patients undergoing revascularization surgery showed that oxygenation level in the treated foot has significant increase after the surgery, indicating that hemodynamic measurement could be used to validate the success of the treatment [104]. Adequate perfusion and hemodynamic success are not only important judgment for the success of revascularization surgery, but are also mandatory for healing of chronic wound [100]. Thus, imaging of deep tissue hemodynamics should provide important information on the prediction of wound healing and on the validation of treatment outcome of various types of chronic wound.

For the chronic wound study, we experienced difficulty in subject recruitment. In order to participant in this study, subjects were asked to travel from WCC after their clinic visit to CCTS. Although free public transportation and free parking were available, it was still hard and inconvenient for the potential subjects since most of them had other chronic diseases or health issues besides the wound, which all together limited their mobility significantly. In addition, because of the limited coverage of the ncDCT system, only small wounds were imaged.

Limitations of ncDCS/ncDCT system. The ncDCS/ncDCT system has some limitations when applying in clinical settings. The motorized linear stage enables lateral scanning along the surface of ROI and allows relatively dense sampling by assigning relative short step separation. However, the fixed linear S-D array limits longitudinal coverage of scanning and leads to poor spatial resolution. Motion artifacts may contaminate boundary data and result in difficulty for S-D alignment. The step-by-step scanning in relatively low speed also makes ncDCT system impractical for catching fast

transient changes in tissue hemodynamics. Since ncDCS/ncDCT system uses optical fibers and expensive APDs, it is difficult to improve temporal and spatial resolution.

4.1 Introduction

Imaging of blood flow (BF) distributions in burn wounds can provide essential information for determining the ischemic area that requires wound excision or skin grafting to ensure successful surgical outcomes [1]. As reviewed early in **Chapter 3**, although noncontact diffuse correlation spectroscopy and tomography (ncDCS/ncDCT) can measure BF distributions in vulnerable tissues including wounds, they have limited temporal and spatial resolution and limited size of region of interests (ROI) for BF imaging because of limited sources/detectors and long mechanical scanning. Very recently, our lab proceeded from avalanche photodetector (APD) to camera detection for blood flow imaging, which significantly increases temporal/spatial resolution and eliminates the needs of mechanical scanning. This novel optical imaging technique is termed speckle contrast DCT (scDCT) [44-46]. The scDCT employs a focused point source and a galvo mirror to remotely project point light onto source locations over a selected ROI. The optical zoom lens in front of the camera enables fully noncontact detection of BF and flexible adjustment of ROI. As mechanical scanning is no longer needed, scDCT enables fast data acquisition, which is desirable for use in the operating room. Thousands of pixels provided by the camera significantly improve spatial resolution of imaging. The scDCT system has been tested for BF imaging using tissue-simulating phantoms and *in vivo* tissues.

The scDCT technique extracts boundary BF information from the spatial distribution of diffuse laser speckles detected by the camera. Boundary BF data is input to the modified NIRFAST program (see **Chapter 3.2.2**) for three dimensional (3D) tomographic reconstruction of BF distributions. In addition, we have developed two dimensional (2D) mapping method, which requires less computation time (several minutes) compared to 3D reconstruction (several hours) [105], although it sacrifices the depth information.

One limitation with the current scDCT technique is the potential influence of unknown tissue optical properties such as μ_a on BF measurements [25, 47, 106]. For the current approach of blood flow index (BFI, i.e. αD_B) quantification from diffuse speckle contrasts, we assume constant optical properties (absorption coefficient: μ_a , reduced scattering coefficient: μ'_s) for the entire tissue volume. However, it has been reported that different types of tissues or tissues with different diseases have varied optical properties [85, 107]. Assuming inaccurate optical properties may lead to error in αD_B calculations [108-110]. Therefore, new algorithms to overcome this limitation are desired [106, 109, 111].

In this study, I optimized and tested the scDCT system using tissue-simulating phantoms and in human forearms with arterial occlusions to validate the capability of the scDCT system on imaging spatial and temporal flow changes. I applied the scDCT system for the first time to image burned wounds [47]. Lower BF was expected in burnt tissue comparing with surrounding normal tissue. I also developed and validated a new algorithm for extracting both αD_B and μ_a from the measured light intensities and speckle

contrasts at multiple S-D distances collected by scDCT system in order to get rid of the influence of μ_a on αD_B calculation.

4.2 Methods

4.2.1 scDCT instrumentation

Figure 4.1 shows the scDCT system configuration [45]. Two cameras were tested including an electron-multiplying charge coupled device (EMCCD; Cascade 1K, Photometrics, AZ) and scientific complementary metal–oxide–semiconductor (sCMOS; Hamamatsu Orca Flash 4.0LT) in the scDCT system. Camera specifications are listed in **Table 4.1**. The sCMOS camera has higher frame rate (30 frame per second (fps)) comparing with the EMCCD (~10 fps), which benefits a faster sampling.

Table 4.1 Specifications of Cascade 1K and Orca Flash 4.0LT

	Cascade 1K	Orca Flash 4.0LT
Sensor type	EMCCD	sCMOS
Pixel number	1004 × 1002	2048 × 2048
Pixel size	8 μm × 8 μm	6.5 μm × 6.5 μm
Sensor size	8.032 mm × 8.016 mm	13.312 mm × 13.312 mm
Well capacity	30,000	30,000
Frame rate	10Hz	30Hz
AD conversion	16 bits	16 bits

The camera with a large number of pixels increases significantly sampling density and spatial resolution. It also eliminates the need of mechanical scanning in ncDCT, and

thus shortens the measurement time and avoids motion artifacts. NIR point-source light at 830 nm from a long-coherence laser (Crystalaser) is delivered through a multimode fiber (core size: 200 microns) to an achromatic lens (AC127-019-B, Thorlabs), and then to a galvo mirror (GVS002, Thorlabs). The galvo mirror projects NIR light to different source positions in ROI. Very recently, a pinhole was added into the source light path between the achromatic lens and the galvo mirror to sharpen the projected laser spot on the measured tissue/phantom.

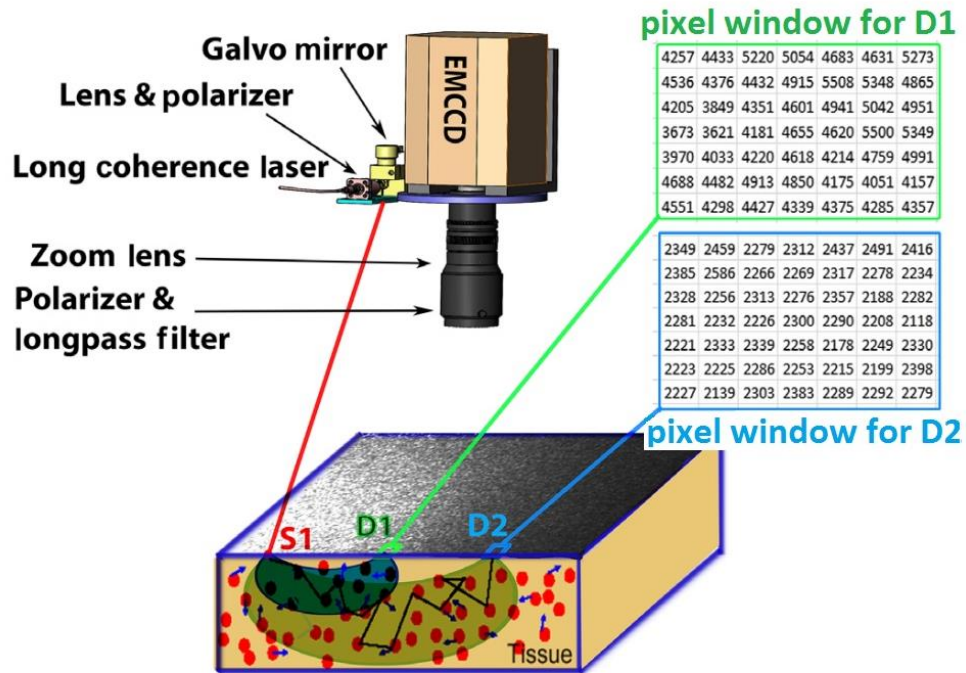


Figure 4.1 scDCT system configuration.

The EMCCD/sCOMS camera is focused by a zoom lens onto the tissue surface. A long coherence laser is connected through an optical fiber to lens and polarizer. The focused source light spot is projected by the galvo mirror onto the measured tissue surface. S1: source 1, D1/D2: detector 1/2.

A zoom lens (Zoom 7000, Navitar) is mounted to the camera enabling easy adjustment of ROI. The camera detects diffuse light from tissue surface in a reflectance mode, which is more practical and flexible for applications in large volume tissues, where transmission mode is impractical due to limited penetration depths of light. In order to reduce the direct reflection of the source light from the tissue surface, a pair of polarizers (LPNIRE050-B and LPNIRE200-B, Thorlabs) is added in source light path and in camera detection path. A long-pass filter (84-762, Edmund Optics, NJ) is added in front of the zoom lens to minimize the influence of room light. The noncontact scDCT probe is fixed on an articulated arm for flexible positioning and accurate focusing on the ROI. The scDCT system is controlled by a LabView program for accurate projection of source light to desired locations and the sequential collection of images.

4.2.2 3D reconstruction of blood flow distributions

The concept of speckle contrast comes from laser speckle contrast imaging, where typically a wide-field illumination is applied over a ROI and a camera is used for detecting laser speckle fluctuation on superficial tissue surface [112, 113]. By contrast in scDCT technique, a focused point laser source is used to deliver NIR light into the deep tissue. An EMCCD/sCOMS camera is used to detect diffused laser speckle fluctuation, resulting from motion of red blood cells. The diffuse speckle contrast is defined as:

$$K_s(\mathbf{r}) = \frac{\sigma_s}{\langle I \rangle}, \quad (4.1)$$

Here, σ_s is the spatial or temporal standard deviation of light intensity and $\langle I \rangle$ is the mean intensity of a set of pixels, \mathbf{r} is the distance of the pixels from the source location.

From the Siegert relationship (**Equation 2.5**), the speckle contrast $K_s(\mathbf{r})$ can be related to the temporal correlation function g_1 as the following [44]:

$$K_s(\mathbf{r})^2 = \frac{2\beta}{T} \int_0^T \left(1 - \frac{\tau}{T}\right) [g_1(\mathbf{r}, \tau)]^2 d\tau; \quad (4.2)$$

Where T is the exposure time.

By substituting g_1 with its analytical solution (**Equation 2.9**) to **Equation 2.7** in semi-infinite geometry, a nonlinear relationship between $K_s(\mathbf{r})$ and αD_B can be established, where $K_s(\mathbf{r})$ can be written as a function of αD_B , together with other parameters [44]:

$$K_s(\mathbf{r})^2 = f(\alpha D_B, T, \mu_a, \mu_s', \lambda, \beta, k_0, \mathbf{r}) \quad (4.3)$$

Where λ is the wavelength of the source light and k_0 is the wavenumber. For each fixed set of αD_B , μ_a , μ_s' , λ , β and k_0 , the nonlinear relationship between the diffuse speckle contrast (K), S-D separation (\mathbf{r}) and exposure times (T) is shown in **Figure 4.2**.

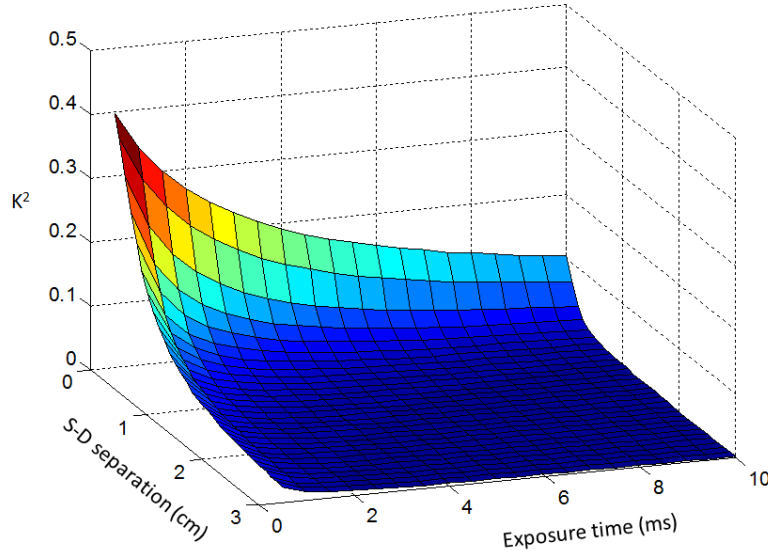


Figure 4.2 Variations in speckle contrasts over a range of S-D separations and exposure times.

We extract αD_B from the speckle contrast at a single S-D separation and a single exposure time (i.e., a single data point on the surface shown in **Figure 4.2**) [44, 45]. The speckle contrast can be experimentally measured and calculated (**Equation 4.1**) from images taken by the camera. In the right-hand side of **Equation 4.3**, T , λ , k_0 and r are known or measurable, μ_a , μ_s' and β can be estimated from literatures. Therefore, αD_B is the only unknown variable. By assigning a value for αD_B , a theoretical diffuse speckle contrast can be calculated using **Equation 4.3**. Finally, αD_B is determined by searching for the value of αD_B that minimizes the square difference between the measured speckle contrast and the theoretical speckle contrast.

The αD_B extracted from scDCT is equivalent to that obtained from APDs measurement in ncDCT as introduced in **Chapter 3**. Therefore, scDCT reconstruction of 3D blood flow distributions can be performed in the same manner as ncDCT [44, 45].

4.2.3 2D mapping of blood flow distributions

2D mapping of BF distributions projects boundary BF measurements onto a 2D mesh of FOV, which saves computation time comparing with DCT reconstruction. The procedures of 2D mapping are introduced below [105]. For each linked S-D pair, BFI is first calculated using the method introduced in **Chapter 4.2.2**. The midpoint was then calculated for the S-D pair as the center location between the source and the detector (**Figure 4.3**). The boundary BFI is then projected to the midpoint location to represent the S-D pair. This is because the midpoint matches better to the realistic sensitive region of the diffuse light with a banana photon pathway for the manipulated S-D pair.

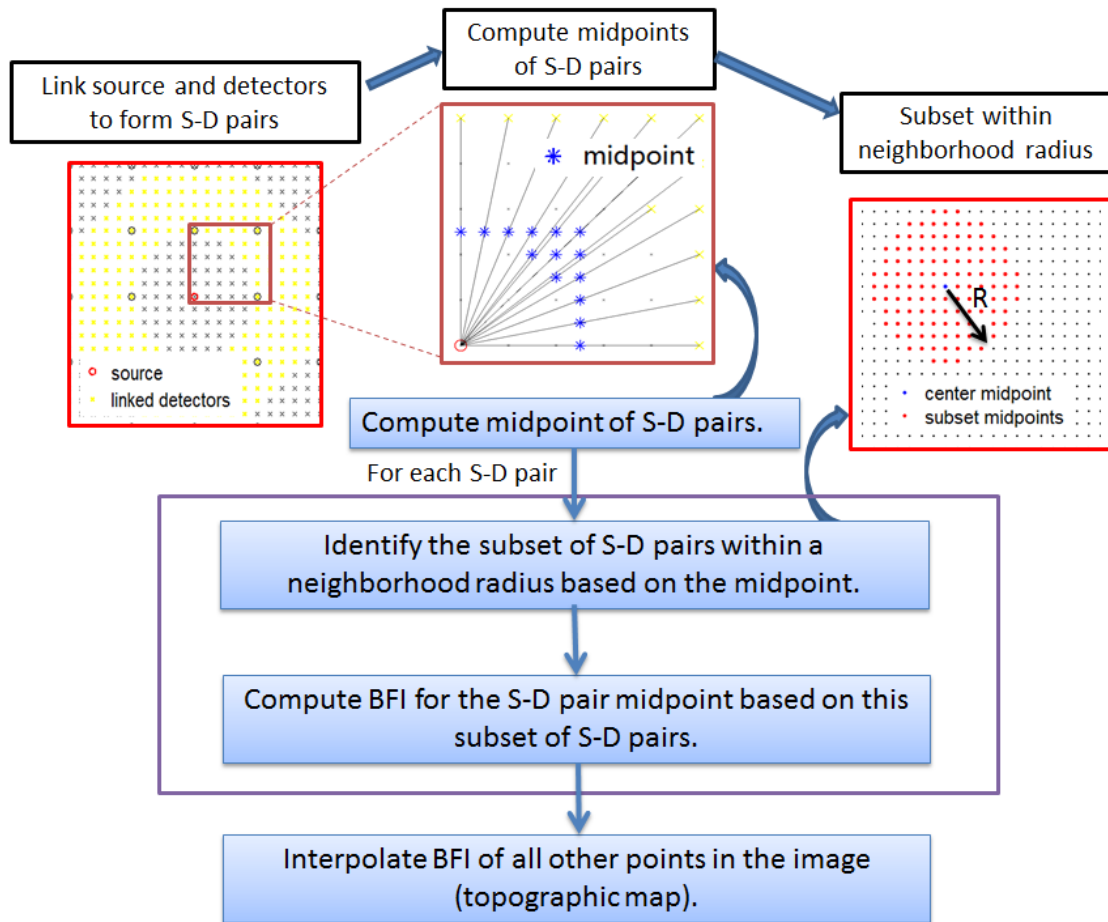


Figure 4.3 Flowchart of 2D mapping algorithm.

S-D: source-detector.

After BFI and midpoints over all linked S-D pairs are calculated, spatial merging and smoothing are done. For each midpoint, a subset of S-D pairs within a neighborhood radius based on midpoint location is identified. The average or weighted average of the BF measurements corresponding to this subset are calculated and projected to the manipulated midpoint location as the final BF value for this location.

4.2.4 Phantom tests

Tissue-like phantoms with known optical properties are commonly used in optical instrument calibration and validation. The liquid phantom consists of distilled water, India ink (Black India, MA) and intralipid (Fresenius Kabi, Sweden). The intralipid particles in the liquid phantom provide control of μ'_s and Brownian motion (particle flow) while India ink provides control of μ_a .

In this study, the optical properties of the homogeneous phantom were set as $\mu_a = 0.05 \text{ cm}^{-1}$ and $\mu'_s = 8 \text{ cm}^{-1}$ to match the realistic biological tissues. The homogeneous liquid phantom was filled into a water tank as the background. Two heterogeneous phantoms were created to validate the scDCT system by embedding two different anomalies with increased or decreased flow contrast respectively into the homogeneous phantom.

In the first heterogeneous phantom, a transparent plastic cylindrical tube (diameter = 6 mm, length = 80 mm) connected with a peristaltic pump (HV-77201-60, Cole Parmer, IL) through soft rubber tube was placed 5 mm (tube center to liquid phantom surface) beneath the surface of the background liquid phantom to create high flow contrasts at different levels against the background liquid phantom. The tube lay across the center of ROI along x direction (**Figure 4.4 (a)**). The tube was mostly stuffed with small pieces of solid phantom (composition: titanium dioxide, silicon and carbon black) with the same optical properties as the background liquid phantom to randomize the particle motion as random flow inside the tube. The tube was then filled with the same liquid phantom and the liquid was pumped by the pump to create step increases in steady flow from 0 to 20 ml/min at 5 ml/min increment in the tube.

In the second heterogeneous phantom, two sphere shape solid phantoms ($\mu_a = 0.05 \text{ cm}^{-1}$, $\mu'_s = 8 \text{ cm}^{-1}$, flow = 0) at diameter of $\sim 7 \text{ mm}$ were placed at 5 mm (sphere center to background phantom surface) beneath the surface of background liquid phantom at the locations of X-Y planes (15, 15 mm) and (-15, -15 mm) respectively to create low flow contrasts against the background liquid phantom (**Figure 4.4 (a)**). A thin iron wire penetrating through the centers of the two sphere solid phantoms was used to hold the two anomalies in place.

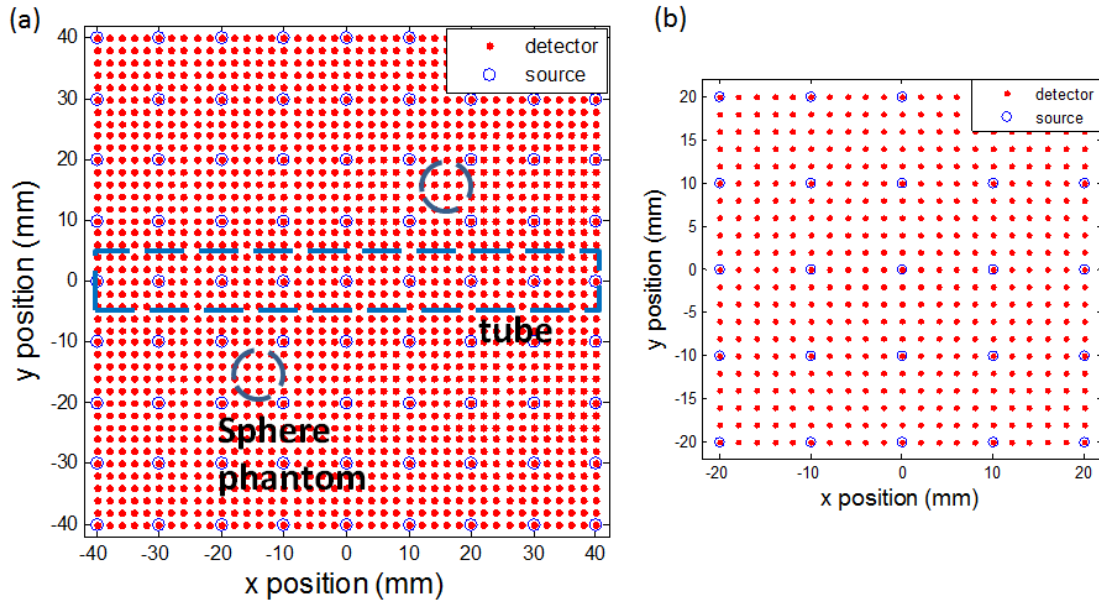


Figure 4.4 Phantom tests with scDCT.

(a) Source-detector (S-D) configuration for phantom tests: region of interests (ROI) = $80 \times 80 \text{ mm}^2$; dimension and locations of anomalies. (b) S-D configuration for forearm occlusion test: ROI = $40 \times 40 \text{ mm}^2$

For scDCT data collection, the EMCCD (i.e., Cascade 1K in **Table 4.1**) was used.

An ROI of size $80 \times 80 \text{ mm}^2$ was selected to cover the anomalies region (**Figure 4.4 (a)**).

The galvo mirror projected 830 nm source light to 9×9 source locations (1 cm separation from each) in the ROI. For each scanning, 4 frames of EMCCD images were

taken at each source location. 41×41 detectors (2 mm separation from each) were evenly defined in the ROI for image reconstruction. Sources and detectors within S-D separation range of 7 to 19 mm werelinked for boundary data calculation and DCT reconstruction. Image reconstructions were processed using a $100 \times 100 \times 30 \text{ mm}^3$ slab mesh centered at (0, 0, 15 mm) with 4 mm distance nodes and refined 1.3 mm distance nodes in the center (~60K nodes in total) to improve the reconstruction resolution in the targeted area.

4.2.5 Imaging of forearm blood flow

The scDCT is tested for continuous imaging of BF changes in a healthy human forearm. The BF change in forearm was induced by a 4-minute arterial occlusion at a pressure of 230 mmHg applied on the upper arm. The EMCCD (i.e., Cascade 1K in **Table 4.1**) was used in this test. An ROI of $40 \times 40 \text{ mm}^2$ was selected on the subject's forearm (**Figure 4.4 (b)**). 5×5 sources separated by 1cm of each were used for the data collection. 21×21 detectors were evenly defined for boundary BF calculation. Image reconstruction was processed on a $60 \times 60 \times 30 \text{ mm}^3$ slab mesh centered at (0, 0, 15 mm) with 2 mm distance nodes (~20K nodes in total).

4.2.6 Imaging of wounds

The experimental protocol has been approved by University of Kentucky (UK) Institutional Review Board (IRB) (#14-0571-F1V) [47]. Patients with burn wound were recruited from UK hospital. scDCT imaging was done in the operating room prior to wound excision and grafting (**Figure 4.5 (a)**). The EMCCD (i.e., Cascade 1K in **Table**

4.1) was used in this study. A ROI of $80 \times 80 \text{ mm}^2$ was selected to cover an area with burned tissue and adjacent unburnt tissues. 9×9 sources were evenly distributed over the ROI with 1 cm separation between each for data acquisition (**Figure 4.5 (b)**). The exposure time used in this study was 5 ms. Two frames of raw images were acquired and averaged at each source location.

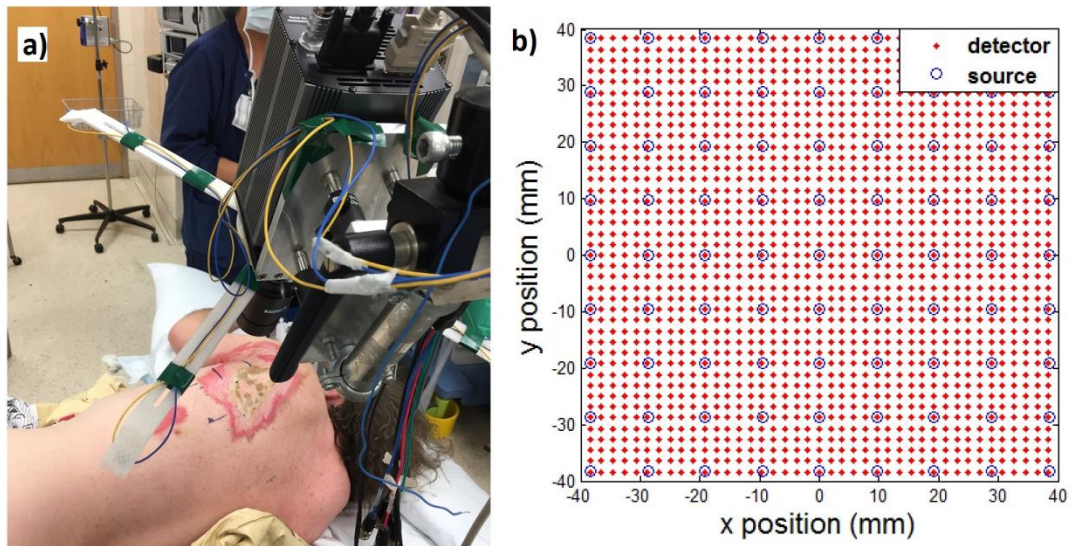


Figure 4.5 Imaging of BF distributions in burn wounds with scDCT system.

(a) Experimental set up in the operating room. scDCT imaging is focused onto the selected area across the burned wound and surrounding normal tissue. (b) The source-detector arrangement over the region of interests.

41×41 detectors with 2 mm separation between each were evenly defined over the ROI (**Figure 4.5 (b)**). Each detector region was defined as binding 3×3 adjacent pixel windows while each pixel window consisted of 7×7 pixels. Spatial speckle contrast was first calculated for each of the 9 pixel windows. Speckle contrast of the detector was then calculated by averaging the speckle contrasts over the 9 pixel windows

and over the two frames to enhance signal-to-noise ratio [44, 45]. S-D separation was calculated as the distance from the center of the source light spot to the center of each detector region. Pre-processing of raw data including shot noise removal, dark noise removal and smear correction were performed prior to speckle contrast calculations. Speckle contrasts at the S-D separations of 7 to 19 mm were then calculated as boundary data [44, 45].

Boundary BFI data were normalized to their mean value (assigning “1”) to calculate relative change of BF (rBF). The normalized boundary rBF were then used as input for 3D tomographic reconstructions of BF distributions in the targeted tissue volume using the modified NIRFAST and for 2D mapping of BF distributions. For the 3D reconstruction, a slab shape tetrahedral mesh with a volume of $100 \times 100 \times 30 \text{ mm}^3$ and node distance of 2 mm was used for 3D image reconstruction. In this study, we only recruited patients with burn on body part(s) with relatively flat surface. Thus, a slab mesh was used to approximate tissue geometry without introducing much errors related to irregular geometry. A neighborhood radius of 6 mm was used for 2D mapping. Results from 3D reconstruction and 2D mapping were compared.

4.2.7 Simultaneous extraction of absorption coefficient (μ_a) and blood flow index (αD_B)

Recalling **Equation 4.3**, speckle contrast is a function of multiple parameters including αD_B and optical properties (μ_a and μ_s). The assumption of optical properties may lead to errors in αD_B calculations. Therefore, developed a new algorithm that enables extraction of both μ_a and αD_B from the measured light intensities and speckle

contrasts at multiple S-D distances. This algorithm employs a two-step approach: first, μ_a is calculated from the measured light intensities at multiple S-D distances; second, αD_B is calculated from the speckle contrast at multiple S-D distances with the input of μ_a obtained in the first step. Details of these steps are described below.

The simplified solution of photon diffusion equation is given as [23, 105, 111]:

$$\ln[I(r) r^2] = k - r \mu_{eff} \quad (4.4)$$

Here $I(r)$ is the light intensity I at S-D separation r , k is a constant, μ_{eff} is the effective attenuation coefficient defined as:

$$\mu_{eff}(\lambda) = \sqrt{3 \mu_a(\lambda) \cdot \mu'_s(\lambda)} \quad (4.5)$$

Note that the premise of **Equation 4.4** is $r \geq 1$ cm [23, 105]. $\ln[I(r) r^2]$ approximately has a linear relationship with r when this condition is met. μ_{eff} can be fitted from light intensities at multiple S-D distances since μ_{eff} is the slope in this linear model. By assuming μ'_s , μ_a can be calculated by fitting μ_{eff} (**Figure 4.6 (a)**).

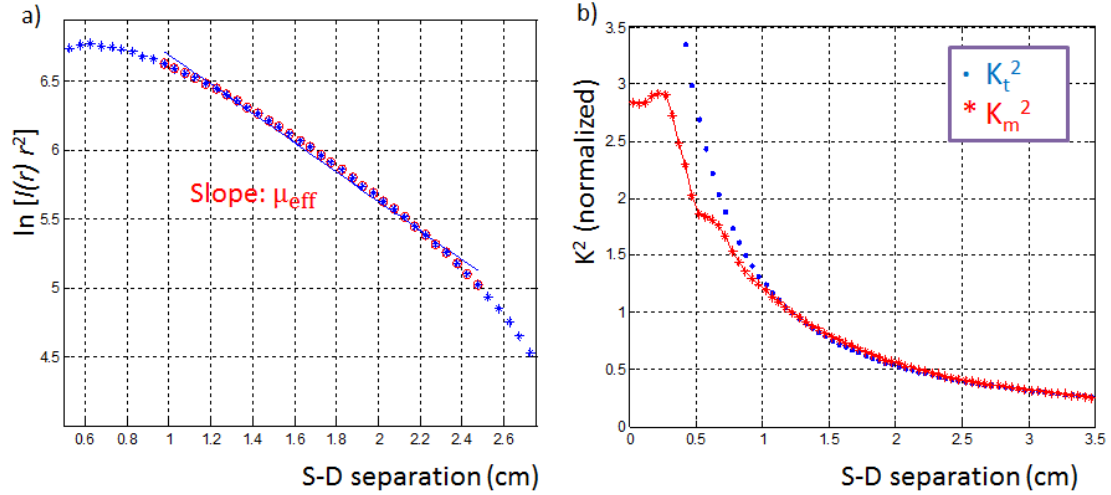


Figure 4.6 Two-step approach for extraction of μ_a and μ_s' .

(a) Fitting effective attenuation coefficient (μ_{eff}) from light intensities measured at multiple source-detector (S-D) separations. (b) Fitting blood flow index (αD_B) from speckle contrasts measured at multiple S-D separations.

The second step of the algorithm is to fit αD_B from the measured speckle contrasts at multiple S-D distances by minimizing the penalty term defined as [106, 109, 110, 114]:

$$\chi^2 = \sum_{i=1}^{N_r} [K_m^2(r_i, \alpha D_B) - K_t^2(r_i, \alpha D_B)]^2 \quad (4.6)$$

Here, K_m^2 is the experimentally measured speckle contrast and K_t^2 is the theoretical speckle contrast with assigned αD_B calculated using **Equation 4.3**. In order to eliminate the influence of the linear scaling factor β in **Equation 4.3**, we normalize both K_m^2 and K_t^2 to their mean over all the selected r respectively to cancel β from the calculation (**Figure 4.6 (b)**) [110].

In addition to the improvement on quantification of αD_B , assessment of μ_a at multiple wavelengths (λ) would enable the quantification of [Hb] and [HbO₂] (see **Chapter 2.2.1**).

4.2.8 Phantom tests for simultaneous extraction of μ_a and αD_B

The high sensitivity sCMOS camera (i.e., Orca Flash4.0LT in **Table 4.1**), which has better sensitivity in photon sensing, was used in this test.

The pinhole added in the source light path was further optimized for this test to minimize the influence of the projected laser spot to the diffuse speckle at relatively short S-D separations, which is critical for the tested algorithm since speckle contrast at short S-D separations are more sensitive to the change of αD_B . There is a trade-off for the opening of pinhole: the smaller the laser spot is the better signal at short S-D separations; however, more light is blocked by the pinhole so the signal to noise ratio (SNR) decreases especially at larger S-D separations. In this study, we optimized the pinhole opening to get valid data at S-D separations around 3 mm up to around 20 mm. **Figure 4.7** shows a comparison of normalized speckle contrast at multiple S-D separations without (**Figure 4.7 (a)**) and with (**Figure 4.7 (b)**) the optimized pinhole in the source path.

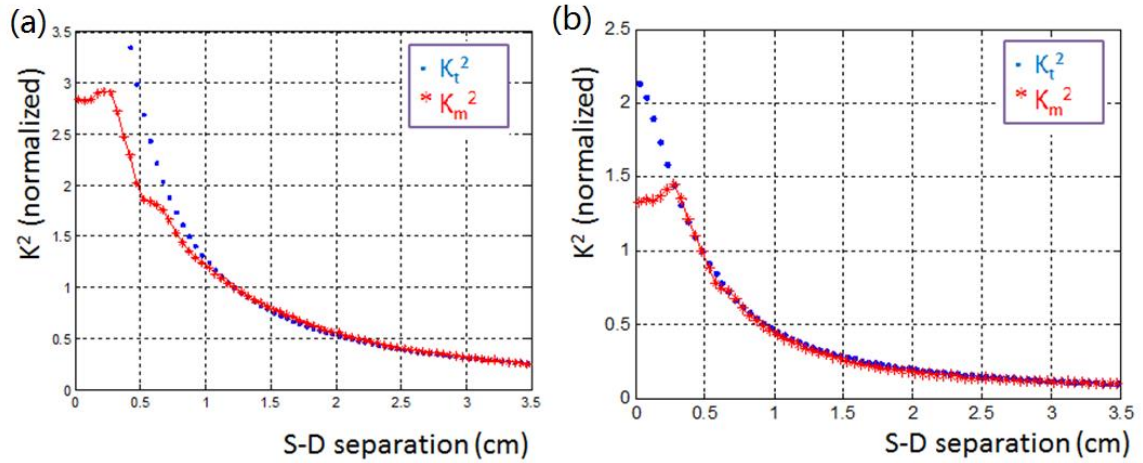


Figure 4.7 Effect of pinhole optimization.

(a) Before pinhole optimization: the shortest valid source-detector (S-D) separation was around 10mm. (b) After pinhole optimization: the shortest valid S-D separation was shorten to around 3mm.

The new algorithm requires input of measured light intensities and speckle contrasts at multiple S-D separations. At this preliminary stage, our tests were done with one source located at the center of the FOV (**Figure 4.8 (a)**). We then optimized the parameters of the camera and the lens system based on this configuration.

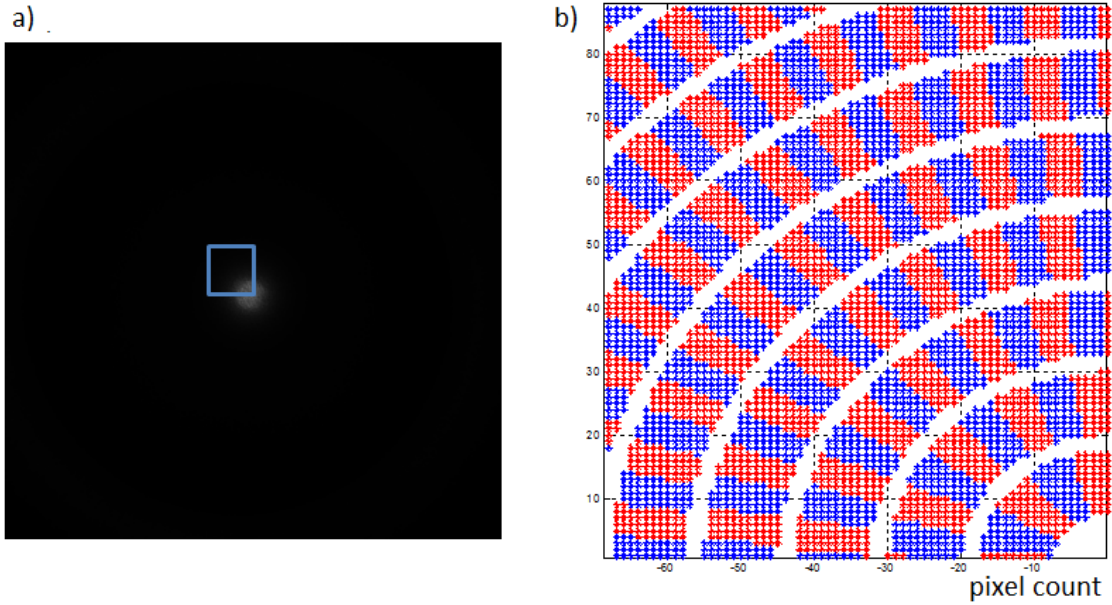


Figure 4.8 Definition of pixel windows.

(a) Experimental set up for phantom test of the new algorithm. The source location is fixed at the center of field of view. (b) Pixel window definition in the blue box region marked in (a): each cluster of pixels with same color is assigned as one pixel window.

A field of view (FOV) of $90 \times 90 \text{ mm}^2$ was selected to ensure up to 30 mm S-D separations in all directions. To fulfill the Nyquist sampling criteria that the minimum speckle size (ρ_{speckle}) must be two times larger than the camera pixel size (ρ_{pixel}), the following equation gives the lower limit of F# [115]:

$$\rho_{\text{speckle}} = 2.44\lambda (1+M) F\# \geq 2\rho_{\text{pixel}} \quad (4.8)$$

Here, M is the magnification of the imaging system, which is camera sensor size (i.e., $13.312 \times 13.312 \text{ mm}^2$) divided by the size of FOV ($90 \times 90 \text{ mm}^2$). The calculation results suggest that the minimum F# for the current setting is 6.4.

Several combinations of exposure time ($T = 1, 2, 3, 5 \text{ ms}$) and F# (6.4, 8, 11) were tested on tissue like phantoms with varied μ_a levels (0.04 cm^{-1} to 0.16 cm^{-1}). The

combination of $T = 2\text{ms}$ and $F\# = 8$ gives the best data quality and this is used in the following tests.

Experimental design for phantom tests. To examine the performance of the new algorithm, we performed tissue-like liquid phantom tests using the above-mentioned configuration and parameters ($\text{FOV} = 90 \times 90 \text{ mm}$, $T = 2 \text{ ms}$, $F\# = 8$). A glass tank was filled with the liquid phantom that consisted of distilled water, India ink (Black India, MA) and Intralipid (Fresenius Kabi, Sweden).

As the new algorithm aimed to extract μ_a and αD_B from scDCT data, we varied μ_a and αD_B of the phantom respectively, while μ'_s was set at 10 cm^{-1} throughout the test. At each step, 50 frames of images were taken using the scDCT system. For validation, near infrared spectroscopy (NIRS) and diffuse correlation spectroscopy (DCS) measurements were also conducted on the tissue phantoms using a hybrid contact probe.

Indian ink titration was done to create gradient in μ_a from 0.04 cm^{-1} to 0.16 cm^{-1} with 0.03 cm^{-1} increment per step, while concentration of intralipid was kept constant with $\mu'_s = 10 \text{ cm}^{-1}$ and $\alpha D_B = \sim 1 \times 10^{-8} \text{ cm}^2/\text{s}$. For each titration step, the phantom was stirred thoroughly and then rested for 2 minutes to allow it to come back to static before data collection by scDCT and NIRS/DCS.

Changes in Brownian motion (αD_B) were created by changing the temperature of the phantom from $5 \text{ }^\circ\text{C}$ to $25 \text{ }^\circ\text{C}$ (fridge to room temperature). The μ_a and μ'_s were controlled at 0.1 cm^{-1} and 10 cm^{-1} respectively during the flow titration. Data was collected at each increment of $5 \text{ }^\circ\text{C}$ using scDCT and NIRS/DCS devices. The temperature was monitored by a thermometer throughout the test and recorded when optical data were collected.

For each raw image, dark noise and shot noise were removed before speckle contrast calculation. Note that, sCMOS camera (i.e., Orca Flash 4.0LT in **Table 4.1**) used in this study does not have smear effect as the EMCCD (i.e., Cascade 1K in **Table 4.1**) had. Spatial speckle contrasts and light intensities in all directions around the source were calculated in S-D separations ranged from 0.25 to 35 mm, with increment of 0.5 mm. For each S-D separation r_0 , all pixels within $(r_0 - 0.2) \text{ mm} \leq r \leq (r_0 + 0.2) \text{ mm}$ were selected and segmented into pixels windows of 50 adjacent pixels (**Figure 4.8 (b)**). Speckle contrasts of each pixel window were calculated using **Equation 4.1** and then averaged over all the pixel windows to get the speckle contrast at r_0 . Similarly, light intensities at each S-D separation were calculated and averaged using the same pixel window assignment for each image. Finally, speckle contrasts and light intensities at multiple S-D separations were averaged over 50 frames of images for each S-D separation.

Light intensities at S-D separations of 10 to 20 mm were used to fit μ_a . Speckle contrasts at S-D separations of 3 to 15 mm were used to fit αD_B . For the validating measurements using NIRS/DCS, μ_a and μ'_s were first calculated from NIRS data at each step. αD_B was then calculated from DCS data with μ_a and μ'_s measured by NIRS as inputs.

The μ_a and αD_B fitted from the new algorithm were compared with NIRS/DCS measurement results. Percent error in the fitted data with the new algorithm was calculated by taking NIRS/DCS data as gold standard (i.e., $\text{error} = 100\% \times \frac{|\text{fitted} - \text{standard}|}{\text{standard}}$). Linear regression of μ_a in ink titration was conducted between the

NIRS data and scDCT data with the new algorithm. Linear regression of αD_B was also conducted between DCS and scDCT measurements.

4.3 Results

4.3.1 Phantom test results

Figure 4.9 (a) shows the cross-section view of the reconstructed flow distribution at pump speed of 20 ml/min cross the tube anomaly center. The tube shape was clearly reconstructed. Reconstructed anomaly was determined by a half-maximum threshold and the reconstructed anomaly flow at each pump speed was calculated as the mean αD_B in the reconstructed anomaly region.

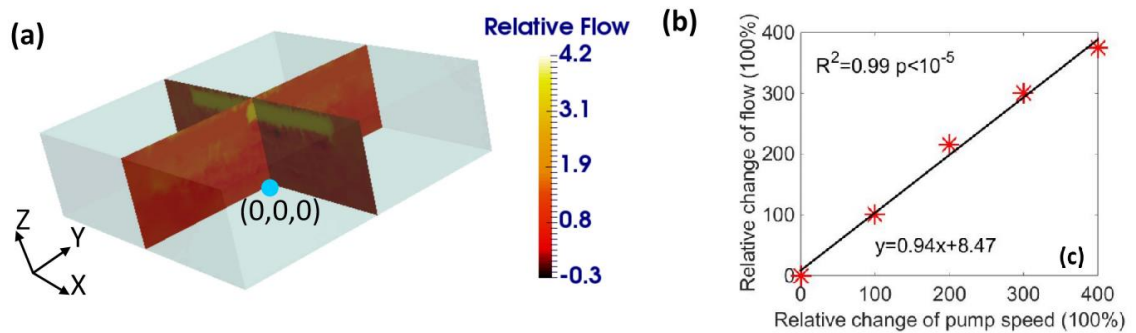


Figure 4.9 The reconstructed 3D images of tube flow contrasts.

(a) Cross section views of x direction at pump speed of 20 ml/min. (b) Linear regression between the reconstructed percentage flow changes and relative flow changes by the pump.

For comparison, the reconstructed anomaly flow contrasts were normalized to the averaged step difference of αD_B . The pump speeds were normalized to the step

difference (i.e., 5 ml/min). **Figure 4.9 (b)** shows the linear regression between the reconstructed percentage flow changes and the relative flow changes pumped in the tube. Perfect linear relationship was observed ($y = 0.94x + 8.47$, $R^2 = 0.99$, and $p < 10^{-5}$).

Figure 4.10 (a) illustrates the cross-section views of the reconstructed flow contrast of the two anomalies in the liquid phantom. **Figure 4.10 (b)** shows the cross-section views of X-Y plane at different depths (0, 3, 6 and 9 mm) below the phantom surface. Similarly, the reconstructed anomalies were determined by a half-maximum threshold. The averaged flow contrasts in the two reconstructed anomalies are 0.32 and 0.25 (relative to a background flow assigning 1). The reconstructed center locations of the two anomalies are (14.2, 15.4, 24.5 mm) and (-14.4, -15.3, 25.8 mm), which are close to the designed locations (15.0, 15.0, 25.0 mm) and (-15.0, -15.0, 25.0 mm), respectively. The reconstructed anomaly diameters are 8.6 and 7.1 mm, which are close to the diameter of the solid sphere phantoms (~ 7 mm).

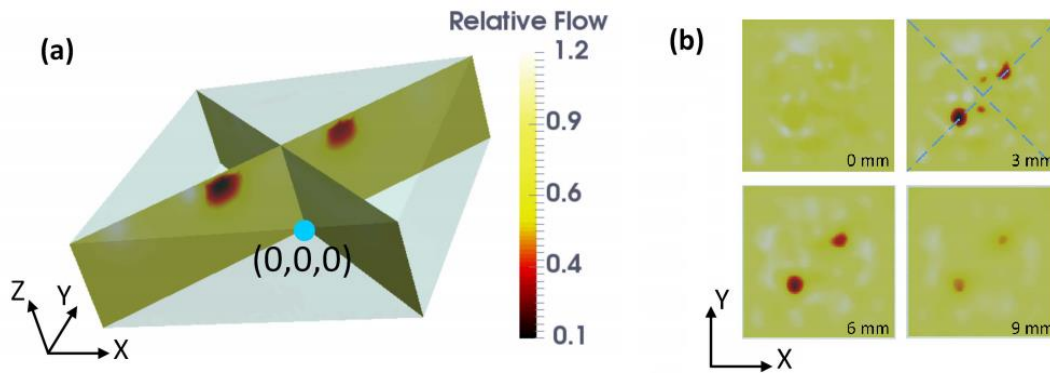


Figure 4.10 Reconstructed images of spherical phantoms flow contrasts.

(a) Cross section views cross the center of the two spherical anomalies. (b) Cross section views of X-Y plane at the depths of 0, 3, 6 and 9 mm below the phantom surface.

4.3.2 Human forearm test results

Figure 4.11 shows the reconstructed 3D forearm BF images during baseline (T1) (**Figure 4.11 (a)**), cuff occlusion (T2) (**Figure 4.11 (b)**), reactive hyperemic peak flow (T3) (**Figure 4.11 (c)**), and recovery (T4) (**Figure 4.11 (d)**). **Figure 4.11 (e)** shows time sequence of BF changes relative to resting baseline in the selected two tissue volumes (marked on **Figure 4.11 (a)**) of $\sim 5 \text{ mm}^3$ centered at (0, 0, 25 mm) and (16, 16, 25 mm), respectively. The spatial averaged rBF values inside the two tissue volumes at the four measurement time points (T1 to T4) shown in **Figure 4.11 (e)**. The rBF trends throughout the occlusion protocol are consistent in the two selected tissue volumes with some spatial heterogeneity. The rBF trends and variation level agreed well with previous results. These results demonstrate the feasibility of scDCT for 3D in vivo imaging of BF distributions in deep tissue.

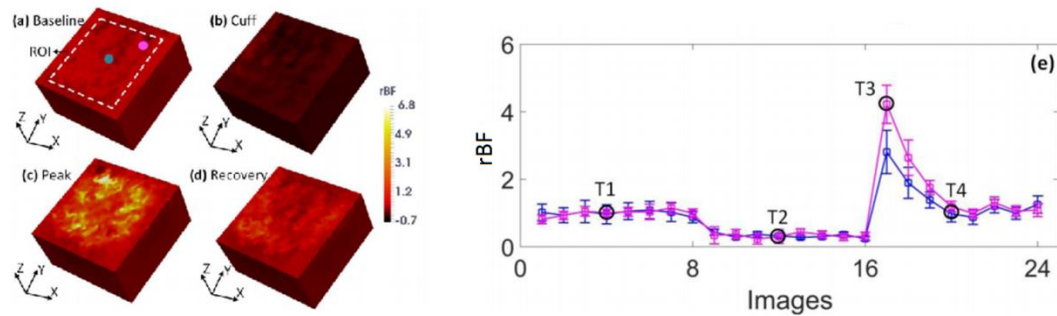


Figure 4.11 Reconstructed 3D images of forearm blood flow during cuff occlusion.

Forearm flow images at the periods of baseline (a), cuff occlusion (b), reactive hyperemic peak flow (c), and recovery (d). (e) Time sequence of flow changes in the selected two tissue volumes marked in (a).

4.3.3 3D and 2D imaging of wounds

Two patients with full thickness burn wounds were enrolled in this study [47]. **Figure 4.12** shows imaging results from Patient #1. **Figure 4.12 (a)** shows the surface color photo of the selected ROI that covers the areas of full thickness burn, partial thickness burn, and surrounding unburnt tissue. The boundaries across the burn and unburnt tissues are marked with blue lines. **Figure 4.12(b)** shows the reconstructed 2D cross-section views of rBF distributions in the targeted tissue at different depths of 0, 3, 6, and 9 mm below the tissue surface. Each cross-section was averaged from mesh nodes located within $\pm 0.2\text{mm}$ range from the center depth. The average rBF values in the full thickness burn volume, the partial thickness burn volume, and the normal tissue volume were 0.97 ± 0.054 , 1.01 ± 0.053 , and 1.04 ± 0.062 (mean \pm standard deviation), respectively (**Figure 4.12**). One-way ANOVA test revealed significant differences in rBF among different tissue volumes ($p < 0.001$). Post-hoc tests in ANOVA suggested significant differences in rBF for each of pair-wise comparison across different tissue volumes ($p < 0.001$). In addition, spatial variations in rBF existed across the ROI and over different depths. **Figure 4.12 (c)** shows the 2D mapping of BF distributions which agreed with the DCT reconstruction results.

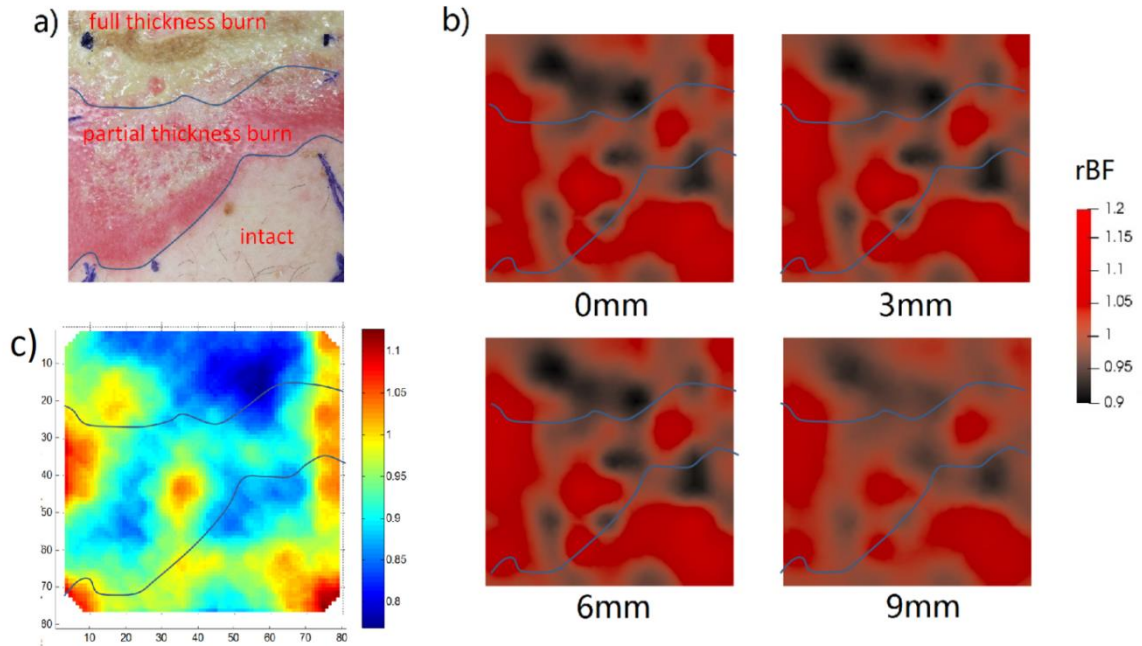


Figure 4.12 BF Distribution in Patient #1.

(a) A photo of the imaged region. (b) 2D cross-section views of relative blood flow (rBF) distributions at the depths of 0, 3, 6, and 9 mm. (c) 2D mapping of rBF.

Figure 4.13 shows the imaging results from Patient #2. Similarly, significant lower rBF values (0.92 ± 0.078) were observed in the eschar volume (**Figure 4.13**), compared to the surrounding tissue volume (1.06 ± 0.079 , $p < 0.001$, two sample t-test). Spatial variations in rBF existed across the ROI and over different depths. Note that the wound in Patient #2 was a burn combined with pressure ulcer, diagnosed during wound excision. In addition, the range of rBF variation in Patient #2 (0.8 to 1.4) was larger than that in Patient #1 (0.9 to 1.2). **Figure 4.13 (c)** shows the 2D mapping of BF distribution; similar flow pattern was seen as observed in 3D image.

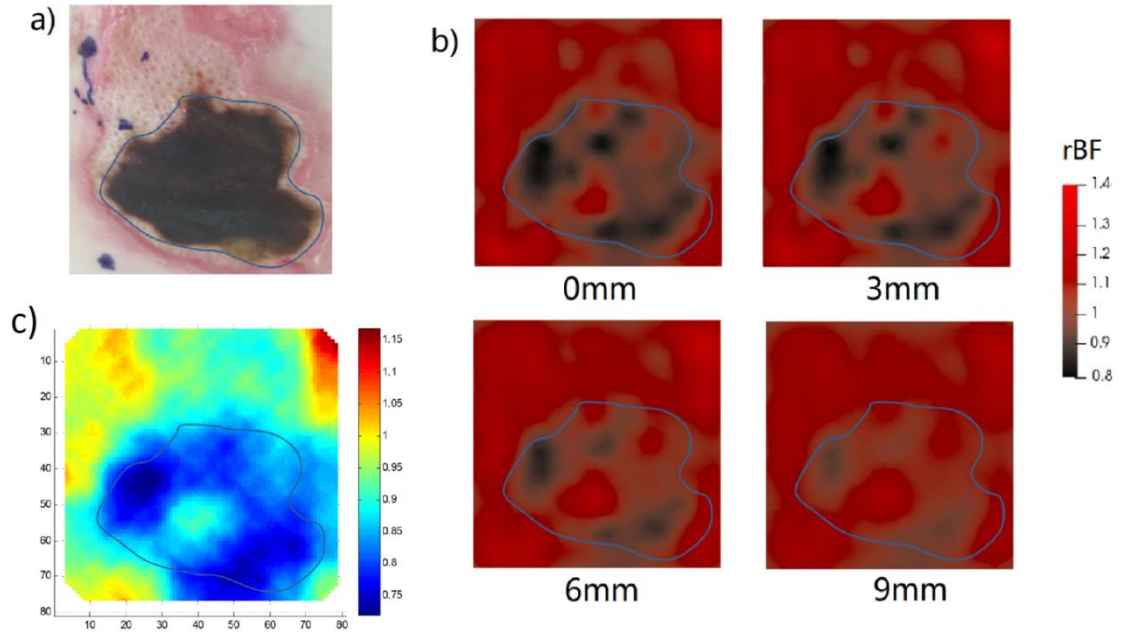


Figure 4.13 BF Distribution in Patient #2.

(a) A photo of burn/wound region. (b) 2D cross-section views of relative blood flow (rBF) distributions at the depths of 0, 3, 6, and 9 mm. (c) 2D mapping of rBF.

4.3.4 Phantom test results for simultaneous extraction of μ_a and αD_B

Results of ink titration and temperature variation are shown in **Figure 4.14** and **Figure 4.15**. Comparison of μ_a and αD_B values obtained from the scDCT with the new algorithm and from NIRS/DCS are reported in **Table 4.2**. Linear regressions between these measurements are shown in **Figure 4.16**.

Table 4.2 Summary of phantom test results

	μ_a (cm^{-1})		Error (%)	αD_B ($*10^{-8} \text{ cm}^2/\text{s}$)		Error (%)
	reference	fitted		reference	fitted	
Ink titration test	0.040	0.033	15.97	1.08	1.02	5.31
	0.073	0.068	6.21	1.22	1.19	3.05
	0.100	0.097	3.30	1.28	1.35	5.80
	0.127	0.130	2.29	1.10	1.24	13.23
	0.155	0.157	1.13	1.11	1.62	45.42
Temperature varying test	0.099	0.099	0.49	0.77	0.68	11.51
	0.099	0.099	0.20	0.80	0.79	1.72
	0.099	0.098	0.81	0.90	0.88	2.19
	0.099	0.100	0.91	1.00	1.01	0.67
	0.099	0.100	1.02	1.17	1.09	7.29

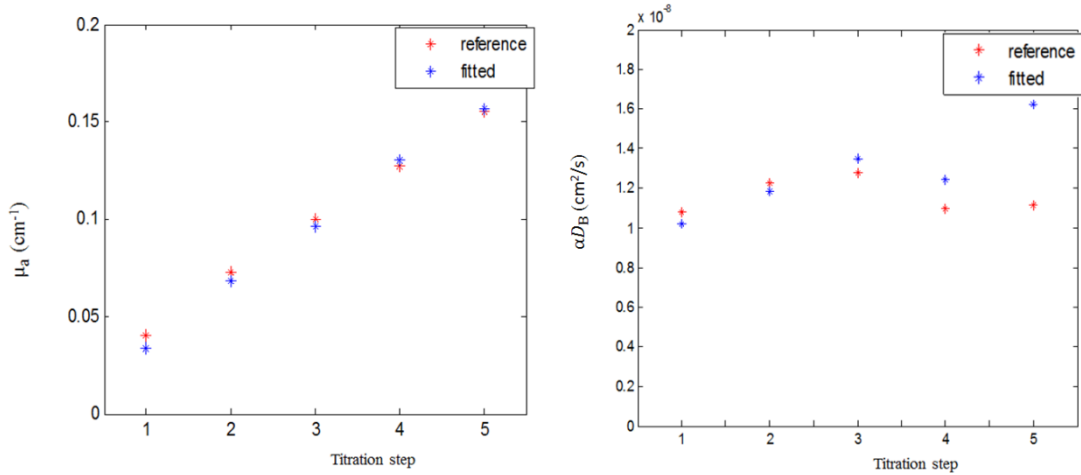


Figure 4.14 Ink titration results.

(a) Comparison results between the fitted absorption coefficient (μ_a) and NIRS measured μ_a . (b) Comparison results between the fitted blood flow index (αD_B) and DCS measured αD_B .

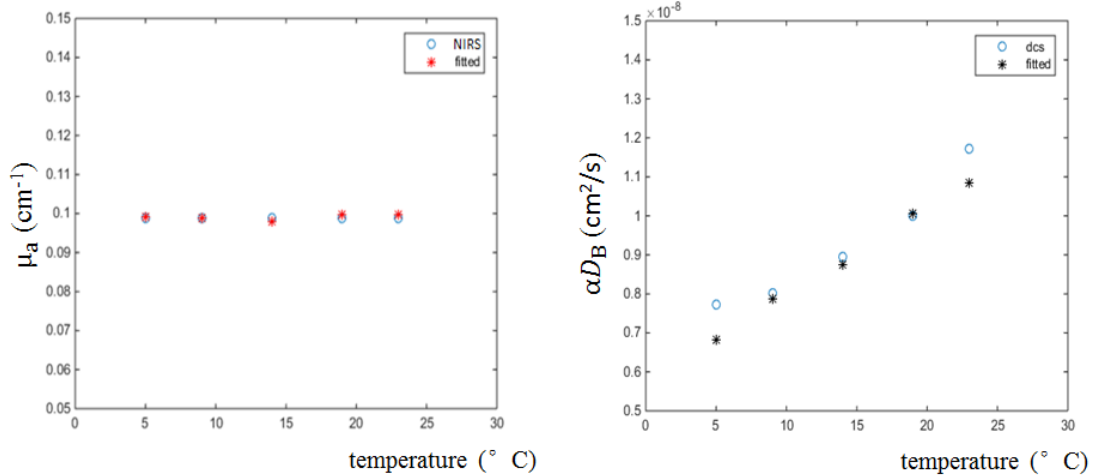


Figure 4.15 Temperature variation results.

(a) Comparison results between the fitted absorption coefficient (μ_a) and NIRS measured μ_a . (b) Comparison results between the fitted αD_B and DCS measured αD_B .

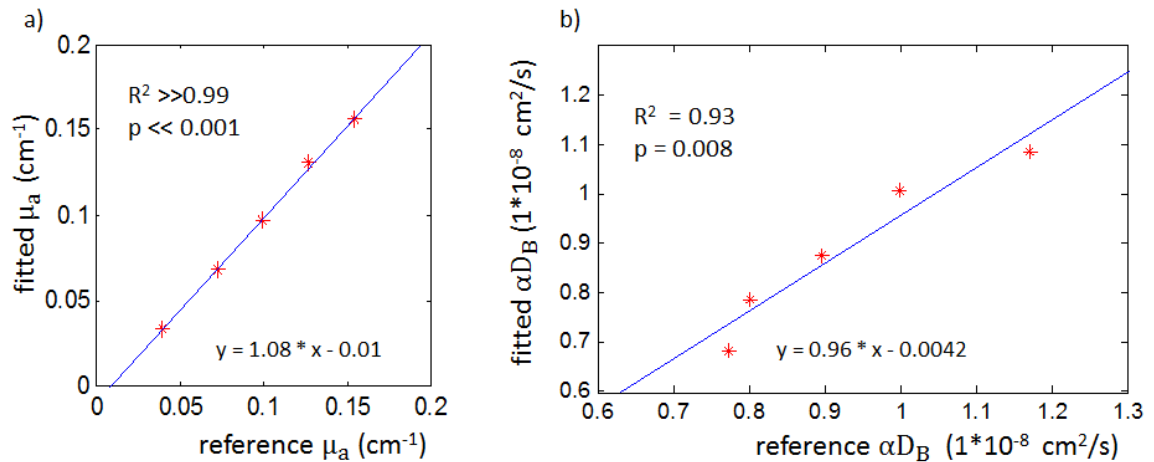


Figure 4.16 Linear regressions of fitted unknowns against pre-set values.

(a) Linear regression between the fitted μ_a and NIRS measured μ_a from ink titration tests. (b) Linear regression between the fitted blood flow index (αD_B) and DCS measured αD_B from temperature variation tests.

4.4 Discussion and conclusions

We have developed an innovative scDCT system for BF imaging. Use of EMCCD/sCMOS camera as a 2D detection array significantly increases spatial resolution and speeds up data acquisition. Comparing to ncDCT that uses APDs as detector, the motion artifacts and lengthy scan time from mechanical scanning are mitigated with the novel design of scDCT. The optical zoom lens used in scDCT enabled adjustment of ROI with different sizes, thus offering translatability of the scDCT for small animals and large human subjects. The use of galvo mirror enabled flexible projection of source location to anywhere within FOV and made the source/detector pattern and scanning density adjustable for different applications.

We have tested the scDCT system using tissue-simulating phantoms with two types of heterogeneities (high and low flow contrasts relative to the background). In both cases, flow contrast and anomaly geometries were successfully reconstructed. The recovered flow contrast changes in the cylindrical tube was highly correlated to the pump speed changes ($R^2 = 0.99$, and $p < 10^{-5}$) (**Figure 4.9**) demonstrating that we accurately captured the flow contrast/changes using scDCT. The recovered flow contrast of the solid sphere phantoms were 0.25 and 0.32 to the background (~ 1.00) (**Figure 4.10**), which are comparable to our previous results found by similar phantoms [39, 44]. Their localization matched the actual arrangement in the phantom setup. Results from *in vivo* imaging on human forearm indicated the capability of scDCT on monitoring deep tissue blood flow distributions of both temporal and spatial variations. The hyperemic response after cuff occlusion was clearly visible at multiple locations in the forearm tissue (**Figure 4.11**). The random spatial variation was expected due to regional tissue heterogeneities.

The pilot study on imaging of burn wounds demonstrates the feasibility of scDCT system for noncontact 3D imaging of blood flow distributions in vulnerable tissues with no risk of infection. As expected, significant lower BF values were observed in the burn/wound volumes compared with the surrounding unburn tissue volumes in both patients. Spatial heterogeneities in rBF were also observed across different tissue volumes (e.g., partial thickness burn versus full thickness burn) and over different depths. We noted that the rBF variation in Patient #2 (0.8 to 1.4) was larger than that in Patient #1 (0.9 to 1.2), generating a better rBF image contrast (**Figure 4.13(b)**). Thus, the rBF distribution from Patient #2 (**Figure 4.13(b)**) matched the pattern of the wound/eschar (**Figure 4.13(a)**) better than Patient #1 (**Figure 4.12**). The relatively smaller rBF variation/contrast across different tissue areas/volumes in Patient #1 made it more difficult to be detected. Also, it was possible that the “intact” tissue adjacent to the wound was affected by adjacent burn. Thus, it was not surprised that lower rBF areas/volumes were observed in the "intact" tissue adjacent to the "partial thickness burn" tissue (**Figure 4.12**). Due to the limited number of subjects in this study ($n = 2$), however, it is impossible to test the significance of inter-patient difference in rBF variations. More subjects are needed to test whether there is a minimum/maximum rBF variation that limits to clinical utility of the results.

In addition to 3D reconstruction, 2D mapping of BF distributions has been established for burned wounds. Similar patterns in BF contrasts were obtained comparing with 3D reconstruction. Comparing to 3D reconstructions which are time consuming (several hours), the 2D mapping (~3 min) is time efficient. The scDCT provides the depth resolution with the expense of computation time, whereas 2D mapping provides

real-time monitoring ability. Comparing to LSCI, 2D mapping with scDCT allows mapping of BF at different depths by selecting different S-D separations; larger S-D separations are, more weight from deeper layers. In summary, selection of 2D mapping and 3D reconstruction should be made upon specific applications.

From the results of imaging burn wounds, although the trends of BF decreases in burn/wound areas agreed with surgeon's prediction, the amplitudes of rBF decreases were smaller than expected. This may be attributed to the influence of μ_a and μ_s' on αD_B calculations, as discussed in **Chapter 4.1** and **Chapter 4.2.7** [25, 47, 106]. Therefore, we developed the new algorithm for extracting both μ_a and αD_B .

The new algorithm extracts μ_a and αD_B from the scDCT measurements without additional instrumentation or measurements. The assessment of μ_a improves the accuracy of αD_B calculation from speckle contrast at multiple S-D separations. In previous studies, αD_B was calculated with assumed μ_a or μ_a measured by other technique [44, 45, 110]. In this study, we eliminated the need of additional measurement. Moreover, knowledge of μ_a at multiple wavelengths provides the potential for tissue oxygenation measurements in the future.

We have validated the new algorithm using tissue-like liquid phantoms with varied μ_a and αD_B . Results measured by the new algorithm agreed well with those measured by DCS and NIRS over a wide range of μ_a and αD_B which are commonly observed in biological tissues, indicating the potential of the algorithm for calculating both μ_a and αD_B in a variety types of biological tissue. Promising results have been obtained especially in μ_a using light intensities at multiple S-D separations. Relatively

larger errors were found in αD_B fitting when μ_a was large and SNR was low, indicating the sensitiveness of the new algorithm to SNRs.

The next step is to apply this new algorithm for *in vivo* applications. One of the foreseen challenges is the tissue heterogeneity. Instead of using boundary data over the full FOV, we may select a subset data at a local/regional area for data fitting to reduce the influence of tissue heterogeneity. Other work to optimize the algorithm for *in vivo* applications include data screening, noise removal, and trade-off between data quality and time efficiency.

5.1 Study Summary and my contributions

In this dissertation, I presented the progression of advancing NIR diffuse optical techniques for spectroscopic measurements and tomographic imaging of tissue hemodynamics in vulnerable tissues with the goal of disease diagnosis and treatment monitoring. For the studies reported in **Chapter 2**, I participated in the adaptation and optimization of hybrid near infrared spectroscopy and diffuse correlation spectroscopy (NIRS/DCS) with a contact fiber-optic probe for simultaneous and continuous monitoring of absolute values of BF, blood oxygenation, and oxygen consumption in exercising gastrocnemius [28]. This is the first time that the hybrid NIRS/DCS techniques together with the novel occlusive calibration and gated dynamometer exercise protocol have been translated to lower limb measurement. My contributions include adaptation of the occlusive calibrations for absolute quantification of blood flow (BF) and oxygen consumption (VO_2) in calf muscles, optimization of dynamometer gating exercise protocols and NIRS/DCS settings, validation tests in young healthy subjects, and characterization of muscle hemodynamic responses to exercise in older adults with vitamin D (vitD) insufficiency [38]. I conducted all optical measurements using a hybrid NIRS/DCS device in older population and analyzed all optical data. I also built an Arduino-based control system for real-time monitoring and recording of dynamometer foot pedal position and torque reading. I developed a MATLAB program with graphical user interface (GUI) for automatic torque peak recognition. Results from these

measurements indicated that vitD supplement plus aerobic training improved muscle metabolic function in older population [38].

For the studies reported in **Chapter 3**, I adapted and optimized an innovative noncontact diffuse correlation spectroscopy and tomography (ncDCS/ncDCT) system for three dimensional (3D) imaging of mastectomy skin flaps and chronic wounds [39, 42, 43, 101]. The ncDCS/ncDCT system employed optical lenses to project sources and detectors remotely onto the tissue surface which is appropriate for vulnerable tissue assessment comparing with contact apparatus as the noncontact measurement minimized the risk of inflammation. A motorized linear stage was employed to drive the noncontact probe to scan over a region of interests (ROI) for 3D tomographic imaging of blood flow distributions. The ncDCS/ncDCT system was applied in clinical applications, including intraoperative assessment of blood flow in mastectomy skin flaps [43] and *in vivo* imaging of chronic wounds. For intraoperative assessment of mastectomy skin flaps, I contributed to experimental design, data collection, and result interpretation. We found that intraoperative relative BF changes (rBF) immediately after mastectomy correlated with flap viability over months after the surgery, indicating the potential of ncDCS measurements for predicting skin flap necrosis. For imaging of chronic wounds, I independently established measurement protocol, performed optical measurements and data processing. Spatial variations in BF contrasts over the wounded tissues were observed, indicating the capability of ncDCT in detecting tissue hemodynamic heterogeneities. The ncDCT holds the potential for longitudinal monitoring and validation of chronic wound healing.

For the studies reported in **Chapter 4**, I adapted and optimized a novel camera-based noncontact speckle contrast DCT (scDCT) for 2D/3D imaging of burn wounds [44, 45]. The scDCT employed a focused point source and a galvo mirror to remotely project point light onto source locations over a selected ROI. A camera with a flexible ROI and fast sampling rate was used for imaging of BF distributions. The camera provided 2D detector matrix thus eliminated the need for mechanical scanning and enabled fast data acquisition. Thousands of pixels provided by the camera significantly improve spatial resolution of imaging. I was involved in building and validating the scDCT system using tissue-simulating phantoms and in human forearms with a cuff occlusion protocol [45]. I upgraded the scDCT with a new scientific complementary metal-oxide-semiconductor (sCMOS) camera and optimized scDCT configuration to improve data quality. Finally, I adapted the scDCT for 3D imaging of burn wounds. I independently performed optical measurements and data processing, and wrote the manuscript [47]. Significantly lower BF values were observed in the burn areas compared to surrounding normal tissues. Due to the limited subject number, further interpretation of the measurement and its clinical utility are subject to future work. In addition to 3D reconstruction, I also explored fast 2D mapping of BF distributions towards real-time visualization. To overcome the influence of μ_a on BF quantification, I developed and validated a new algorithm to extract both μ_a and αD_B using light intensities and speckle contrasts measured by scDCT at multiple source-detector distances [105, 106, 109-111]. The new algorithm enabled μ_a quantification and potential oxygenation assessment without adding additional measurement and improved the accuracy of αD_B quantification using scDCT. I also designed and conducted phantom

validation tests for the new algorithm. *In vivo* application of the new algorithm is subject to future work.

5.2 Study limitations and future perspectives

Sample size and measurement validation. The sample sizes in the studies of imaging chronic wounds ($n = 5$) and burn wounds ($n = 2$) were small. In the future, more patients will be recruited, and results will be compared to other established techniques to verify the capability of noncontact scDCT for imaging of vulnerable tissues. We may also recruit and measure more patients with interventions; e.g., peripheral arterial disease (PAD) patients with ulcers under revascularization and cancer patients undergoing tissue flap reconstruction. We expect to correlate our measurement results with clinical outcomes for evaluation and prediction of intervention outcomes.

Accuracy of BF quantification. Current data analyses for scDCT measurements (i.e., wound imaging) assumed constant μ_a from the literature [47]. This assumption may result in under- or over-estimation of rBF [25, 106]. Therefore, the new algorithm for extracting both μ_a and αD_B from scDCT measurements has been developed in this dissertation work [106, 109, 111]. Future study will translate and optimize this innovative algorithm for *in vivo* applications to improve accuracy of BF quantification. Current scDCT system enables 3D imaging of BF distributions using one single wavelength. In the future, we may extend to a multi-wavelength system for simultaneous measurements of BF and oxygenation distributions for comprehensive assessment of tissue viability.

Time efficiency of image reconstruction. Depending on mesh density and boundary configurations, current algorithms for finite element method (FEM) based 3D image reconstruction requires several hours for computation, which is a big obstacle for intraoperative real-time monitoring. Recently, a fast and efficient sensitivity map generation method in NIRFAST for diffuse optical tomography (DOT) reconstruction has been developed [116]. This method employs a reduced sensitivity matrix and takes advantage of parallelization processes, thus reducing the computation burden and shortening the process time significantly. We may adapt this method to the modified NIRFAST for DCT reconstruction in the future to realize real-time imaging.

Tissue geometry issue. For the patients with wounds imaged by our scDCT [47], DCT reconstructions were run with the assumption of a flat tissue surface geometry. Our previous studies showed that irregular tissue surface geometry can influence DCT reconstructions [46]. Very recently, we integrated a novel photometric stereo technique into the scDCT system to acquire both tissue surface geometry and boundary BFI data using the same camera [46]. We will adapt this method in future to improve the quality of image reconstructions.

APPENDIX: GLOSSARY

Notations/terms	Descriptions
[Hb]	deoxy-hemoglobin concentration
[HbO ₂]	oxy-hemoglobin concentration
μ_a	absorption coefficient
μ_s'	reduced scattering coefficient
2D	two dimensional
3D	three dimensional
α_{DB}	blood flow index (BFI)
APD	avalanche photodiode
ASL-MRI	arterial-spin-labeled magnetic resonance imaging
AT	aerobic training
AUC	area under the ROC curve
BF	blood flow
CTL	control
CW	continuous-wave
D	vitD repletion alone
DAT	vitD repletion + aerobic training
DCS	diffuse correlation spectroscopy
DCT	diffuse correlation tomography
DOT	diffuse optical tomography
EMCCD	electron-multiplying charge coupled device
FD	frequency domain (FD)
FEM	finite element method (FEM)
FOV	field of view (FOV)
fps	frame per second (fps)
GUI	graphical user interface (GUI)
H ₂ O	water
Hb	deoxy-hemoglobin
HbO ₂	oxy-hemoglobin
I	light intensity
IRB	Institutional Review Board (IRB)
λ	wavelength
k_0	wavenumber
K	speckle contrast
LCD	liquid crystal display (LCD)
LDF	laser Doppler flowmetry (LDF)
MRI	magnetic resonance imaging (MRI)
MVC	maximal voluntary isometric contractions (MVC)
ncDCS	noncontact diffuse correlation spectroscopy

ncDCT	noncontact diffuse correlation tomography
NIR	near-infrared light (NIR)
NIRS	Near-infrared spectroscopy (NIRS)
PAD	peripheral arterial disease
PET	Positron emission tomography
P-MRS	phosphorus magnetic resonance spectroscopy
rBF	Relative changes in blood flow
ROC	receiver operating characteristic
ROI	region of interest
rVO ₂	relative change in oxygen consumption
scDCT	speckle contrast DCT
sCMOS	scientific complementary metal–oxide–semiconductor
SD	secure digital
S-D	source-detector
SEM	standard error of mean
SNR	signal-to-noise ratio
StO ₂	blood oxygenation saturation
τ	correlation delay time
T	Exposure time
T50	recovery half-time
THC	total hemoglobin concentration
UK	University of Kentucky
vitD	Vitamin D
VO ₂	oxygen consumption rate
WCC	Wound Care Clinic
Δ StO ₂	change of blood oxygenation saturation

REFERENCES

1. A. D. Jaskille et al., "Critical review of burn depth assessment techniques: part II. Review of laser doppler technology," *J Burn Care Res* **31**(1), 151-157 (2010).
2. M. Augustin, and K. Maier, "Psychosomatic aspects of chronic wounds," *Dermatology and Psychosomatics/Dermatologie und Psychosomatik* **4**(1), 5-13 (2003).
3. K. Moreo, "Understanding and overcoming the challenges of effective case management for patients with chronic wounds," *Case Manager* **16**(2), 62-63, 67 (2005).
4. C. A. Salzberg et al., "A new pressure ulcer risk assessment scale for individuals with spinal cord injury," *Am J Phys Med Rehabil* **75**(2), 96-104 (1996).
5. N. Bergstrom et al., "The Braden Scale for Predicting Pressure Sore Risk," *Nurs Res* **36**(4), 205-210 (1987).
6. H. R. Moyer, and A. Losken, "Predicting mastectomy skin flap necrosis with indocyanine green angiography: the gray area defined," *Plast Reconstr Surg* **129**(5), 1043-1048 (2012).
7. Q. Luu, and D. G. Farwell, "Advances in free flap monitoring: have we gone too far?," *Curr Opin Otolaryngol Head Neck Surg* **17**(4), 267-269 (2009).
8. D. D. Adler et al., "Doppler ultrasound color flow imaging in the study of breast cancer: preliminary findings," *Ultrasound Med Biol* **16**(6), 553-559 (1990).
9. I. V. Larina et al., "Hemodynamic measurements from individual blood cells in early mammalian embryos with Doppler swept source OCT," *Opt Lett* **34**(7), 986-988 (2009).
10. S. Hu, and L. V. Wang, "Photoacoustic imaging and characterization of the microvasculature," *Journal of biomedical optics* **15**(1), 011101 (2010).
11. H. M. Subhash et al., "Volumetric in vivo imaging of microvascular perfusion within the intact cochlea in mice using ultra-high sensitive optical microangiography," *IEEE Trans Med Imaging* **30**(2), 224-230 (2011).
12. T. Yamada et al., "Clinical reliability and utility of skin perfusion pressure measurement in ischemic limbs--comparison with other noninvasive diagnostic methods," *J Vasc Surg* **47**(2), 318-323 (2008).
13. B. T. Phillips et al., "Intraoperative perfusion techniques can accurately predict mastectomy skin flap necrosis in breast reconstruction: results of a prospective trial," *Plast Reconstr Surg* **129**(5), 778e-788e (2012).
14. R. Singer et al., "Fluorescein test for prediction of flap viability during breast reconstructions," *Plast Reconstr Surg* **61**(3), 371-375 (1978).
15. R. Benya, J. Quintana, and B. Brundage, "Adverse reactions to indocyanine green: a case report and a review of the literature," *Cathet Cardiovasc Diagn* **17**(4), 231-233 (1989).
16. A. Nouvong et al., "Evaluation of diabetic foot ulcer healing with hyperspectral imaging of oxyhemoglobin and deoxyhemoglobin," *Diabetes Care* **32**(11), 2056-2061 (2009).

17. R. D. Braun et al., "Comparison of tumor and normal tissue oxygen tension measurements using OxyLite or microelectrodes in rodents," *Am J Physiol Heart Circ Physiol* **280**(6), H2533-2544 (2001).
18. C. R. Wyss et al., "Transcutaneous oxygen tension measurements on limbs of diabetic and nondiabetic patients with peripheral vascular disease," *Surgery* **95**(3), 339-346 (1984).
19. O. U. Scremin et al., "Pre-amputation evaluation of lower-limb skeletal muscle perfusion with H(2) (15)O positron emission tomography," *Am J Phys Med Rehabil* **89**(6), 473-486 (2010).
20. M. P. Francescato, and V. Cettolo, "Two-pedal ergometer for in vivo MRS studies of human calf muscles," *Magn Reson Med* **46**(5), 1000-1005 (2001).
21. V. Ntziachristos et al., "Concurrent MRI and diffuse optical tomography of breast after indocyanine green enhancement," *Proc Natl Acad Sci U S A* **97**(6), 2767-2772 (2000).
22. J. P. Culver et al., "Diffuse optical tomography of cerebral blood flow, oxygenation, and metabolism in rat during focal ischemia," *J Cereb Blood Flow Metab* **23**(8), 911-924 (2003).
23. H. Liu et al., "Determination of optical properties and blood oxygenation in tissue using continuous NIR light," *Phys Med Biol* **40**(11), 1983-1993 (1995).
24. M. N. Kim et al., "Noninvasive measurement of cerebral blood flow and blood oxygenation using near-infrared and diffuse correlation spectroscopies in critically brain-injured adults," *Neurocrit Care* **12**(2), 173-180 (2010).
25. D. Irwin et al., "Influences of tissue absorption and scattering on diffuse correlation spectroscopy blood flow measurements," *Biomed Opt Express* **2**(7), 1969-1985 (2011).
26. K. Gurley, Y. Shang, and G. Yu, "Noninvasive optical quantification of absolute blood flow, blood oxygenation, and oxygen consumption rate in exercising skeletal muscle," *Journal of biomedical optics* **17**(7), 075010 (2012).
27. Y. Shang et al., "Noninvasive optical characterization of muscle blood flow, oxygenation, and metabolism in women with fibromyalgia," *Arthritis research & therapy* **14**(6), R236 (2012).
28. B. Henry et al., "Hybrid diffuse optical techniques for continuous hemodynamic measurement in gastrocnemius during plantar flexion exercise," *Journal of biomedical optics* **20**(12), 125006 (2015).
29. D. Boas, T. Gaudette, and S. Arridge, "Simultaneous imaging and optode calibration with diffuse optical tomography," *Opt Express* **8**(5), 263-270 (2001).
30. R. J. Cooper et al., "Transient haemodynamic events in neurologically compromised infants: a simultaneous EEG and diffuse optical imaging study," *Neuroimage* **55**(4), 1610-1616 (2011).
31. R. A. De Blasi et al., "Cerebral and muscle oxygen saturation measurement by frequency-domain near-infra-red spectrometer," *Med Biol Eng Comput* **33**(2), 228-230 (1995).

32. G. Yu et al., "Noninvasive monitoring of murine tumor blood flow during and after photodynamic therapy provides early assessment of therapeutic efficacy," *Clin Cancer Res* **11**(9), 3543-3552 (2005).
33. T. Durduran et al., "Diffuse optical measurement of blood flow, blood oxygenation, and metabolism in a human brain during sensorimotor cortex activation," *Opt Lett* **29**(15), 1766-1768 (2004).
34. G. Yu et al., "Validation of diffuse correlation spectroscopy for muscle blood flow with concurrent arterial spin labeled perfusion MRI," *Opt Express* **15**(3), 1064-1075 (2007).
35. C. Zhou et al., "Diffuse optical correlation tomography of cerebral blood flow during cortical spreading depression in rat brain," *Opt Express* **14**(3), 1125-1144 (2006).
36. D. A. Boas, and A. G. Yodh, "Spatially varying dynamical properties of turbid media probed with diffusing temporal light correlation," *JOSA A* **14**(1), 192-215 (1997).
37. Y. Shang et al., "Effects of muscle fiber motion on diffuse correlation spectroscopy blood flow measurements during exercise," *Biomed Opt Express* **1**(2), 500-511 (2010).
38. D. T. Thomas et al., "Local In Vivo Measures of Muscle Lipid and Oxygen Consumption Change in Response to Combined Vitamin D Repletion and Aerobic Training in Older Adults," *Nutrients* **11**(4), (2019).
39. Y. Lin et al., "Three-dimensional flow contrast imaging of deep tissue using noncontact diffuse correlation tomography," *Appl Phys Lett* **104**(12), 121103 (2014).
40. C. Huang et al., "Alignment of sources and detectors on breast surface for noncontact diffuse correlation tomography of breast tumors," *Appl Opt* **54**(29), 8808-8816 (2015).
41. L. He et al., "Noncontact diffuse correlation tomography of human breast tumor," *Journal of biomedical optics* **20**(8), 86003 (2015).
42. C. Huang et al., "Noncontact diffuse optical assessment of blood flow changes in head and neck free tissue transfer flaps," *Journal of biomedical optics* **20**(7), 075008 (2015).
43. N. B. Agochukwu et al., "A Novel Noncontact Diffuse Correlation Spectroscopy Device for Assessing Blood Flow in Mastectomy Skin Flaps: A Prospective Study in Patients Undergoing Prosthesis-Based Reconstruction," *Plast Reconstr Surg* **140**(1), 26-31 (2017).
44. C. Huang et al., "Speckle contrast diffuse correlation tomography of complex turbid medium flow," *Medical physics* **42**(7), 4000-4006 (2015).
45. C. Huang et al., "Noncontact 3-D Speckle Contrast Diffuse Correlation Tomography of Tissue Blood Flow Distribution," *IEEE Trans Med Imaging* **36**(10), 2068-2076 (2017).
46. S. Mazdeyasna et al., "Noncontact speckle contrast diffuse correlation tomography of blood flow distributions in tissues with arbitrary geometries," *Journal of biomedical optics* **23**(9), 1-9 (2018).
47. M. Zhao et al., "Noncontact Speckle Contrast Diffuse Correlation Tomography of Blood Flow Distributions in Burn Wounds," *2018 MHSRS Supplement to the Journal of Military Medicine (under revision)* (2019).

48. T. Hamaoka et al., "The use of muscle near-infrared spectroscopy in sport, health and medical sciences: recent developments," *Philos Trans A Math Phys Eng Sci* **369**(1955), 4591-4604 (2011).
49. J. L. Jasperse, D. R. Seals, and R. Callister, "Active forearm blood flow adjustments to handgrip exercise in young and older healthy men," *J Physiol* **474**(2), 353-360 (1994).
50. B. Chance et al., "Recovery from exercise-induced desaturation in the quadriceps muscles of elite competitive rowers," *Am J Physiol* **262**(3 Pt 1), C766-775 (1992).
51. V. Quaresima, R. Lepanto, and M. Ferrari, "The use of near infrared spectroscopy in sports medicine," *J Sports Med Phys Fitness* **43**(1), 1-13 (2003).
52. U. Wolf et al., "Localized irregularities in hemoglobin flow and oxygenation in calf muscle in patients with peripheral vascular disease detected with near-infrared spectrophotometry," *J Vasc Surg* **37**(5), 1017-1026 (2003).
53. A. Elvin et al., "Decreased muscle blood flow in fibromyalgia patients during standardised muscle exercise: a contrast media enhanced colour Doppler study," *Eur J Pain* **10**(2), 137-144 (2006).
54. R. Zelis et al., "A comparison of regional blood flow and oxygen utilization during dynamic forearm exercise in normal subjects and patients with congestive heart failure," *Circulation* **50**(1), 137-143 (1974).
55. K. K. McCully, C. Halber, and J. D. Posner, "Exercise-induced changes in oxygen saturation in the calf muscles of elderly subjects with peripheral vascular disease," *J Gerontol* **49**(3), B128-134 (1994).
56. G. Yu et al., "Time-dependent blood flow and oxygenation in human skeletal muscles measured with noninvasive near-infrared diffuse optical spectroscopies," *Journal of biomedical optics* **10**(2), 024027 (2005).
57. A. Sinha et al., "Improving the vitamin D status of vitamin D deficient adults is associated with improved mitochondrial oxidative function in skeletal muscle," *J Clin Endocrinol Metab* **98**(3), E509-513 (2013).
58. Z. C. Ryan et al., "1alpha,25-Dihydroxyvitamin D3 Regulates Mitochondrial Oxygen Consumption and Dynamics in Human Skeletal Muscle Cells," *J Biol Chem* **291**(3), 1514-1528 (2016).
59. S. McMahan, and H. A. Wenger, "The relationship between aerobic fitness and both power output and subsequent recovery during maximal intermittent exercise," *J Sci Med Sport* **1**(4), 219-227 (1998).
60. D. T. Ubbink et al., "Skin microcirculation in diabetic and non-diabetic patients at different stages of lower limb ischaemia," *Eur J Vasc Surg* **7**(6), 659-656 (1993).
61. E. Wahlberg et al., "Level of arterial obstruction in patients with peripheral arterial occlusive disease (PAOD) determined by laser Doppler fluxmetry," *Eur J Vasc Surg* **7**(6), 684-689 (1993).

62. Z. Chen et al., "Optical Doppler tomography: imaging in vivo blood flow dynamics following pharmacological intervention and photodynamic therapy," *Photochem Photobiol* **67**(1), 56-60 (1998).
63. J. C. Baron, "Mapping the ischaemic penumbra with PET: implications for acute stroke treatment," *Cerebrovasc Dis* **9**(4), 193-201 (1999).
64. P. Schmitt et al., "Quantitative tissue perfusion measurements in head and neck carcinoma patients before and during radiation therapy with a non-invasive MR imaging spin-labeling technique," *Radiother Oncol* **67**(1), 27-34 (2003).
65. R. F. Mottram, "The oxygen consumption of human skeletal muscle in vivo," *J Physiol* **128**(2), 268-276 (1955).
66. M. N. Smithies et al., "Comparison of oxygen consumption measurements: indirect calorimetry versus the reversed Fick method," *Crit Care Med* **19**(11), 1401-1406 (1991).
67. T. Sako et al., "Validity of NIR spectroscopy for quantitatively measuring muscle oxidative metabolic rate in exercise," *J Appl Physiol* (1985) **90**(1), 338-344 (2001).
68. Y. Shang et al., "Diffuse optical monitoring of repeated cerebral ischemia in mice," *Opt Express* **19**(21), 20301-20315 (2011).
69. Y. Shang et al., "Cerebral monitoring during carotid endarterectomy using near-infrared diffuse optical spectroscopies and electroencephalogram," *Phys Med Biol* **56**(10), 3015-3032 (2011).
70. G. Yu, "Near-infrared diffuse correlation spectroscopy in cancer diagnosis and therapy monitoring," *Journal of biomedical optics* **17**(1), 010901 (2012).
71. R. Cheng et al., "Near-infrared diffuse optical monitoring of cerebral blood flow and oxygenation for the prediction of vasovagal syncope," *Journal of biomedical optics* **19**(1), 17001 (2014).
72. Y. Shang et al., "Portable optical tissue flow oximeter based on diffuse correlation spectroscopy," *Opt Lett* **34**(22), 3556-3558 (2009).
73. H. M. Kooijman et al., "Near infrared spectroscopy for noninvasive assessment of claudication," *J Surg Res* **72**(1), 1-7 (1997).
74. E. Selvin, and T. P. Erlinger, "Prevalence of and risk factors for peripheral arterial disease in the United States: results from the National Health and Nutrition Examination Survey, 1999-2000," *Circulation* **110**(6), 738-743 (2004).
75. A. Yodh, and B. Chance, "Spectroscopy and imaging with diffusing light," *Physics Today* **48**(3), 34-41 (1995).
76. B. Chance, "Optical Tomography, photon migration, and spectroscopy of tissue and model media-theory, human studies and instrumentation," *Proc. SPIE* (1995).
77. R. M. Danen et al., "Regional imager for low-resolution functional imaging of the brain with diffusing near-infrared light," *Photochem Photobiol* **67**(1), 33-40 (1998).
78. D. A. Boas, "Diffuse photon probes of structural and dynamical properties of turbid media: theory and biomedical applications," Citeseer (1996).

79. C. Cheung et al., "In vivo cerebrovascular measurement combining diffuse near-infrared absorption and correlation spectroscopies," *Phys Med Biol* **46**(8), 2053-2065 (2001).
80. A. Kienle, and M. S. Patterson, "Improved solutions of the steady-state and the time-resolved diffusion equations for reflectance from a semi-infinite turbid medium," *J Opt Soc Am A Opt Image Sci Vis* **14**(1), 246-254 (1997).
81. M. S. Patterson et al., "Absorption spectroscopy in tissue-simulating materials: a theoretical and experimental study of photon paths," *Appl Opt* **34**(1), 22-30 (1995).
82. L. Dong et al., "Diffuse optical measurements of head and neck tumor hemodynamics for early prediction of chemoradiation therapy outcomes," *Journal of biomedical optics* **21**(8), 85004 (2016).
83. D. M. Hueber et al., "New optical probe designs for absolute (self-calibrating) NIR tissue hemoglobin measurements," *Optical tomography and spectroscopy of tissue III* 618-632 (1999).
84. S. Fantini, M. A. Franceschini, and E. Gratton, "Semi-infinite-geometry boundary problem for light migration in highly scattering media: a frequency-domain study in the diffusion approximation," *JOSA B* **11**(10), 2128-2138 (1994).
85. S. L. Jacques, "Optical properties of biological tissues: a review," *Phys Med Biol* **58**(11), R37-61 (2013).
86. D. T. Delpy et al., "Estimation of optical pathlength through tissue from direct time of flight measurement," *Phys Med Biol* **33**(12), 1433-1442 (1988).
87. D. R. White, H. Q. Woodard, and S. M. Hammond, "Average soft-tissue and bone models for use in radiation dosimetry," *Br J Radiol* **60**(717), 907-913 (1987).
88. D. R. White et al., "The composition of body tissues (II). Fetus to young adult," *Br J Radiol* **64**(758), 149-159 (1991).
89. D. A. Boas, L. Campbell, and A. G. Yodh, "Scattering and imaging with diffusing temporal field correlations," *Physical review letters* **75**(9), 1855 (1995).
90. S. O. Rice, "Mathematical analysis of random noise," *Bell System Technical Journal* **24**(1), 46-156 (1945).
91. A. Einstein, "On the motion of small particles suspended in liquids at rest required by the molecular-kinetic theory of heat," *Annalen der physik* **17**(549-560) (1905).
92. R. A. De Blasi et al., "Noninvasive measurement of human forearm oxygen consumption by near infrared spectroscopy," *Eur J Appl Physiol Occup Physiol* **67**(1), 20-25 (1993).
93. Y. Shang, K. Gurley, and G. Yu, "Diffuse Correlation Spectroscopy (DCS) for Assessment of Tissue Blood Flow in Skeletal Muscle: Recent Progress," *Anat Physiol* **3**(2), 128 (2013).
94. S. Zetterquist, "The effect of active training on the nutritive blood flow in exercising ischemic legs," *Scand J Clin Lab Invest* **25**(1), 101-111 (1970).
95. T. A. Mustoe, K. O'Shaughnessy, and O. Kloeters, "Chronic wound pathogenesis and current treatment strategies: a unifying hypothesis," *Plast Reconstr Surg* **117**(7 Suppl), 35S-41S (2006).

96. T. Mustoe, "Understanding chronic wounds: a unifying hypothesis on their pathogenesis and implications for therapy," *Am J Surg* **187**(5A), 65S-70S (2004).
97. H. Brem et al., "Evidence-based protocol for diabetic foot ulcers," *Plast Reconstr Surg* **117**(7 Suppl), 193S-209S; discussion 210S-211S (2006).
98. A. J. Boulton, "The diabetic foot: from art to science. The 18th Camillo Golgi lecture," *Diabetologia* **47**(8), 1343-1353 (2004).
99. G. C. Leng et al., "Incidence, natural history and cardiovascular events in symptomatic and asymptomatic peripheral arterial disease in the general population," *Int J Epidemiol* **25**(6), 1172-1181 (1996).
100. E. Tukiainen, F. Biancari, and M. Lepantalo, "Lower limb revascularization and free flap transfer for major ischemic tissue loss," *World J Surg* **24**(12), 1531-1536 (2000).
101. T. Li et al., "Simultaneous measurement of deep tissue blood flow and oxygenation using noncontact diffuse correlation spectroscopy flow-oximeter," *Sci Rep* **3**(1358) (2013).
102. H. Dehghani et al., "Near infrared optical tomography using NIRFAST: Algorithm for numerical model and image reconstruction," *Commun Numer Methods Eng* **25**(6), 711-732 (2008).
103. R. C. Allam, "Micronized, particulate dermal matrix to manage a non-healing pressure ulcer with undermined wound edges: a case report," *Ostomy Wound Manage* **53**(4), 78-82 (2007).
104. R. P. Boezeman et al., "Monitoring of Foot Oxygenation with Near-infrared Spectroscopy in Patients with Critical Limb Ischemia Undergoing Percutaneous Transluminal Angioplasty: A Pilot Study," *Eur J Vasc Endovasc Surg* **52**(5), 650-656 (2016).
105. A. M. Chiarelli et al., "Low-resolution mapping of the effective attenuation coefficient of the human head: a multidistance approach applied to high-density optical recordings," *Neurophotonics* **4**(2), 021103 (2017).
106. L. Dong et al., "Simultaneously extracting multiple parameters via fitting one single autocorrelation function curve in diffuse correlation spectroscopy," *IEEE Trans Biomed Eng* **60**(2), 361-368 (2013).
107. B. Chance et al., "Effects of solutes on optical properties of biological materials: models, cells, and tissues," *Anal Biochem* **227**(2), 351-362 (1995).
108. D. Tamborini et al., "Development and characterization of a multidistance and multiwavelength diffuse correlation spectroscopy system," *Neurophotonics* **5**(1), 011015 (2018).
109. J. Liu et al., "Simultaneously extracting multiple parameters via multi-distance and multi-exposure diffuse speckle contrast analysis," *Biomed Opt Express* **8**(10), 4537-4550 (2017).
110. C. P. Valdes et al., "Speckle contrast optical spectroscopy, a non-invasive, diffuse optical method for measuring microvascular blood flow in tissue," *Biomed Opt Express* **5**(8), 2769-2784 (2014).

- 111.P. Farzam, and T. Durduran, "Multidistance diffuse correlation spectroscopy for simultaneous estimation of blood flow index and optical properties," *Journal of biomedical optics* **20**(5), 55001 (2015).
- 112.C. Jiang et al., "Dedicated hardware processor and corresponding system-on-chip design for real-time laser speckle imaging," *Journal of biomedical optics* **16**(11), 116008 (2011).
- 113.A. K. Dunn, "Laser speckle contrast imaging of cerebral blood flow," *Ann Biomed Eng* **40**(2), 367-377 (2012).
- 114.A. Rajaram et al., "Simultaneous monitoring of cerebral perfusion and cytochrome c oxidase by combining broadband near-infrared spectroscopy and diffuse correlation spectroscopy," *Biomed Opt Express* **9**(6), 2588-2603 (2018).
- 115.D. A. Boas, and A. K. Dunn, "Laser speckle contrast imaging in biomedical optics," *Journal of biomedical optics* **15**(1), 011109 (2010).
- 116.X. Wu et al., "Fast and efficient image reconstruction for high density diffuse optical imaging of the human brain," *Biomed Opt Express* **6**(11), 4567-4584 (2015).

VITA

Mingjun Zhao, PhD candidate

EDUCATION

Biomedical Engineering, PhD program, University of Kentucky (UKY), US 2012/08 -- 2019/07
Date of qualifying exam: 12/16/2014; GPA: 3.69/4.0

Biomedical Engineering, B.E, Tianjin University (TJU), China 2008/09 -- /2012/07

PROFESSIONAL POSITIONS

Research Assistant, Department of Biomedical Engineering, UKY, Lexington, KY

AWARDS & HONORS

2017 fall Max Steckler Fellowship

2014/04 Conference Travel Support Awards, UKY

2011/10 1st Prize of 5th National Competition of MEMS Application, China

PROFESSIONAL MEMBERSHIP

2014, 2018 Optical Society of America (OSA)

2017, 2018 Biomedical Engineering Society (BMES)

PEER-REVIEWED JOURNAL PUBLICATIONS

1. **M. Zhao**, S. Mazdeyasna, C. Huang, N. B. Agochukwu, A. Bonaroti, L. Wong, G. Yu, "Noncontact Speckle Contrast Diffuse Correlation Tomography of Blood Flow Distributions in Burn Wounds", 2018 MHSRS Supplement to the Journal of Military Medicine (Under revision)
2. D. T. Thomas; D. Schnell; M. Redzic; **M. Zhao**; H. Abraha; D. Jones; H. Brim; G. Yu. "Local in vivo measures of muscle lipid and oxygen consumption change in response to combined vitamin D repletion and aerobic training in older adults", *Nutrients*, 11(4), 930 (2019)
3. S. Mazdeyasna, C. Huang, **M. Zhao**, N. B. Agochukwu, A. A. Bahrani, L. Wong, G. Yu, "Noncontact speckle contrast diffuse correlation tomography of blood flow distributions in tissues with arbitrary geometries", *Journal of Biomedical Optics*, 23(9), 096005 (2018)
4. C. Huang, D. Irwin, **M. Zhao**, Y. Shang, N. B. Agochukwu, L. Wong, G. Yu, "Noncontact 3-dimensional speckle contrast diffuse correlation tomography of tissue blood flow distribution", *IEEE Transactions on Medical Imaging*, 36(10), 2017

5. N. B. Agochukwu*, C. Huang*, **M. Zhao**, A. Bahrani, L. Wong, G. Yu, "A novel noncontact diffuse correlation spectroscopy for assessing blood flow in mastectomy skin flaps: a prospective study in patients undergoing prosthesis-based reconstruction", *Plastic and Reconstructive Surgery*, 140(1), 2017. *Contributed equally.
6. B. Henry*, **M. Zhao***, Y. Shang, T. Uhl, D. T. Thomas, E. S. Xenos, S. P. Saha, G. Yu, "Hybrid diffuse optical techniques for continuous hemodynamic measurement in gastrocnemius during plantar flexion exercise", *Journal of Biomedical Optics*, 20(12), 125006 (2015). *Contributed equally.

CONFERENCE PROCEEDINGS/ABSTRACTS

1. S. Mazdeyasna, A. Bonaroti, C. Huang, **M. Zhao**, M. Mohtasebi, X. Liu, L. Wong, G. Yu, "Noninvasive 3D Optical Imaging of Blood Flow Distributions in Mastectomy Skin Flaps", *BMES Annual Scientific Meeting, Philadelphia, PA* (Submitted, 2019)
2. S. Mazdeyasna, C. Huang, **M. Zhao**, A. Bonaroti, L. Wong, G. Yu, "Noninvasive 3D Optical Imaging of Blood Flow Distributions in Mastectomy Skin Flaps", *UK Markey Cancer Research Day, Lexington, KY, 2019*
3. M. Mohtasebi, A. Bahrani, **M. Zhao**, G. Yu, "Simultaneous Measurements of Cerebral Blood Oxygenation and Metabolism using Noninvasive Near-infrared Spectroscopy", *UK CCTS Spring Conference, Lexington, KY, 2019*
4. **M. Zhao**, C. Huang, G. Yu, "Extracting Multiple Tissue Optical Properties from Speckle Contrast Diffuse Correlation Tomography (scDCT) Measurements", *UK CCTS Spring Conference, Lexington, KY, 2019*
5. S. Mazdeyasna, C. Huang, **M. Zhao**, M. Mohtasebi, A. Bonaroti, L. Wong, G. Yu, "Noncontact 2D and 3D diffuse optical imaging of tissue blood flow distributions", *UK CCTS Spring Conference, Lexington, KY, 2019*
6. **M. Zhao**, D. Jones, D. T. Thomas, G. Yu, "Monitoring of Muscle Hemodynamics during Exercise Using Hybrid Near-infrared Spectroscopy and Diffuse Correlation Spectroscopy in Older Adults", *BMES Annual Scientific Meeting, Atlanta, GA, 2018*
7. S. Mazdeyasna, C. Huang, **M. Zhao**, N. Agochukwu, A. Bahrani, L. Wong, G. Yu, "Intraoperative 3D imaging of blood flow distributions in mastectomy skin flaps using noncontact speckle contrast diffuse correlation tomography", *BMES Annual Scientific Meeting, Atlanta, GA, 2018*
8. L. Wong, **M. Zhao**, C. Huang, N. Agochukwu, S. Mazdeyasna, A. Bahrani, L. Chen, J. Radabaugh, R. Aouad, G. Yu, "Perioperative Optical Assessment of Blood Flow Variations in Soft Tissues: Implications for Assessment & Management of Battlefield Injuries", *Military Health System Research Symposium, Kissimee, FL, (2018)*
9. **M. Zhao**, C. Huang, N. Agochukwu, L. Wong, J. P. Radabaugh, R. K. Aouad, G. Yu, "Intraoperative Monitoring of Tissue Blood Flow Alterations for Predicting Flap Necrosis", *UK Markey Cancer Research Day, Lexington, KY, 2018*
10. **M. Zhao**, C. Huang, S. Mazdeyasna, N. Agochukwu, L. Wong, G. Yu, "Noncontact Speckle Contrast Diffuse Correlation Tomography for 3-D Blood Flow Imaging of Burn Wounds", *UK CCTS Spring Conference, Lexington, KY, 2018*
11. D. Jones, **M. Zhao**, G. Yu, D. T. Thomas, "Vitamin D Repletion Coupled with Aerobic Training Improves Skeletal Muscle Oxygen Extraction During Fatiguing Exercise in Healthy Older Adults", *UK CCTS Spring Conference, Lexington, KY, 2018*

12. S. Mazdeyasna, C. Huang, **M. Zhao**, A. Bahrani, N. Agochukwu, L. Wong, G. Yu, “Intraoperative imaging of blood flow distributions in mastectomy skin flaps using speckle contrast diffuse correlation tomography”, UK CCTS Spring Conference, Lexington, KY, 2018
13. D. Irwin, C. Huang, **M. Zhao**, S. Mazdeyasna, A. Bahrani, G. Yu, “Noncontact Imaging of Flow and Fluorescence Contrasts”, UK CCTS Spring Conference, Lexington, KY, 2018
14. **M. Zhao**, C. Huang, D. Irwin, S. Mazdeyasna, A. Bahrani, N. Agochukwu, L. Wong, G. Yu, “EMCCD-based Speckle Contrast Diffuse Correlation Tomography of Tissue Blood Flow Distribution”. Biophotonics Congress: Biomedical Optics, Hollywood, FL, 2018. Oral Presentation
15. **M. Zhao**, C. Huang, L. Chen, J. Radabaugh, R. Aouad, N. Agochukwu, L. Wong, G. Yu, “Intraoperative Assessment of Blood Flow Variations in Tissue Flaps Using Noncontact Diffuse Correlation Spectroscopy”. Biophotonics Congress: Biomedical Optics, Hollywood, FL, 2018. Oral Presentation
16. **M. Zhao**, C. Huang, S. Mazdeyasna, E. A. Jawdeh, H. Bada, G. Yu, “A Novel Fiberless Diffuse Speckle Contrast Flowmeter for Tissue Blood Flow Measurement”. Biophotonics Congress: Biomedical Optics, Hollywood, FL, 2018. Oral Presentation
17. N. Agochukwu, C. Huang, S. Mazdeyasna, **M. Zhao**, G. Yu, L. Wong. “3D Imaging of Tissue Blood Flow in Mastectomy Skin Flaps”. American Society of Plastic Surgeons 2017 Annual Meeting. Oral Presentation.
18. S. Mazdeyasna, C. Huang, N. McGregor, **M. Zhao**, A. Bahrani, G. Yu, “A photometric stereo technique to acquire tissue surface geometry for 3D imaging of blood flow distributions in mastectomy skin flaps”, BMES Annual Scientific Meeting, Phoenix, AZ, 2017
19. S. Mazdeyasna, C. Huang, M. Seong, J. Morgan, **M. Zhao**, A. Bahrani, J. Kim, J. Hastings, G. Yu, “A novel low-cost compact diffuse speckle contrast flowmeter for contact blood flow measurement”, BMES Annual Scientific Meeting, Phoenix, AZ, 2017 (oral presentation).
20. **M. Zhao**, C. Huang, D. Irwin, S. Mazdeyasna, N. Agochukwu, L. Wong, G. Yu, “Noncontact 3-dimensional speckle contrast diffuse correlation tomography of tissue blood flow distribution”, BMES Annual Scientific Meeting, Phoenix, AZ, 2017 (oral presentation)
21. **M. Zhao**, C. Huang, N. Agochukwu, A. Bahrani, S. Mazdeyasna, L. Wong, G. Yu, Noncontact diffuse correlation spectroscopy assessment of tissue blood flow for the prediction of mastectomy skin flap necrosis”, BMES Annual Scientific Meeting, Phoenix, AZ, 2017
22. **M. Zhao**, C. Huang, N. Agochukwu, L. Wong, G. Yu, “Noncontact diffuse optical assessment of blood flow imaging in mastectomy skin flaps”, UK CCTS Spring Conference, Lexington, KY, 2017
23. **M. Zhao**, C. Huang, N. Agochukwu, L. Wong, G. Yu, “Noncontact Diffuse Optical Imaging of Blood Flow Distribution and Necrosis Prediction in Mastectomy Skin Flaps”, Markey Cancer Center Breast Cancer Symposium, Lexington, KY, 2017
24. C. Huang, **M. Zhao**, D. Irwin, N. Agochukwu, L. Wong, G. Yu, “Noncontact 3-dimensional speckle contrast diffuse correlation tomography of tissue blood flow distribution”, UK CCTS Spring Conference, Lexington, KY, 2017 (Oral)
25. C. Huang, **M. Zhao**, D. Irwin, N. Agochukwu, L. Wong, G. Yu, “Noncontact 3-dimensional speckle contrast diffuse correlation tomography of tissue blood flow distribution”, Markey Cancer Center Breast Cancer Symposium, Lexington, KY, 2017
26. N. B. Agochukwu, C. Huang, **M. Zhao**, G. Yu, L. Wong, “A novel noncontact optical

method for assessing blood flow in mastectomy skin flaps: A prospective study in patients undergoing prosthetic based reconstruction”. Annual Meeting of the Southeastern Society of Plastic Surgeons, Orlando FL, (2016) (oral presentation)

27. G. Yu, C. Huang, N. B. Agochukwu, **M. Zhao**, L. Wong, “Intraoperative optical assessment of blood flow changes in mastectomy skin flaps in patients with breast cancer”, Markey Cancer Center Breast Cancer Symposium, Lexington, KY, 2016 (Oral)
28. C. Huang, N. B. Agochukwu, **M. Zhao**, “L. Wong, G. Yu, Intraoperative optical assessment of blood flow changes in mastectomy skin flaps”, UK CCTS Spring Conference, Lexington, KY, 2016
29. **M. Zhao**, C. Huang, E. Xenos, G. Yu, “Diffuse Optical Assessment of Blood Flow Distribution in Wounded Tissue: A Case Study”, UK CCTS Spring Conference, Lexington, KY, 2015
30. **M. Zhao**, Y. Shang, B. Henry, T. L. Uhl, G. Yu, “Tissue metabolic rate of oxygen consumption in calf muscle measured by arterial and venous occlusion protocols”, OSA Biomedical Optics (BIOMED), Miami, FL, 2014
31. **M. Zhao**, Y. Shang, B. A. Henry, G. Yu, “Measurements of tissue metabolic rate of oxygen consumption in skeletal muscle using arterial and venous occlusion protocols”, University of Kentucky Muscle Biology Fall Retreat, Lexington, KY, 2013
32. B. A. Henry, Y. Shang, **M. Zhao**, T. Uhl, and G. Yu, “Diffuse optical spectroscopies for continuous monitoring of absolute tissue hemodynamics in calf muscle during plantar flexion exercise”, University of Kentucky Muscle Biology Fall Retreat, Lexington, KY, 2013
33. **M. Zhao**, Y. Shang, B. A. Henry, G. Yu, “Measurements of tissue metabolic rate of oxygen consumption in skeletal muscle using arterial and venous occlusion protocols”, University of Kentucky Muscle Biology Fall Retreat, Lexington, KY, 2013
34. D. Irwin, Y. Lin, L. He, C. Huang, Y. Shang, **M. Zhao**, G. Yu, “Noncontact 3-D imaging of small animal tumors with combined diffuse optical, correlation, and fluorescence tomography: preliminary results in phantoms”, UK CCTS Spring Conference, Lexington, KY, 2013
35. **M. Zhao**, Y. Shang, B. A. Henry, G. Yu, “Comparison of ultrasound imaging and skinfold caliper measurements of subcutaneous adipose tissue thickness”, UK CCTS Spring Conference, Lexington, KY, 2013
36. D. Irwin, Y. Lin, L. He, C. Huang, Y. Shang, **M. Zhao**, G. Yu, “Noncontact 3-D imaging of small animal tumors with combined diffuse optical, correlation, and fluorescence tomography: preliminary results in phantoms”, UK Markey Cancer Research Day, Lexington, KY, 2013